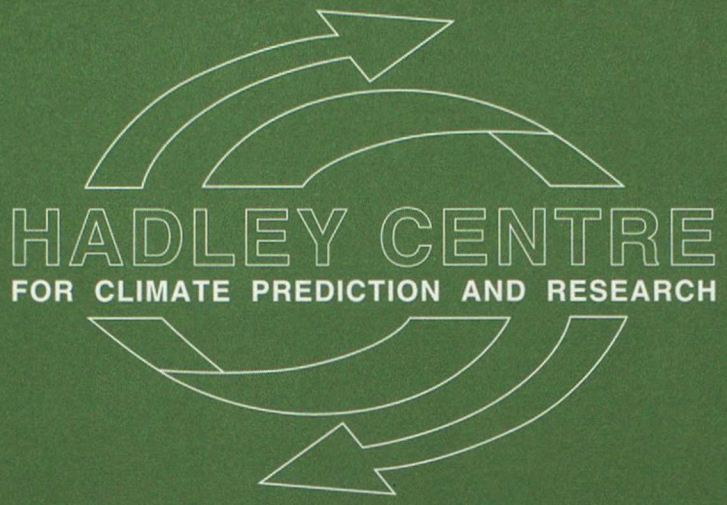

The second Hadley Centre coupled ocean-atmosphere GCM: Model description, spinup and validation

by

TC Johns, RE Carnell, JF Crossley, JM Gregory, JFB Mitchell, CA Senior, SFB Tett and RA Wood

CRTN 67 **January 1996**

CLIMATE
RESEARCH
TECHNICAL
NOTE

Hadley Centre
Meteorological Office
London Road
Bracknell
Berkshire RG12 2SY

CLIMATE RESEARCH TECHNICAL NOTE NO. 67

THE SECOND HADLEY CENTRE COUPLED OCEAN-ATMOSPHERE GCM: MODEL DESCRIPTION, SPINUP AND VALIDATION

by

T C Johns, R E Carnell, J F Crossley, J M Gregory,
J F B Mitchell, C A Senior, S F B Tett and R A Wood

Submitted to Climate Dynamics

Hadley Centre for Climate Prediction and Research
Meteorological Office
London Road
Bracknell
Berkshire RG12 2SY

NOTE: This paper has not been published. Permission to quote from it should be obtained from the Director of the Hadley Centre.

The Second Hadley Centre Coupled Ocean-Atmosphere GCM: Model Description, Spinup and Validation.

Tim C. Johns, Ruth E. Carnell, Jenny F. Crossley, Jonathan M. Gregory, John F.B. Mitchell, Catherine A. Senior, Simon F.B. Tett, and Richard A. Wood

Hadley Centre for Climate Prediction and Research, Meteorological Office, London Road, Bracknell, RG12 2SY, UK

Submitted to *Climate Dynamics*

25 January 1996

Corresponding author's address:

Dr. Tim Johns,
Hadley Centre for Climate Prediction and Research,
Meteorological Office,
London Road,
Bracknell,
RG12 2SY,
UK
tel: +[44]-1344-856901
fax: +[44]-1344-854898
email: tcjohns@meto.govt.uk

Abstract

This paper describes a new coupled ocean-atmosphere general circulation model (OAGCM) developed for studies of climate change and results from a hindcast experiment. The model includes various physical and technical improvements relative to an earlier version of the Hadley Centre OAGCM. A coupled spinup process is used to bring the model to equilibrium. Compared to uncoupled spinup methods this is computationally more expensive, but helps to counter climate drift arising from inadequate sampling of short timescale coupled variability when the components are equilibrated separately. Including sea ice advection and enhancing reference surface salinities in high southern latitudes in austral winter to promote bottom water formation during spinup appears to have stabilised the high latitude drift exhibited in the earlier model's control run. In the present study, the atmospheric control climate is stable on multi-century timescales with a drift in global average surface air temperature of only +0.016 K/century, despite a small residual drift in the deep ocean. The control climate is an improvement over the earlier model in several respects, notably in its variability on short timescales. Two anomaly runs are presented incorporating estimated forcing changes over the period 1860 to 1990 arising from greenhouse gases alone and from greenhouse gases plus the radiative scattering effect of sulphate aerosols. These allow validation of the model against the instrumental climate record. Inclusion of aerosol forcing gives a significantly better simulation of historical temperature patterns, although comparisons against recent sea ice trends are equivocal. These studies emphasize the potential importance of including additional forcing terms apart from greenhouse gases in climate simulations, and refining estimates of their spatial distribution and magnitude.

1 INTRODUCTION

The need for improved understanding of basic climate processes, sensitivity and feedback mechanisms in the context of anthropogenic emissions of pollutants and their radiative forcing effect has recently received much attention in the scientific community. Recent reports by the Intergovernmental Panel on Climate Change (IPCC) summarise the scientific concensus on current understanding and key issues (Houghton et al. 1990; Houghton et al. 1992; Houghton et al. 1994). One of the main goals of new research is to produce improved physically based predictions of the effects of natural and anthropogenic perturbations on global and regional climate, taking account of the time dependent nature of the perturbations. Probably the most important tools available to assist in this endeavour are coupled ocean-atmosphere general circulation models (OAGCMs), which presently include comprehensive representations of the world's atmosphere, land surface, ocean and sea ice components. Only such models, carefully validated against observed climate, offer the possibility of exploring the complex feedbacks in the climate system and the interplay between regional and global climate forcing and responses. In future, interactively coupled biosphere, land ice and chemistry components are also likely to be added, to permit modelling of a wider range of feedbacks.

Many groups worldwide are now involved in developing OAGCMs to improve understanding of climate processes, and to perform more realistic time dependent simulations of climate change (for a recent summary see Meehl 1995 and WCRP 1995). In this paper, we describe and document a new OAGCM developed at the Hadley Centre, and present some results from initial experiments. The new model includes enhancements to its formulation and resolution compared with the original coupled model described by Murphy (1995).

Due to the computational cost of running such models, only a limited number of century timescale simulations have been published to date (Washington and Meehl 1989; Manabe et al. 1991; Manabe et al. 1992; Cubasch et al. 1992; Meehl et al. 1993; Cubasch et al. 1994; Cubasch et al. 1995; Murphy 1995; Murphy and Mitchell 1995; Power et al. 1993; Russell et al. 1995; Tokioka et al. 1995). Most have used idealised experimental designs which make the results difficult to relate directly to evolving climate change in the real world. The realism of experiments is improved by starting the perturbed forcing from an early historical era, when forcing was relatively weak compared to present and projected future levels. Cubasch et al. (1995) started an experiment in 1935 with observed forcing changes, but to reduce the significance of neglecting past forcing to acceptable levels it is desirable to start at least 100 years before present. This

requires a large computational investment but is feasible on modern computers and has been done in the present study.

Another large computational overhead is the time taken to bring the intermediate and deep ocean into equilibrium with the rest of the coupled system, in order to minimise climate drift in the simulations. There are techniques for speeding up the approach of the ocean to equilibrium (Bryan 1984), but these are not necessarily applicable when the seasonal cycle of forcing is included. Some groups have nevertheless apparently used accelerated ocean spinup techniques successfully to initialise the ocean state for long climate studies (eg. Manabe et al. 1991; Manabe et al. 1992; Stouffer et al. 1994). However, for acceleration techniques to be applied, an uncoupled ocean spinup must be used. But there are suggestions that uncoupled spinup may leave a residual drift in models with strong coupled variability, even if the component models are 'perfect' (Power 1995); coupled spinup may therefore be a better strategy in such models. Our experience with the new model supports this notion.

In the next section, the new OAGCM is described, identifying the main changes and improvements in formulation. The model spinup is described in section 3, together with some remarks on the influence of the methodology in minimising subsequent climate drift. In section 4, the experimental design is outlined. An assessment of a multi-century control run is given in section 5. In section 6 we validate the time dependent response of the model forced with greenhouse gas changes alone and greenhouse gas changes plus sulphate aerosol effects against the instrumental temperature record and recent sea ice changes. Conclusions are given in section 7.

2 MODEL DESCRIPTION

The coupled model used in this study derives from that used in an earlier climate change study conducted at the Hadley Centre (Murphy 1995; Murphy and Mitchell 1995; hereafter 'UKTR'). Considerable changes have been made to the component models, which now run under the Unified Model system ('UM' - Cullen 1993). As in UKTR the oceanic component of the model is based on the Bryan-Cox primitive equation code, but recoded to interface to the UM system. The present model's atmospheric component has been completely rewritten. In particular, the atmospheric dynamics scheme is completely different, based on a new grid type, requiring changes in some of the physical parameterizations. The ocean and sea ice components are also modified in significant ways from UKTR. The new OAGCM version (designated 'HADCM2' - **Had**ley Centre **C**oupled **M**odel - version **2**) is described below, highlighting key differences relative to UKTR. For a more detailed technical description see Johns (1996).

Model resolution and grid layout

The horizontal resolution of the model is 2.5 degrees in latitude by 3.75 degrees in longitude, as in UKTR. This gives a grid spacing of 278 km in the North-South direction and 417 km East-West at the equator reducing to 295 km at 45 degrees North and South - comparable to a T42 spectral model resolution). To simplify coupling between atmosphere and ocean the layout of the horizontal grid and coastline in the ocean model have been chosen exactly congruent to the atmosphere, with the exception that the northern row is considered to be land (a polar island) in the ocean model but sea in the atmospheric model. This is an expedient measure to avoid difficulties in specifying boundary conditions at the coordinate singularity. Conservation of atmospheric fluxes into the ocean is therefore achieved without the need for horizontal interpolation or redistribution. An island representing Iceland, absent in UKTR, is included in the new model. Vertical resolution is enhanced in both components relative to UKTR, from 11 to 19 levels in the atmosphere, and 17 to 20 levels in the ocean. The sea ice component remains a 'zero-layer' model sharing the ocean model horizontal grid, but with the addition of simple ice and snow advection (Bryan 1969b).

Atmosphere Model

The atmospheric model equations are a quasi-hydrostatic version of the full primitive equations in spherical polar coordinates with a complete representation of the Coriolis force in which the usual shallow atmosphere approximation is relaxed (White and Bromley 1995). Physical parameterizations and numerical diffusion are represented by 3-dimensional source and sink vector functions of the main state variables. The predicted state variables are surface pressure, horizontal wind components, and two conserved thermodynamic variables "liquid water potential temperature" and "total water mixing ratio" related to potential temperature and specific humidity via the cloud water content (Smith 1990). Dynamical boundary conditions are the orographic height at the lower boundary and the implied mass continuity condition that vertical velocities through the upper and lower coordinate boundary vanish. Various other boundary conditions related to the physical parameterizations (particularly the land surface and hydrology schemes) are imposed via climatological fixed or seasonally-varying datasets. A 30 minute timestep is used to compute increments from both dynamical and physical parameterisations, although full radiation calculations are performed only every 3 hours for economy. In UKTR, a 10 minute timestep was used, except for radiation.

An Arakawa 'B'-grid (Arakawa and Lamb 1977) layout is used for horizontal discretization in the atmospheric model, in place of the Arakawa 'A'-grid used in UKTR, as the revised dynamics scheme achieves better accuracy on this staggered grid. The layout places surface pressure and the thermodynamic variables at the centre of the gridcell with wind components at the corners. A hybrid coordinate (Simmons and Burridge 1981) is used for the vertical discretization rather than the sigma coordinate used in UKTR. The bottom 4 of the 19 layers (Table 1) are terrain-following sigma layers and the top 3 layers pure pressure layers, with a smooth transition in between.

A split-explicit scheme (Cullen and Davies 1991) integrates the equations in time, the geostrophic adjustment process being separated from the advection part. A 10 minute timestep is used for adjustment, iterated three times per 30 minute advection timestep. Averaged velocities over the three adjustment timesteps are used for advection, which is integrated in time using the Heun scheme (Mesinger 1981). The finite difference scheme is 4th-order accurate in space. Geostrophic adjustment is resolved more accurately than in UKTR as a result of the staggered grid layout, and a longer advection (and hence physics) timestep is made possible by the split adjustment and advection parts.

The dynamical equations in their numerical form formally conserve mass, energy, momentum, angular momentum and total water in the absence of source and sink terms. Fourier damping of unstable zonal wavenumbers is necessary at high latitudes, damping weights being recomputed every 6 hours according to local wind strength. The variables filtered are mass-weighted winds during adjustment and after diffusion, and mass-weighted increments to thermodynamic variables from advection. In addition, an iterated del-squared diffusion process is applied globally to mass-weighted liquid water potential temperature and winds (3 iterations except in the top layer which has only one iteration), and mass-weighted total water (2 iterations). The e-folding times for 2 and 4 gridlength waves associated with diffusion are 6.9 and 29 hours respectively for total water, and 3.7 and 31 hours respectively for other variables. Both filtering and diffusion introduce an energy loss into the model, which is numerically corrected with a 1-day lag by adding a globally constant temperature increment computed daily as a global heat budget residual taking account of all fluxes into the system. Small losses of mass resulting from numerical rounding are also corrected with a 1-day lag.

In regions of strong local gradient the advection scheme can produce negative humidity. To correct this, negative values are set to zero and remaining points in the same layer rescaled to preserve the layer total. If there is insufficient positive moisture to allow a redistribution, negative values are reset to zero without rescaling positive values, resulting in a net source of atmospheric moisture. Even in layers which conserve moisture, systematic local sources and sinks will generally be created, but on a large scale this effect is relatively minor, the zonal

average absolute flux due to vertically-integrated sources/sinks in the column being below 0.5% of the zonal average absolute net precipitation minus evaporation flux in an annual mean sense at all latitudes apart from the South Pole. This correction scheme is expected to be improved in future to prevent non-conservation.

Gravity wave drag is applied to momentum components in the free atmosphere using a parameterization based on a prescribed sub-grid scale orographic variance field and the vertical stability profile as a function of height through the atmospheric column (Palmer et al. 1986). Anisotropies in the orographic variance are neglected in computing the drag in this scheme.

The radiation scheme consists of two parts; solar calculations, which use four spectral bands as defined in Slingo (1989), and longwave calculations, which use six spectral bands as defined in Slingo and Wilderspin (1986). Both the diurnal cycle and annual cycle of insolation are represented, with the incoming solar part of the radiation rescaled on each physics timestep to give more smoothly varying radiative forcing during daylight hours. Interactive cloud optical properties are computed from the derived cloud water and ice contents (Slingo 1989) assuming an effective droplet radius of 7 μm for water cloud and 30 μm for ice cloud. Radiative transfer calculations take account of the effects of water vapour, carbon dioxide, and ozone (specified from zonal average monthly climatological data) in addition to clouds. Maximum/random overlap of all cloudy layers is assumed in the longwave, but randomly overlapped low, medium and high cloud is assumed in the solar. Low, medium and high cloud groups are defined as layers 1-5, 6-9 and 10-18 respectively. Within each cloud group, the layer with the greatest fractional cover defines the cloud cover and cloud level for the whole group (taking the lowest level if more than one layer is equal), the cloud water from all layers in the group being assumed to be uniformly distributed over that cloud fraction. Surface albedo at ice-free sea points and for leads is calculated as a specified function of solar zenith angle for the direct beam, ranging from 0.05 at the zenith to 0.06 at 45 degrees and 0.17 at 75 degrees, and 0.06 for the diffuse beam. Over sea ice, albedo varies linearly from 0.80 for surface temperature at and below 263.15 K to 0.5 at 273.15 K. Bare ice and snow-covered ice are not differentiated. Over land, albedo is computed from snow-free and deep snow albedos specified according to vegetation type, based on predicted snow depth and surface temperature. In UKTR, solar radiation was not resolved into separate spectral bands as in the present model, so a fixed fractional split of net solar into penetrating and non-penetrating flux into the ocean was assumed. Now, the ocean penetrating component of radiation is computed as a separate band (250 to 690 nm) in the radiation scheme.

Large-scale cloud water and total cloudiness are computed at each point from the total water variable, according to the local temperature and a reference relative humidity, using a simple functional relation to determine the fraction of total water in cloud form. For the purposes of radiation and precipitation, cloud water is split into liquid and ice fractions. The cloud ice fraction increases as a smoothly varying function of temperature from zero to the total amount over the temperature range 0 to -15 degrees C (Smith 1990).

The boundary layer can occupy up to the bottom 5 atmosphere model layers. A first-order turbulent mixing scheme is used to mix the conserved thermodynamic variables and momentum in the vertical (Smith 1990). Over land, surface roughness characteristics are prescribed according to climatological surface type, but at sea points the roughness length over open water is computed from local windspeeds using the Charnock formula (Charnock 1955) with a lower limit of 10^{-4} m in calm conditions. Partial sea ice cover is allowed in surface calculations at ocean points, with separate fluxes computed for sea ice and leads within an icy gridbox. In order to resolve the diurnal cycle of surface temperature over sea ice, a small surface areal heat capacity equivalent to about 5 cm of water is assumed, while the surface ocean temperature within the leads portion of an icy gridbox is fixed at -1.8 degrees C. A 4-layer soil temperature model (Warrilow et al. 1986) is embedded in the land surface part of the scheme. The choice of soil layer thicknesses is designed to resolve both the diurnal and seasonal cycles with minimal distortion. A zero heat flux condition is imposed at the base of the soil model to conserve heat within the system. Fluxes from the boundary layer are computed for coupling with the sea ice and ocean model, the new model taking account of ocean surface currents (neglected

in UKTR) as well as lowest level winds in computing exchange coefficients for heat, moisture and momentum fluxes. Accounting for ocean currents is potentially important in determining surface stress in equatorial regions, where surface currents are significant compared with surface winds (Pacanowski 1987).

Surface hydrology calculations take account of storage of water in a vegetative canopy in addition to ground storage. Canopy evaporation and transpiration, throughfall of moisture from the canopy to the ground, and surface and sub-surface runoff are modelled according to local moisture availability, canopy and ground water content and prescribed parameters (fixed throughout the year) for vegetative fraction, canopy capacity, hydraulic conductivity, infiltration rate, wilting point, root depth, stomatal resistance, critical soil moisture limit for evaporation, and Eagleson's exponent (Warrilow et al. 1986). The scheme is similar to that in UKTR except that in calculating canopy throughfall and surface runoff, a distribution of rainfall rate within each gridbox rather than a uniform value is assumed (Dolman and Gregory 1992). The model also differs from UKTR in that river outflow is now included, giving the possibility of ocean salinity feedbacks via land changes. Surface and sub-surface runoff are converted into river outflow using predefined river catchments over land and associated coastal outflow points defined relative to the model grid, taking account of actual geographical catchments rather than basing them on the slope of the model orography. River transport is not modelled explicitly, so runoff is transported instantaneously to the coast.

Large-scale (dynamic) rainfall and snowfall calculations are based on cloud water and ice contents and are generally similar to those in UKTR (Smith 1990). Evaporation of falling precipitation, enhanced precipitation rates via seeding from layers above, and phase changes between cloud water and ice are represented. The ice fallout scheme has been modified to allow cloud ice to contribute to the water and ice budget of lower levels as it falls, rather than falling instantaneously through to the ground.

Convective rainfall and snowfall are calculated using a mass flux penetrative convection scheme (Gregory and Rowntree 1990), similar to UKTR but with the addition of an explicit downdraught representation (Gregory and Allen 1991). Mixing of convective parcels with environmental air, forced entrainment and detrainment, and evaporation of falling precipitation are all modelled. Convective cloud amounts are computed from the column condensed water path via a simple functional relation (Slingo et al. 1988).

Ocean Model

The ocean component of the model is based on the Bryan-Cox primitive equation model (Bryan 1969a, Cox 1984). The 20 depth levels in the vertical are listed in Table 2. Level spacing is small near the surface in order to resolve the mixed layer, the top layer being 10m thick. Bottom topography is derived from the Scripps 1 degree resolution orography dataset (Gates and Nelson 1973), with single gridpoint inlets and basins removed. A 1 hour timestep is used to integrate the model (ie. 2 hour leapfrog timestep), with a Robert time filter applied to suppress the grid-splitting mode and a forward timestep once a day to allow storage of just one time level at model checkpoints. In UKTR, a 20 minute timestep was used.

An energy balance mixed layer model based on Kraus and Turner (1967) is embedded in the model, like that used in UKTR. Any negative surface buoyancy flux into the ocean surface is convectively mixed down to a neutrally buoyant level (in terms of potential density relative to the surface). 15% of the gravitational potential energy released by this convection, and 70% of the work done by the wind on the ocean surface, are assumed to be available for turbulent kinetic energy (TKE). The amount of available TKE is assumed to decay exponentially with depth, with an e-folding scale of 100m. Mixing continues down to a level at which the density profile is statically stable and the TKE is depleted. Any subsurface static instability (for example, caused by horizontal advection of light water masses) is effectively removed at the end of the timestep using 5 iterations of the convective mixing algorithm described by Cox (1984). Only potential temperature and salinity are mixed by these schemes.

Further vertical mixing is provided at all depths through vertical diffusion both of tracers (potential temperature and salinity) and momentum. The vertical diffusivity is the sum of a depth-dependent constant background term and a term dependent on Richardson number (Pacanowski and Philander 1981). In practice it is found that the latter term is small everywhere except in the mixed layer. For momentum, a background value of 1.0×10^{-5} m^2/s is used at all levels. The background profile for tracers (Table 2) is a close fit to the theoretical/observational estimate of Kraus (1990), and the near-surface values are in good agreement with recent direct measurements in the upper 1000m of the ocean (Ledwell et al. 1993). UKTR used 1.0×10^{-5} m^2/s at all levels (the surface value in the present model), and so had lower tracer diffusivities at all depths.

A horizontal momentum diffusivity (eddy viscosity) of 1.5×10^5 (1+cos(latitude)) m^2/s is applied. This latitudinal profile spreads the subtropical western boundary currents in the model sufficiently to allow them to be resolved at the model resolution, while avoiding a restriction on the timestep due to numerical instability in the diffusion equation at high latitudes. The cosine dependence of diffusivity was omitted in UKTR. Tracers are diffused along isopycnal surfaces (Redi 1982), with a depth-dependent diffusivity of $(400 + 1600\exp(-z/500))$ m^2/s, where z is the depth in metres. A background horizontal diffusivity of 40 m^2/s is also applied to tracers to control gridscale noise.

There is no direct connection between the Mediterranean Sea and Atlantic Ocean with the modelled coastline and bathymetry, but mixing of temperature and salinity across the Straits of Gibraltar is parameterized by completely mixing the easternmost point of the Atlantic with the westernmost point of the Mediterranean having the same depth of water, in the manner of Manabe and Stouffer (1988). Mixing occurs over the top 13 layers, to a depth of 1200m, on the assumption that Mediterranean water will sink to at least this depth after flowing over the sill. Mixing between the Atlantic and Mediterranean was not represented in UKTR.

Sea Ice Model

The thermodynamics of the model is based on the zero-layer model of Semtner (1976). A parameterisation of ice concentration, A, based on that of Hibler (1979), is included. A is not allowed to exceed 0.995 in the Arctic and 0.980 in the Antarctic since completely unbroken ice cover is rarely observed in reality even in pack ice. Ice depth can be increased by the formation of "white ice" (Ledley 1985) where the weight of snow forces the ice-snow interface below the water line.

The effect of sea ice formation and melt on ocean salinity is accounted for within the model, assuming a constant salinity of 0.6% for sea ice. Sublimation increases ocean salinity, as the salt is assumed to blow into leads, and white ice formation reduces it to account for the salt added in converting snow to ice. Snowfall reduces ocean salinity in leads, and accumulates onto ice, and all rainfall is assumed to reach the ocean through leads.

Surface fluxes over the ice and leads fractions of each grid box, and surface temperatures, are calculated separately within the atmosphere component of the model, assuming a linear temperature profile in the ice. In UKTR wind mixing (mechanical) energy was not applied under ice, leading to rather shallow mixed layers, so in the present model a windmixing energy, calculated using the drag coefficient appropriate for leads and weighted by the leads fraction of the grid square, is applied to the ocean. Oceanic heat flux into the base of the ice is related to the temperature difference between the ocean top level and the base of the ice (assumed to be at a freezing point of -1.8 degrees C), as in the previous model, with a coupling coefficient of 20 $W/m^2/K$.

A simple parameterization of sea ice dynamics, omitted in UKTR, is now included, based on Bryan (1969b). Ice thickness, concentration and snow depth are advected using the top layer ocean current, and an upstream advection scheme. Ice rheology is crudely represented by preventing convergence of ice once the ice depth reaches 4m. Del-squared horizontal diffusion of ice depth is also applied, with a coefficient 2000 m^2/s.

In UKTR, net heat fluxes from the leads fraction of a grid square with ice were used within the ice model to melt or form ice via Hibler's (1979) leads formulation, rather than to cool or warm the ocean. This gives unrealistic behaviour with dynamics added to the model; as soon as a small amount of ice advected over a warm but cooling ocean, the net heat flux from ocean to atmosphere tending to cool the ocean was entirely diverted into forming ice instead. Unlike in UKTR, the penetrative part of shortwave radiation into leads is now allowed to warm the ocean as it would at open ocean grid squares, and all other surface heat fluxes into leads are split, so that a fraction of them equal to the ice concentration is used to form/melt ice by the ice model. The remainder is applied to the ocean model.

Coupling and flux adjustments

The coupling cycle consists of a one-day integration of the atmosphere model during which fluxes of heat, momentum, water and wind-mixing energy are averaged followed by a one-day integration of the ocean model. In UKTR a longer, 5 day, coupling cycle was used. During the ocean leg, averaged atmospheric fluxes are supplied from the preceding atmosphere leg, with additional fluxes of heat and fresh water calculated to keep the ocean surface temperature (SST) and salinity (SSS) close to specified seasonally-varying reference climatologies. Without these 'flux adjustments', the coupled model would rapidly drift away from a realistic state. (See section 3 for further discussion of the spinup method and flux adjustment). An improvement over UKTR is that flux adjustment of sea ice is no longer required with the inclusion of sea ice dynamics and other changes. Keeping SST close to its reference climatology imposes a strong constraint on the sea ice areal extent, but the sea ice depth is free to adjust to a mutual equilibrium with the atmosphere and ocean in HADCM2.

Before commencing the control and climate change runs, flux adjustments are first calibrated by interactively computing Newtonian relaxation terms proportional to the differences between modelled SST and SSS and their reference climatological values on each timestep, and storing averages over 5 day periods. This is done during the spinup phase. The Newtonian relaxation constant for heat fluxes is 164 $W/m^2/K$, giving an e-folding timescale of 14.5 days for a 50 m mixed layer, and the relaxation constant for fresh water such that the relaxation timescale for SSS is the same as for SST. The reference climatologies for SST and SSS are taken from monthly mean Levitus (1982) conditions, without any adjustments to SST near sea ice as were made in UKTR. Some modifications are, however, made to Levitus salinities around Antarctica, as described in section 3. In the control and climate change runs, these calibrated flux adjustments (averaged over 25 annual cycles in this study) are applied as prescribed, non-interactive terms.

Summary

Table 3 briefly summarises the main differences between UKTR and HADCM2.

3 SPINUP

Review of spinup methods for coupled models

Before commencing a climate change study, it is usually necessary to allow the atmosphere and ocean to adjust or "spin up" to a mutual equilibrium state. The objective is to bring the model close to a stable equilibrium so that negligible climate drift is experienced in the control run which follows. Stability of the control run is necessary to obtain accurate statistics for the model climate, which is crucial in assessing the significance of climate change signals. However, systematic model errors mean that relaxation of the ocean surface to present day conditions and possibly adjustment of other surface fluxes ('flux adjustment') is generally employed to maintain a realistic climate during spin up. Even so, a slow adjustment of the ocean state still occurs on century timescales as it finds an equilibrium with the surface forcing. If the model is run without flux adjustment, although the model will still reach an equilibrium state, it will have

a less realistic climate than with flux adjustment, casting doubt on conclusions from climate change experiments with such a model. It remains an open question whether flux adjustments themselves introduce more or less distortion than the inaccuracy resulting from leaving them out in any given model.

The intermediate and deep ocean have by far the longest spinup times of any part of the model. Meehl (1995) discusses the rationale and some generic approaches for ocean spinup in coupled models. One approach (eg. Manabe et al. 1991, Cubasch et al. 1992, Murphy 1995) is to spin up the atmosphere and ocean separately, using average forcing from the atmosphere model to spin up the ocean while restoring SST and SSS (and possibly other quantities) towards specified values. Towards the end of the spinup, the components may be recoupled for a short period and flux adjustments calibrated (Murphy 1995), or alternatively the calibration of flux adjustments may be done towards the end of a long ocean-only spinup phase without recoupling (Manabe et al. 1991).

Spinning up the components mainly independently (the 'uncoupled' method) is computationally much cheaper than spinning up coupled throughout when (as is usually the case) the ocean is considerably cheaper than the atmosphere to integrate. It may also allow the use of techniques to reduce the computer time needed to reach a statistical equilibrium in the ocean (Bryan 1984). However, this approach was not used in the present study, for two reasons. Firstly, the accelerated integration technique of Bryan (1984) did not work satisfactorily in our model (see below). Secondly, the model equilibrium state is sensitive to changing from a coupled spinup to ocean-only spinup even with strong restoring conditions on SST and SSS, which led us to use a coupled spinup to avoid consequential climate drift. These two points are discussed below.

Use of accelerated ocean integration techniques

An initial attempt to spin up with a preliminary version of the ocean model (without sea ice dynamics) was performed using the accelerated integration techniques of Bryan (1984). After an accelerated integration of the model to equilibrium, switching to unaccelerated integration resulted in a rapid drift away from the accelerated equilibrium solution. Certain aspects of the model physics interacted to produce 'accelerated' solutions which were significantly different from corresponding 'unaccelerated' ones. Further detailed investigations identified three interactions specific to the ocean model (and resulting drifts).

i) Isopycnal diffusion with 'accelerated' dynamics (which caused variability and drift in the Antarctic Circumpolar Current).

ii) Isopycnal diffusion with convection (giving drift in the Greenland Sea).

iii) The mixed layer model with the Richardson number dependent diffusivity and implicit vertical diffusion solver (giving drift at the base of the tropical mixed layer).

Since the integrations reported in this paper were run, modifications have been developed which allow the accelerated integration technique to be used while retaining essentially the physics described in this paper (Wood 1996). The technique is only appropriate for ocean-only spinup, however, which means it still may not help in the spinup due to the sensitivity discussed below.

Sensitivity to coupled versus ocean-only spinup

The spun-up state of the model was found to be sensitive to the form of spinup integration used. In essence, with relaxation conditions on SST and SSS the ocean and sea ice state attained in coupled spinup mode differs from that in ocean-only mode forced with seasonally varying time-averaged fluxes calibrated in a coupled spinup phase. This supports the conjecture of Power (1995) that residual climate drift is likely if the components in a coupled model are equilibrated separately, since forcing extremes and coupled interactions should contribute to determining the mean state if the coupled model behaves non-linearly and has high internal variability. For example, there are significant differences between the equilibrium sea ice thickness in the coupled

spinup integration used in this study and in a parallel ocean-only spinup. The ocean-only spinup was run for 170 years, starting from the end of the coupled spinup, and forced by seasonally varying surface fluxes averaged from the last 20 years of the coupled spinup, without using the acceleration methods mentioned above. It shows systematically thicker ice than the coupled spinup in regions of thermodynamic formation and slightly thinner ice in regions where ice is imported by the drift dynamics (Fig 1b), the differences being considerably larger than the interdecadal standard deviation in the coupled control run (Fig. 1a). A similar trend is seen in the Arctic sea ice. Differences are also found in the response of the ocean mixed layer, which is sensitive to extremes of turbulent wind mixing and buoyancy forcing. These sensitivities are probably encouraged by the high level of atmospheric variability in the model (see Section 5).

Since the non-linearities in this model are probably a true reflection of the essential physics of the real system, reformulating the model in such a way that it behaves more linearly is not justifiable simply to allow the use of cheaper un-coupled spinup methods. Hence we carried out the spinup in a coupled way to allow as much as possible of the coupled variability and extremes of forcing to be sampled. Other coupled models which are formulated with non-linear physics might also require a coupled spinup phase to avoid climate drift, although the severity of the drift associated with inadequate sampling of variability during spinup may be acceptable, depending on the model and application.

Rahmstorf and Willebrand (1995) claim that a form of ocean surface boundary condition representing non-local thermal feedbacks in the atmosphere could be applied in ocean-only spinup. If calibrated correctly this technique might improve the chances of using an ocean-only spinup successfully. However, it only represents a particular category of feedback and may therefore not be a complete solution. For example, sensitivity in the sea ice equilibrium state as found in our model and in a different type of model by Stössel et al. (1990) may arise through separate dynamic/thermodynamic mechanisms. It is possible that using statistically sampled stochastic forcing could work in ocean-only spinup, but this would still neglect coupled interactions between anomalies in ocean, ice and surface forcing. We have not investigated the stochastic forcing approach in the present model.

Spinup method used in the present study

Starting from Levitus (1982) climatological September values for oceanic potential temperature and salinity, with zero currents, we performed most of the spinup phase in a fully coupled way, alternating between relaxation boundary conditions on SST and SSS and using flux adjustments calibrated in a preceding relaxation phase (as illustrated in Fig. 4). We spun the model up for 510 years, rather than to full equilibrium, for reasons of computational economy. Reference SST and SSS climatologies used during the relaxation phases of the spinup are based on Levitus surface conditions. This method ensures that the model state is consistent with the forcing used, because the system experiences most of the modes of variability likely in the subsequent control run. Even so, there is strong damping of modes of SST and SSS variability on timescales longer than a few weeks (eg. ENSO-like oscillations) during phases which use relaxation conditions, and some readjustment occurs on changing from relaxation to flux adjustment boundary conditions at the start of the control run. Relative to internal variability over 200 years of the control run, this initial readjustment is most noticeable in parts of the subtropical mixed layer and under Antarctic sea ice (Fig. 2), regions which are also sensitive to ocean-only versus coupled spinup. Fortunately, it appears to be a transient effect and does not lead to a long term drift at the atmosphere-ocean-sea ice interface (see Section 5).

Surface salinities near the Antarctic continent in the Levitus (1982) climatology are probably too fresh in austral winter (being biased towards summer values due to the lack of wintertime observations in the region). England (1992, 1993) demonstrated the potential sensitivity of an ocean model's deep water mass structure and characteristics, particularly of Antarctic Bottom Water (AABW), to the reference surface salinities in winter in this region. We therefore undertook a series of short experiments with an ocean-only version of the coupled model to attempt to

tune the reference salinities to improve the AABW characteristics (which tended to be too warm and fresh using the unadjusted reference salinities). The details of the adjustments adopted are summarised in Table 4. Despite the relatively localised changes (confined to a few degrees of latitude around Antarctica), the thermohaline overturning cell in the Southern Ocean is markedly stronger (Fig. 3) as found by England (1993). Although these runs were quite short (50 years), the intermediate and bottom water mass characteristics appear better with the adjusted forcing, and the evidence from the coupled model spinup is that the bottom water does not warm as in UKTR (Fig. 4 - compare Murphy 1995 Fig. 3; see also Section 5), indicating that AABW is forming with about the right temperature in the model.

4 EXPERIMENTAL DESIGN

To model climate change since the mid nineteenth century one would like to start with the model in an equilibrium state resembling pre-industrial conditions.

In practice, this is not possible with the present model. If flux adjustments are omitted, it quickly develops unacceptably large systematic errors which would cast serious doubt on conclusions from a climate change experiment. However, using flux adjustments requires a lengthy spinup with relaxation of SST and SSS towards reference values in order to achieve equilibrium in the ocean. SST and SSS values appropriate for pre-industrial conditions are not well known, so we must instead use present day SSTs and SSSs in this case. Even with relaxation at the ocean surface, the interior ocean state develops quite large differences from present day observed conditions (which are probably not very different from pre-industrial conditions for much of the ocean). This would be the case irrespective of whether pre-industrial or present day reference SST and SSS values were used.

We therefore accept that systematic errors in the model equilibrium state are inevitable, but attempted to minimise drift in the control run using a long spinup and flux adjustment, since this is crucial in determining accurate statistics for the model climate. We assume that the model's sensitivity to changes in relative forcing is not significantly affected by systematic differences between its equilibrium state and the unknown pre-industrial state.

For consistency with SST and SSS forcing, present day rather than pre-industrial levels of equivalent carbon dioxide were used during the spinup.

The climate change study consists of a control run initialised from the end of the 510 year spinup, and two anomaly runs initialised after 10 years of the control (nominally 1860). Since the control run's climate should resemble present day conditions, it is possible to verify it against reliable climatologies and assess its systematic errors.

Forcing perturbations applied relative to the control in the anomaly runs represent anomalous forcing since the pre-industrial period. The difference between anomaly and control run responses then represents the 'signal' or 'climate change' relative to pre-industrial climate. Provided the spinup leads on to a stable control simulation, this approach allows a clear interpretation of changes in anomaly runs, even with the low levels of forcing believed to have occurred over the last century. We prefer this approach to attempting to correct the initial state to an earlier epoch prior to starting the experiment as done by Cubasch et al. (1995), because such a correction procedure may itself introduce a contaminating signal into the model.

The control run was initially integrated for 140 years (nominally 1850-1990) and has now been extended beyond 1000 years (Tett et al. 1996). The first 10 years are neglected as the model shows evidence of adjustment from the spinup phase (Fig. 2), and the control simulation is assessed against present climate mainly using 130 year averages (nominally 1860 to 1990) unless otherwise stated.

The anomaly runs are forced with the estimated evolving radiative forcing changes since 1860. By applying relative changes in forcing since the start of the instrumental temperature record (Houghton et al. 1990; Houghton et al. 1992), we can verify the time dependent response of the model against real climate change over an extended period which is reasonably well observed. The 1990 predictions from the simulations are used as initial conditions for future

prediction studies (Mitchell et al. 1995b; Mitchell and Johns 1996) thereby taking account of the past history of forcing and so largely avoiding the 'cold start' error (Hasselmann et al. 1993), although there is a small residual cold start effect from the initial forcing increment at 1860.

5 CONTROL CLIMATE

Stability of the modelled climate

Although oceanic temperature and salinity were still slowly adjusting at the end of the spinup, the transition into the control run (Fig. 4) is much smoother than in UKTR. There are residual trends of +0.02 K/century (equivalent to an average flux of about 0.1 W/m^2 over the ocean surface) and -0.002 psu/century in global mean oceanic temperature and salinity during the first 400 years of the control run. The temperature drift is relatively small compared with changes introduced in perturbed runs, but leads to a slow linear trend in global mean sea-level of about +1.5 cm/century due to thermal expansion.

The model shows a negligible long term trend in surface air temperature over the first 400 years of its control integration (Fig. 5). The best-fit linear trend in global average surface air temperature over the first 400 years is +0.01 K/century (+0.016 K/century over the first 1000 years; see Tett et al. 1996), similar to that reported by Stouffer et al. (1994) for a 1000 year run of the GFDL model from a fully equilibrated ocean initial state, and much less than that in the control simulation of UKTR (Murphy 1995). Hemispheric sea ice areal coverage and volume (Fig. 6) are also stable over this period, although with considerable interdecadal variability, particularly in Southern Hemisphere (SH) sea ice volume which shows peak-to-peak changes of order 20%.

Global energy budget, poleward energy transport and cloud forcing

The model achieves a creditable simulation of the top of atmosphere (TOA) radiation budget in comparison with data from the Earth Radiation Budget Experiment (ERBE) (Harrison et al. 1990). There is too little net downward shortwave radiation in both hemispheres in mid-latitudes, especially during summer when the incoming solar radiation is greatest (Fig. 7a). Outgoing longwave radiation (OLR) is too low throughout the year at these latitudes (Fig. 7b). These errors are associated with too much cloud or too high a value of cloud albedo in the storm tracks and over northern continents. In the tropics too little shortwave radiation is reflected throughout the year. The error is largest in the oceanic sub-tropical stratocumulus areas off the western coasts of South America, Africa and California where the model produces too little cloud, a problem common to many contemporary models. The OLR is too large over the equator, possibly due to too low a value of cloud emissivity. Errors in the shortwave and longwave components tend to compensate each other at most latitudes.

As evident above, clouds play a key role in determining the Earth's radiation budget and cloud-related feedbacks represent a major source of uncertainty in determining the magnitude of climate change. The effect of clouds on the present day radiation balance can be assessed by considering the cloud radiative forcing (the difference in radiative fluxes between clear and cloudy conditions with the same profile of temperature and radiatively active gases). The seasonal variation in cloud forcing in the model, expressed as the difference between January and July (Fig. 8), shows considerable agreement with the ERBE data. The simulation is an improvement on UKTR (Fig. 8, dot-dashed line) in mid-latitudes, where the seasonal cloud shifts are better represented.

Poleward energy transport by the whole system (Fig. 9) is simulated accurately, as expected given the fairly accurate TOA fluxes. Compared with transports derived from ERBE fluxes, the model underestimates the peaks slightly, but is within a few tenths of a PW of ERBE at all latitudes - a very creditable performance compared with results from lower resolution atmospheric models (Stone and Risbey 1990; Colman et al. 1994). However the modelled oceanic transport (Fig. 9) is considerably lower than suggested by observational estimates (eg.

Trenberth and Solomon 1994). The implied ocean transport from the modelled surface fluxes into the ocean is in rather better agreement with the Trenberth and Solomon estimate, the heat flux adjustment accounting for the difference. Given that the ocean meridional transport implied by the atmospheric flux at the ocean surface is rather sensitive to cloud radiative forcing (Gleckler et al. 1995), this supports the view that cloud radiative forcing is well simulated, but the ocean model's transport is too weak. Estimates of ocean energy transport remain somewhat uncertain. Manabe et al. (1991) obtained a higher actual ocean transport than in the present model, but also lower than observed. Better schemes for oceanic mixing which parameterize sub-grid scale eddy transports (Danabasoglu et al. 1994; Gent et al. 1995) may help improve this aspect of coarse resolution models.

Atmospheric mean circulation, temperature and winds

For comparison, we use an updated version of the UKMO operational model analyses used in the intercomparison and model validation study of Bourke et al. (1991), and by Murphy (1995). In this case we use average analyses between May 1983 and September 1995, although some upper air and near surface levels are averages only since January or September 1986. The UKMO analyses are broadly similar to ECMWF and NMC analyses.

Mean sea level pressure is generally well modelled in comparison with the UKMO analysis (Fig. 10), and is better than in UKTR (cf. Murphy 1995 Fig. 25). Relative to the analysis, the positioning and shape of the major equatorial low pressure belts, subtropical highs and mid-latitude low pressure systems is quite accurately reproduced in both DJF and JJA seasons. The pressure gradient over western and northern Europe in DJF is still too weak, associated with a relatively weak Icelandic low and Siberian high, indicating insufficient propagation of storms into this region, but is clearly improved from UKTR. Apart from the Aleutian low being rather too deep in DJF, the Northern Hemisphere (NH) pressure pattern is well simulated in the Pacific sector. The Azores high in DJF is displaced eastward, being centred more over the Mediterranean. The Antarctic circumpolar trough is too deep in both seasons, with overly strong westerly winds in the Southern Ocean. As in UKTR, the Asian monsoon trough extends too far east over the Pacific.

Zonal mean atmospheric temperatures and zonal winds in DJF and JJA (Fig. 11, Fig. 12) show errors relative to the analysis which are similar to those seen in atmosphere-only simulations driven by climatological specified SSTs and sea ice. The main error is a general cold bias in the troposphere in both seasons which peaks at about -6 to -8K at the tropical tropopause, with warm errors of similar size in the stratosphere. There is corresponding excessively strong easterly flow in the equatorial stratosphere, extending into the summer hemisphere, in both seasons. The lower troposphere north of 45N is too warm by 1 to 3K in DJF. A lens of very large cold errors, up to -12K, exists poleward of the SH jet core in DJF. This feature is present to a reduced extent and shifted towards the equator in JJA. In both seasons it is associated with excessive zonal winds at upper levels on the equatorward side, and in JJA with a large negative wind bias in the stratosphere south of 50S. In the NH, zonal wind errors are generally small in JJA, and temperature errors in the lower troposphere are generally less than 2K, but a cold lens is present in the upper troposphere polewards of 50N similar in character to that seen in the SH in DJF.

The meridional circulation in DJF and JJA (Fig. 13) is generally realistic, reproducing the observed Hadley, Ferrel and polar cells, with a prominent narrow rising branch on the summer hemisphere side of the equator and descending motion at around 30 degrees latitude in the winter hemisphere. The overall strength of the Hadley cell is good (about 10% too high) compared with the circulation implied from UKMO analyses of winds on pressure levels (eg. Murphy 1995 Fig. 27), and considerably stronger than UKTR. Latitudinal divisions between the cells are also generally accurate, but the Hadley cell extends too high in the tropics, with most of the cross-equatorial transport above 200 mb rather than below. The north-south seasonal shift in the main rising branch of the Hadley circulation is also slightly too great.

Overall, the model circulation and temperature structure is quite good compared with analyses and with other atmospheric models of comparable resolution (eg. Bourke et al. 1991; Boer et al. 1991) but the meridional circulation is a little too strong in the tropics, and the positioning and strength of the main jets show significant errors in both hemispheres, associated with systematic temperature biases.

Atmospheric synoptic variability

One measure of synoptic scale variability is the time-filtered standard deviation of 500 hPa geopotential heights (e.g. Blackmon 1976). Applying a band-pass filter (isolating variability on timescales between 2 and 6 days), there is good agreement between the model and observed areas of maximum high frequency variability or "storm tracks" in the North Pacific and Atlantic and in the Southern Ocean (Fig. 14, Fig. 15). The modelled variability is too weak in the NH in DJF and the storm tracks are displaced south and west of their observed position, giving an error significant at the 99% level of confidence across most of the North Atlantic storm track (on applying a two-tailed student t test). The northward displacement of the storm track in JJA is realistically simulated in the Pacific but is too small in the Atlantic and the variability remains slightly lower than suggested by the analysis. In the SH, the model produces a very realistic simulation in DJF in contrast to a 50% underestimate in UKTR (see Murphy 1995 Fig. 26), but has too large values in JJA, consistent with the exaggerated mean depth of the circumpolar trough (Fig. 10).

A synoptic cyclone counting technique based on that of König et al. (1993) has been applied to 10 years of daily mean sea level pressure data for points north of 30N (Fig. 16). The method is described by Carnell et al. (1996). In addition to the Pacific and Atlantic storm tracks there is a region of considerable cyclone activity over the Mediterranean in HADCM2, UKTR and the analysis, which does not show up using the band-pass filter of 500 hPa height. The cyclone tracks extend too far south and are more zonal (Fig. 16a) than is observed (Fig. 16b) in both of the oceanic storm track areas. In the eastern Atlantic the orientation of the cyclone tracks is rather better in HADCM2 than in UKTR (Fig. 16c), with a reduced number of lows over north west Europe. Both models simulate a maximum in the north west Pacific which is not in the analysis. This emanates from the Okhotsk Sea, where the climatological SSTs in the Levitus dataset are probably too high (R.J. Stouffer, pers. comm.) possibly encouraging cyclonic development. However, Boyle (1994) also reports a spurious maximum in the region, attributed in part to terrain effects, in a model forced with AMIP SSTs and sea ice.

On longer timescales of 10 days to a season (not shown) the variability is also generally improved over UKTR. In the NH, HADCM2 simulates the position and strength of the observed maximum low-frequency variability reasonably well in both DJF and especially JJA, although the Atlantic maximum in DJF is south and west of its observed position, consistent with the positional error of the storm track. The variability is larger than observed over the UK and north west Europe in both seasons but is quite realistic in the SH. A blocking index that uses the existence of an anomalous high in the 500 hPa geopotential height field at a particular latitude (Tibaldi and Molteni 1990) shows that the frequency of blocking in the model is considerably greater at all longitudes than in UKTR, which had very few blocks with little longitudinal variation, and in quite good agreement with the analyses (Fig. 17). The peak in the Pacific is well placed in the model, though smaller than in the analyses. In the Atlantic region some of the blocks are shifted westward, consistent with the westward shift in the variability and cyclone tracks.

The greater synoptic variability in HADCM2 is most likely to arise from the changes to the formulation of the dynamics scheme. Cullen and Davies (1991) demonstrate that the new scheme gives significantly higher average total, zonal and eddy kinetic energy than in the previous model. Other aspects of the model's variability are discussed by Tett et al. (1996).

Precipitation, soil moisture and the hydrological cycle

The model captures the main features of DJF and JJA precipitation (Fig. 18, Fig. 19; cf. Boer et al. 1991) as shown by precipitation maxima in the inter-tropical convergence zones, South Pacific and storm track regions of the North Atlantic and Pacific and Southern Oceans. The model also captures the dry subtropical regions well. Zonal average precipitation in the model agrees well with the climatology of Legates and Willmott (1990) in most of the NH, but agrees less well in the tropics and particularly the SH, where the DJF precipitation appears deficient (Fig. 18). However, the SH errors should be viewed in the context of the uncertainties in the climatological estimates there, as evidenced by discrepancies between the Legates and Willmott (1990) and Jaeger (1986) estimates. Relative to Legates and Willmott, the largest model errors occur on the western side of the American continent where there is high orography close to the ocean, the model simulating excessive precipitation over the high ground. Over Indonesia the model produces too little precipitation, with errors up to 5 mm/day. Over the Himalayas and central Africa there is probably too much precipitation, which may be partly due to the numerical diffusion of moisture up steep slopes (along model grid surfaces). The South Asian summer monsoon is broadly captured, but the peak in precipitation is shifted too far south over the Bay of Bengal, leaving much of India and China too dry. These precipitation deficiencies are reflected in rather low soil moisture contents in these regions in JJA, but simulated soil moisture content in DJF and JJA (Fig. 20) otherwise appears to be generally reasonable, delineating the moist tropics, subtropical arid areas, mid-latitude moist zones and their seasonal shifts quite well.

A land-only climatology (Hulme 1992) has been used by Airey et al. (1995) to validate terrestrial precipitation patterns from the model. They also compare the model performance with UKTR and two earlier atmospheric GCMs used at the Hadley Centre. HADCM2 shows a general improvement in accuracy in representing monthly global patterns over the earlier models, and in particular a better simulation of the South Asian summer monsoon, although there is not a universal improvement in all regions throughout the year. Inclusion of convective downdraughts in the model is the main source of the improvement in the tropics (D. Gregory, manuscript in preparation, 1995).

The global average precipitation in the model (3.0 mm/day in DJF, 3.1 mm/day in JJA) is about 0.5 mm/day lower in DJF and 0.2 mm/day higher in JJA than suggested by Legates and Willmott (1990), but there is considerable uncertainty in observed values over the oceans. Relative to the land-only Hulme (1992) climatology for 1951 to 1980, however, over the land areas covered by the climatology the model overestimates DJF precipitation by about 0.2 mm/day, but underestimates it by 0.3 mm/day in JJA.

Model river flows are parameterized simply by taking all excess runoff in a river basin and discharging it instantly into the ocean at a single outflow grid point. There are some large apparent errors between modelled and observed annual mean flows of the 15 largest model rivers (Table 5; observed flows are identified from Dumenil et al. 1993). One possible reason is that errors in the model precipitation give rise to large integrated river flow errors. To see if this is the case, the precipitation differences between the model and the Legates and Willmott (1990) and GPCC (1993) observational datasets are converted to a percentage of the model river flow for each of the 15 model river basins (Table 5, last two columns). Both of these climatologies are spatially complete over land allowing a direct comparison of integrated river basin quantities. In most cases, the rainfall error explains some of the difference between the modelled and the observed river flows. However, the precipitation related errors are insufficient to account for all the differences (eg. the discharge from the Ganges and Niger is very much lower than the model predicts, even though the precipitation errors are relatively small). This suggests that modelled river flows should be improved overall by a more accurate precipitation simulation, but a more sophisticated river model (eg. incorporating river dynamics, irrigation, flooding, and evaporation from rivers and flood plains) and better soil hydrology may be required to improve certain river flows.

Snow cover

Snow cover is difficult to validate globally, and the sub-grid scale inhomogeneity in the observations adds to the difficulty in comparing against modelled fields. Satellite observations for the NH, supported by ground-based calibration (Matson et al. 1986) suggest an areal coverage of 44.7 and $7.8 \times 10^{12} m^2$ in DJF and JJA respectively. There is no obvious relationship between the satellite measurements (based on frequency of cover) and model simulated values (depth). However, using a cutoff of 10 mm water equivalent, the model values of 35.3 and 5.1×10^{12} m^2 represent the summer/winter ratio well, as well as being generally reasonable in absolute terms.

Atmosphere heat, water and momentum fluxes into ocean

Zonally averaged net seasonal fluxes of heat and fresh water into the ocean for DJF and JJA are broadly similar to observational estimates (Fig. 21, Fig. 22). The observational estimates in these figures (from Esbensen and Kushnir 1981; Jaeger 1976) are subject to large uncertainties polewards of 60N and 45S. There are nevertheless some large discrepancies in the tropics and subtropics, particularly in the simulated water flux in JJA, which has its maximum further north of the equator and an excess of net evaporation to the south. There is also larger heat loss in the NH in DJF up to about 45N. It is apparent that while the seasonal heat flux adjustments are generally small in magnitude compared with the heat flux at a given latitude, this cannot be said for water flux adjustments, emphasizing the relative difficulty of reproducing observed seasonal changes in ocean salinity compared with temperature.

DJF and JJA zonal mean westerly windstresses (Fig. 23) compare quite well with observational estimates (Hellerman and Rosenstein 1983), with generally consistent patterns in both seasons. In DJF, the apparently weak stresses between 20N and 30S may be more due to a systematic overestimate in the observations (Stockdale et al. 1993), but poleward of 50N the model stress is too easterly. In JJA, there is a 5-10 degree northward shift of the pattern between 30N and the equator, consistent with a northern bias in the mean location of the ITCZ. In both DJF and JJA, but particularly JJA, the model stresses in the SH mid latitude belt appear too strong, consistent with the deep circumpolar trough and consequently high geostrophic winds. However, the observational estimates are themselves subject to some uncertainty in view of corrections to both winds and drag coefficients (Isemer and Hasse 1987). Note that while heat and water fluxes are adjusted, momentum fluxes are not, so the model's windstress errors are seen by the ocean.

Heat and fresh water flux adjustments

Despite the changes in the model components and spinup method, annual mean flux adjustment fields (Fig. 24) bear a strong resemblance to those in UKTR. Although there is a reduction in the area weighted means, area weighted RMS flux adjustments are actually higher on average in HADCM2 (Table 6).

As in UKTR, large positive heat flux adjustments occur in the northwest Atlantic and to the north of the UK, with large negative values towards the coasts of North America and Greenland. These errors are attributable to a combination of the model's inability to maintain the horizontal gradients near the Gulf Stream and insufficient exchange of water masses across the Greenland-Scotland ridge, both of which are mainly a consequence of the low horizontal resolution employed in the ocean model. In the Southern Ocean there are locally large heat flux adjustments of both signs, similar in magnitude to UKTR though with a more negative bias in the Atlantic sector, but the structure in the pattern may be partly attributable to roughnesses in the Levitus (1982) SST climatology due to poor data coverage in the region. The model requires large negative heat adjustments along the western coasts of South America and Africa due to a combination of a lack of marine stratus and upwelled water not being cold enough due to a weak vertical temperature gradient.

Large fresh water flux adjustments are strongly correlated with large heat flux adjustments, especially where there are strong horizontal gradients. Even though the model now includes river runoff and Mediterranean outflow explicitly, there is little impact on the global patterns away from the outflow points themselves. There are some differences compared with UKTR in the sea ice regions, as might be expected, since transport of fresh water in the form of ice is now represented. The adjustments adjacent to Antarctica are larger than in UKTR, perhaps as a result of systematic net sources and sinks of ice from including ice dynamics, but in the more dynamically confined Arctic Ocean the negative fresh water flux adjustments are smaller than in UKTR.

Oceanic temperature and salinity, and meridional circulation

The main thermocline is too thick compared with Levitus (1982), in common with other models of this type (e.g. Manabe et al. 1991; UKTR), resulting in temperatures being too warm at most depths (Fig. 25; Table 7). At mid depth the errors are somewhat greater than in UKTR, probably as a result of the higher value of background vertical diffusivity, although the isotherms do slope upwards from North to South more realistically. Below 4000m though, the model is cooler than both UKTR and Levitus, due to the strong circulation of bottom water in the present model (see below). The salinity structure (Fig. 26) shows an improvement over UKTR in that the tongue of low salinity Antarctic Intermediate Water is well reproduced, although the tongue is a little too thick, resulting in a fresh bias in the SH at mid depths. Globally, the model is somewhat fresh near the surface and at intermediate depths, but a little too saline at the bottom (Table 7).

Aspects of the global scale circulation are summarised by the streamfunction of the zonally integrated meridional volume transport for the globe and Atlantic basin (Fig. 27). The main features are:

i) a number of shallow, wind-driven cells associated with the tropical current systems and subtropical gyres.

ii) a mid-depth overturning cell in the Atlantic sector, associated with the production of North Atlantic Deep Water (NADW) by thermohaline forcing at high latitudes.

iii) the so-called 'Deacon Cell' at depths of 0-2000m, centred on 45S. This cell is largely a manifestation of the subduction of fluid along sloping isopycnals in the subtropical gyre (Döös and Webb 1994; Karoly et al. 1996). It plays an important role in the uptake of heat under conditions of climate change. Recent work has suggested that the strength of this cell may be sensitive to the way in which mesoscale eddy processes are parameterised in the model (Danabasoglu et al. 1994); however it was not possible to investigate this question in the present study.

iv) a deep overturning cell near Antarctica, associated with production of AABW. Some of the AABW escapes below the depth of the Drake Passage sill to join a large scale cell from 3000m depth to the bottom, which penetrates into the NH.

The circulation differs from that of UKTR in several respects. Most notably, the NADW and AABW overturning cells are stronger in the present model, and the bottom water cell (14 Sv here) was non-existent in UKTR. These differences can be attributed to the increased vertical diffusivity at depth (R. A. Wood, manuscript in preparation, 1995) and the modified reference salinities used to spin the model up (Section 3). The mass transport of the NADW cell at 24N is about 16 Sv, comparable with the estimate of 17 Sv by Roemmich and Wunsch (1985). The poleward heat transport across this latitude in the Atlantic is 0.8 PW, a little low compared with the observational estmate of 1.2 ± 0.3 PW (Hall and Bryden 1982).

Sea ice areal coverage

To sustain a realistic ice climatology in the model it is necessary to apply a heat flux adjustment to the ocean, even though the inclusion of ice dynamics removes the need for a direct flux

adjustment to ice itself. With flux adjustment used, the modelled ice climatology is fairly satisfactory, as can be seen from comparing climatological timeseries of the total ice area in the model and observations from the GISST 2.2 dataset for 1961-1990 (Rayner et al. 1995; see also Parker et al. 1994a) (Fig. 28). The GISST 2.2 dataset has observed or interpolated ice concentrations in tenths for each month, but this discretization can be neglected when using the climatology formed from thirty years of data. The comparison shows that the timing of the seasonal cycle is good, the extrema not occurring more than a month differently from in the observations, but the amplitude of the seasonal cycle is too large in the SH. There is a deficit in the area of ice in the autumn minima in both hemispheres (about 50% too little), and an excess during the Antarctic spring maximum (about 25% too much). The Arctic maximum is better simulated (about 20% too little ice).

Geographically, the Antarctic maximum ice edge advances too far, beyond 60S at all longitudes (Fig. 29). This could possibly be because of inadequacies of the thermodynamic formulation, particularly critical in the marginal ice zone; alternatively, it might be because the simple dynamical scheme, which does not represent sub gridscale inhomogeneity, tends to spread out the ice too far. The Arctic maximum ice area (Fig. 30) is more constrained by the bounding land masses, so it could be less sensitive to such model inadequacies. At the Antarctic autumn minimum, the ice edge retreats too close to the continent, whereas at the Arctic autumn minimum, the total ice area is less in error and the main source of the difficulty is that even near the pole the ice has broken up. This is probably related to the fact that the Arctic ice cover is too thin. Even in March, only a very small area exceeds 3 m in depth. Although there are no good comprehensive observational climatologies of ice depth we can be fairly sure that there should be substantial areas with ice of 4 m or more (eg. Bourke and McLaren 1992).

The excess of ice in the Antarctic winter and the deficit in Arctic summer are apparently reinforced by the heat flux adjustment. The largest values of the flux adjustment occur at high latitudes, and are mostly positive (into the ocean, hence melting ice) in the Arctic where there is too little ice, and negative (cooling and freezing the ocean) near Antarctica where there is generally too much ice. The fact that the flux adjustment tends to exaggerate the model errors suggests a need for improved thermodynamics or a better climatology of SSTs beneath ice.

6 SIMULATION AND VALIDATION FROM 1860 TO 1990

We have simulated past temperature changes using estimated forcing perturbations since 1860 to establish whether or not the model's sensitivity is consistent with the real climate system with an assumed forcing history. Estimates of past concentrations of greenhouse gases and sulphur emissions were used to derive the forcing over this period. Note that effects of changes in volcanic and biogenic aerosols, soot, ozone, the indirect effect of sulphate aerosols, and possible solar variations were not accounted for. Although the ability to simulate the recent observed record gives some credibility to a model, uncertainties in historical forcing (Houghton et al. 1994; Mitchell et al. 1995a) and models' sensitivities to increased forcing (Houghton et al. 1990; Houghton et al. 1992) are still large. Hence one could in principle produce a reasonable hindcast for the wrong reasons. For example, if the forcing estimate is too low but the model is too sensitive it might still reproduce the correct rate of warming in recent decades. Also, if the model sensitivity is correct but the reconstructed forcing is wrong the model might fail to reproduce the past record, even though it would have considerable predictive skill. However, the estimates of the net forcing and the climate sensitivity of the model used here are in the middle of the range of current estimates (Houghton et al. 1994; Houghton et al. 1992). Uncertainty as to the level of natural variability also makes it difficult to give an objective assessment of how well a model hindcast should fit the past record, even if the model, forcing and observations were perfect. In summary, ability to reproduce the past record does not necessarily guarantee that predictions of future climate will also be accurate.

The first of the runs (GHG) is forced with equivalent CO_2 changes relative to the control which mimic the change of forcing due to all greenhouse gases relative to pre-industrial levels

(Houghton et al. 1990). In the second run (SUL), additional (negative) forcing is applied which represents the direct radiative forcing due to anthropogenic sulphate aerosol by means of an increase in clear-sky surface albedo proportional to the local sulphate loading (see Mitchell et al. 1995a for details of the method). A spatial loading pattern for 1986 is used, with time-varying scaling coefficients computed to match estimated global burdens over the period (Dignon and Hameed, 1989; Hameed and Dignon 1992). The indirect effect of sulphate aerosols on cloud radiative properties (eg. Jones et al. 1994) is neglected. Note that there is an initial increment of 0.4 W/m^2 in forcing at 1860 relative to the control run (Fig. 31), representing the small increase in greenhouse gases from 1765 to 1860. The coupled model has an estimated equilibrium sensitivity of 2.5 K to doubling CO_2. 0.4 W/m^2 would give an equilibrium response of 0.25 K, most of which would be realised in the first few decades. Thus the cold bias in the twentieth century due to neglecting the effects of this forcing is likely to be less than 0.1K and diminishing with time. Up to about 1930 (slightly later in SUL), the forcing changes are relatively small. Only after this time is it likely that a forced response would be obvious compared with internal model variations. The global warming in GHG starts to become clear at about 1950, but a decade or two later in SUL, and Mitchell et al. (1995b; their Fig. 2a) demonstrate that agreement with the historical global mean temperature record is better in SUL than GHG. Sea level is predicted to rise by 6.5 cm in GHG and 4 cm in SUL from 1860 to 1990 due to thermal expansion of sea water, after subtracting the underlying (linear) trend in the control run.

Patterns of annual surface air temperature change over the 20th century (Fig. 32) show significant areas of cooling in SUL, especially in mid-latitudes, reminiscent of some of the cooling features in the observed. There is no obvious amplification of the warming in the Arctic in SUL. In contrast, GHG shows hardly any areas of cooling, and considerable amplification of the warming in high latitudes. Decadal temperature anomaly pattern correlations between GHG and SUL, and observed anomaly patterns, computed by Mitchell et al. (1995b; their Fig. 3) suggest that the signal defined by SUL is more consistent with observations in recent decades, showing a consistently high correlation with observed patterns both relative to GHG and a sampling statistic derived from the control run. This implies that SUL captures the observed signal of temperature changes better than GHG in the latter period, at which time the signal-to-noise ratio should be increasing. Here, we have reassesed the significance levels by fitting a normal distribution to the measured sampling distribution of correlations between each GHG/SUL decadal pattern and anomaly patterns from the first 40 decades of the control run (applying the appropriate observational mask before computing the correlations). This method of computing the significance level yields fewer samples in forming the sampling distribution, but gives a fairer estimate of the significance level without assuming anything about the degree of orthogonality between the model noise and signal patterns (B.D. Santer; pers. comm.). The only decades above the 10% significance level are the 1970's and 1980's in SUL (Fig. 33), strengthening the conclusion that SUL is more consistent with an emerging climate change signal in the observed than GHG.

The latitudinal distribution of warming with time (Fig. 34) shows some features in common between the simulations and observations (Parker et al. 1994b). The warming is generally a minimum around 45S throughout the period, a feature better represented in SUL than GHG, and there is large interdecadal variability in high latitudes. The most marked warming occurs in the last 20 years, though it is small near 45N. SUL is too warm at this latitude early in the period. The overall trend is too large in GHG, as one would expect from the global mean changes. Neither simulation captures the observed warming in northern mid and high latitudes between 1920 and 1940 very well; not surprising given the absence of a strong rise in model forcing during this time. Schlesinger and Ramankutty (1994) suggest that the warming was part of a temperature oscillation largely confined to the Atlantic and surrounding regions. North of about 25N the observed anomaly is larger than any seen over any period of comparable length in the first 400 years of the control simulation (Fig. 5). It is possible that the model underestimates internal variability, or the observed oscillation may have been driven by some forcing anomaly which has not been represented properly. For example, the modelled forcing does not reflect

the fact that cooling due to volcanic aerosols was anomalously low from 1920 to 1960, and anomalously high since (Sato et al. 1993). Such variations in 'natural' forcing are absent in the control integration as well, of course, tending to reduce its variability and thereby to lead to an underestimate of 'natural' variability.

Recent satellite-based observational estimates of changes in sea ice area over the last decade or so (Johannessen et al. 1995) indicate a statistically significant declining trend in Arctic ice cover from 1978 to 1987, becoming rather steeper since, but no significant trend in Antarctic sea ice over the period. GHG shows a significant declining trend in the Arctic of -0.046 x 10^6 km^2/yr (Fig. 35a), similar to the trends reported by Johannessen et al. (1995) (see Table 8), but SUL shows a slight increase, consistent with its coolness at high latitudes at this time (Fig. 34b). Both simulations show small (statistically insignificant) increasing trends in the Antarctic, consistent with the lack of a significant observed trend (Fig. 35b). In the Arctic, the simulated declining trend in GHG and the observed trend are significant when assessed against the variability of 15 year modelled trends, overlapped by 10 years, in the first 400 years of the control run. The maximum and minimum of 77 such trends are +0.028 and -0.039, with a mean of 0.001 and standard deviation of 0.017 x 10^6 km^2/yr, making the GHG simulated trend for the Arctic significant at the 1% level, but within 1 modelled standard deviation of the observed trends. The fact that GHG gives better agreement in this respect suggests that the NH sulphate forcing in SUL could be too strong, or the high latitude amplification of the sulphate aerosol cooling signal overdone. It is perhaps surprising that the agreement with the observed trend is so good in GHG given the poorer overall agreement between global temperature trends discussed above. The Arctic is a relatively small area, however, so more weight should be attached to the global temperature statistics than to Arctic sea ice trends.

Trends of zonal atmospheric temperature throughout the depth of the atmosphere may also be compared with observed data over the period 1963 to 1988. Observed trends (Fig. 36c) are derived from radio-sonde data (Oort 1983; Oort and Liu 1993). Both GHG and SUL (Fig. 36a,b) show tropospheric warming and stratospheric cooling trends over the period, SUL showing less tropospheric warming than GHG. Both experiments warm too rapidly in the equatorial troposphere at approximately 300 hPa and have the turnover from warming to cooling trends too high, at about 100hPa, compared with observations. Both model simulations also show "wings" of heating and cooling in the extra-tropics at 200 to 100 hPa. The origin of this phenomenon is not fully understood. It may be in part a spurious feature arising from the existence of undamped two-grid length vertical waves as a result of the centred vertical difference scheme. Similar features are seen in CO_2 simulations with some other models which partially resolve the stratosphere (Rind et al. 1990; Boer et al. 1992; Cubasch et al. 1992; Mahfouf et al. 1994). Tropospheric warming trends are generally less in the observations than the model with only weak similarity between the patterns. Above 200 hPa there is general cooling in the observations extending down to 600 hPa north of 45N, with a strong maximum over Antarctica extending down to 400 hPa. The latter feature is largely absent in GHG, but SUL does have a cooling maximum above 200 hPa, though still too weak. This aspect of the model simulations should be improved by representing changes in stratospheric ozone forcing (Santer et al. 1995).

7 CONCLUSIONS

It is evident that the control climate of the model described here is generally an improvement over its predecessor, despite suffering from some deficiencies. The control surface climate is stable on multi-century timescales, its stability compared with other such models (eg. Stouffer et al. 1994) demonstrating that full equilibration of the deep ocean is not necessarily a prerequisite. Indeed, allowing the atmosphere and ocean surface layers and thermocline to adjust to a mutual coupled state (over a few hundreds, as we have done, rather than many thousands of years) appears to be equally effective in achieving stability. This approach allows the model to experience most of the coupled modes of variability while adjusting, thereby minimising climate drift due to inadequate sampling of such coupled non-linear processes, as suggested by Power (1995).

The more accurate atmospheric dynamical scheme adopted in the model leads to an improved simulation of mean climate and its variability. Although significant atmospheric temperature errors still exist, the general circulation patterns are well simulated, with a more vigorous meridional circulation than in UKTR. Atmospheric synoptic variability shows significant improvements, particularly in northern hemisphere blocking and southern hemisphere storm tracks as well as improvements in some other regional details. Global precipitation patterns have been shown by Airey et al. (1995) to be statistically closer to observed terrestrial patterns than for any previous Hadley Centre climate model, mainly from including a representation of convective downdraughts, though not all areas are better throughout the year. Oceanic bottom water temperature is closer to Levitus (1982) values than in UKTR, mainly attributable to a more active thermohaline circulation around Antarctica giving more vigorous AABW formation. This feature was deliberately encouraged by modifying reference salinities in austral winter in high southern latitudes following work by England (1992, 1993).

Poleward energy transport by the atmosphere and ocean combined is within a few tenths of a PW of ERBE-derived estimates at the top of the atmosphere. Atmospheric net heat fluxes into the ocean also appear to be accurately simulated compared with observational estimates, implying accurate poleward transport by the atmospheric component of the model. However, poleward heat transport by the ocean component is too weak compared with recent observational estimates (Trenberth and Soloman 1994) despite having the correct general pattern. The missing ocean heat transport, due mainly to systematic errors in the ocean model related partly to low resolution, is largely compensated by the heat flux adjustment. Introduction of a simple sea ice dynamical scheme has removed the need for flux adjustments to ice as used in UKTR. The sea ice climatology is qualitatively quite good, being stable and with a strong seasonal cycle in both hemispheres, although the ice coverage is too low in the Arctic throughout the year, too low in Antarctic summer and too high in Antarctic winter.

These general improvements are in spite of higher RMS flux adjustments than in UKTR, illustrating that the size of flux adjustments, although a valuable measure, is only one aspect to be considered in assessing the overall performance of a coupled model.

We have assessed the model's sensitivity to changes in radiative forcing by validating its simulation against the 1860 to 1990 temperature record and recent trends in sea ice cover. For the first time, we have modelled the direct forcing effect of sulphate aerosols as well as that due to changes in greenhouse gases. Provided both forcings are represented, we have shown that the model can begin to reproduce observed temperature changes over the last few decades with reasonable accuracy. Although there are presently rather large uncertainties regarding the magnitude and variations of both sulphate aerosol forcing terms, as well as various other terms the effects of which cannot easily be estimated by modelling studies alone, it appears that the combination of the model's sensitivity and the imposed forcing (including aerosol effect) gives a reasonable fit to the observed temperature record, although recently reported Arctic sea ice trends are better simulated with greenhouse gases only. Since we have neglected the indirect aerosol forcing effect, which is expected to have a similar though not identical geographical pattern to the direct effect (Jones et al. 1994), it is possible that we have fortuitously scaled the indirect effect to represent the combined direct plus indirect effect (Wigley 1995). We have also neglected other possible effects including changes in volcanic and biogenic aerosols, ozone, soot and solar variability. Although one would not expect all the details of the observed temperature record to be captured faithfully even with all the forcing terms correctly represented, some notable discrepancies are apparent in the present study (especially between the mid 1930's and late 1950's), perhaps due to neglecting volcanic aerosol forcing.

Using historical forcing as a validation method for checking the sensitivity of coupled models against the observed climate record focusses attention on the need to improve understanding of the magnitude, spatial patterns and time variations of historical climate forcing. Although the present study suggests an improved simulation just with direct aerosol forcing added, it may prove necessary to include other forcings, especially indirect aerosol effects and stratospheric aerosol changes, before a convincing reproduction of the past record can be demonstrated. The

lack of a concensus between the temperature and sea ice trend validation results supports the need for further improvement of forcing histories. It will also be important to estimate the limit of determinism in an individual simulation of the past record by performing ensembles of such runs with identical forcing but perturbed initial states. Both of these will be addressed in future modelling studies.

ACKNOWLEDGEMENTS

The work was carried out under the UK Department of the Environment Climate Prediction Programme (PECD 7/12/37), with supplementary support from the Commission of the European Communities (contract EV5V-CT92-0123). R. Davis and A. Brady helped in creating the aerosol forcing datasets, and with J. Lavery assisted in developing analysis software and extracting diagnostics. The authors would also like to thank their many colleagues who helped in the development of the coupled model and the Unified Model software systems, and J. Murphy and H. Cattle for helpful comments on an early draft of the paper. We are also grateful to B. Santer (PCMDI) and G. Hegerl (MPI) for helpful suggestions and comments on statistical analysis of the simulations.

REFERENCES:

Airey MJ, Hulme M, Johns TC (1995) Evaluation of Simulations of Terrestrial Precipitation by the UK Met. Office/ Hadley Centre Model. Geophys Res Lett (submitted).

Arakawa A, Lamb VR (1977) Computational design of the basic dynamical processes of the UCLA general circulation model. Methods of Computational Physics 17: 174-265, Academic Press.

Blackmon ML (1976) A climatological spectral study of the 500mb geopotential height of the Northern Hemisphere. J Atmos Sci 33: 1607-1623

Boer GJ, Arpe K, Blackburn M, Deque M, Gates WL, Hart TL, Le Treut H, Roeckner E, Sheinin DA, Simmonds I, Smith RNB, Tokioka T, Wetherald RT, Williamson D (1991) An Intercomparison of the Climates Simulated by 14 Atmospheric General Circulation Models. WMO/TD-No. 425.

Boer GJ, McFarlane JNA, Lazare M (1992) Greenhouse-gas induced climate change simulated with the CCC second generation general circulation model. J Climate 5: 1045-1077

Bourke W, Mullenmeister P, Arpe K, Baumhefner D, Caplan P, Kinter JL, Milton SF, Stern WF, Sugi M (1991) CAS/JSC Working Group on Numerical Experimentation. Systematic Errors in Extended Range Predictions. WMO/TD-No. 444.

Bourke RH, McLaren AS (1992) Contour mapping of Arctic basin ice draft and roughness parameters. J Geophys Res 97: 17715-17728

Boyle JS (1994) The Northern Wintertime Divergence Extrema at 200 hPa and MSLP Cyclones as Simulated in the AMIP Integration by the ECMWF General Circulation Model. J Climate 7: 24-32

Bryan K (1969a) A numerical model for the study of the circulation of the world ocean. J Comput Phys 3: 347-376

Bryan K (1969b) Climate and the ocean circulation. III The ocean model. Mon Wea Rev 97: 806-827

Bryan K (1984) Accelerating the convergence to equilibrium of ocean-climate models. J Phys Oceanogr 14: 666-673

Carnell RE, Senior CA, Mitchell JFB (1996) An assessment of measures of storminess: Simulated changes in Northern Hemisphere winter due to increasing CO_2. Clim Dyn (accepted).

Colman RA, McAvaney BJ, Fraser JR, Power SB (1994) Annual mean meridional energy transport modelled by a general circulation model for present and 2xCO_2 equilibrium climates. Clim Dyn 10: 221-229

Charnock H (1955) Wind stress on a water surface. Quart J Roy Meteor Soc 81: 639

Cox MD (1984) A primitive equation, three dimensional model of the ocean. GFDL ocean group technical report no.1, Princeton NJ, USA, 143 pp

Cubasch U, Hasselmann K, Höck H, Maier-Reimer E, Mikolajewicz U, Santer BD, Sausen R (1992) Time-dependent greenhouse warming computations with a coupled ocean-atmosphere model. Clim Dyn 8: 55-69

Cubasch U, Santer BD, Hellbach A, Hegerl G, Höck H, Maier-Reimer E, Mikolajewicz U, Stössel A (1994) Monte Carlo climate change forecasts with a global coupled ocean-atmosphere model; Clim Dyn 10: 1-19

Cubasch U, Hegerl G, Hellbach A, Höck H, Mikolajewicz U, Santer BD, Voss R (1995) A climate change simulation starting 1935. Clim Dyn 11: 71-84

Cullen MJP (1993) The unified forecast/climate model. Meteor Mag 122: 81-94

Cullen MJP, Davies T (1991) A conservative split explicit integration scheme with fourth order horizontal advection. Quart J Roy Meteor Soc 117: 993-1002

Danabasoglu G, McWilliams JC, Gent PR (1994) The Role of Mesoscale Tracer Transports in the Global Ocean Circulation. Science 264: 1123-1126

Dignon J, Hameed S, (1989) Global emissions of nitrogen and sulfur oxides from 1860 to 1980. JAPCA (Journal of the Air & Waste Management Association) 39: 180-186

Dolman AJ, Gregory D (1992) The parametrization of rainfall interception in GCMs. Quart J Roy Meteor Soc 118: 455-467

Döös K, Webb DJ (1994) The Deacon Cell and Other Meridional Cells of the Southern Ocean. J Phys Oceanogr 24: 1281-1293

Dumenil L, Isele K, Liebscher H-J, Schroder U, Schumacher M, Wilke K (1993) Discharge data from 50 selected rivers for GCM validation. MPI Technical Report No 100, Max-Planck-Institut fur Meteorologie, Hamburg. 61 pp

England MW (1992) On the formation of Antarctic Intermediate and Bottom Water in ocean general circulation models. J Phys Oceanogr 22: 918-926

England MW (1993) Representing the global-scale water masses in ocean general circulation models. J Phys Oceanogr 23: 1523-1552

Esbensen SK, Kushnir Y (1981) The heat budget of the global ocean: An atlas based on estimates from surface marine observations. Climatic Research Institute Report No. 29, Oregon State University, 27 pp

Gates WL, Nelson RB (1973) A new tabulation of the Scripps topography on a 1 degree global grid. Part II: Ocean depths. Santa Monica, California, Rand Corp. Contract no. DAHC15-73-0181.

Gent PR, Willebrand J, McDougall TJ, McWilliams JC (1995) Parameterizing Eddy-Induced Tracer Transports in Ocean General Circulation Models. J Phys Oceanogr 25: 463-474

Gleckler PJ, Randall DA, Boer G, Colman R, Dix M, Galin V, Helfand M, Kiehl J, Kitoh A, Lau W, Liang X-Y, Lykossov V, McAvaney B, Miyakoda K, Planton S, Stern W (1995) Cloud-radiative effects on implied oceanic energy transports as simulated by atmospheric general circulation models. Geophys Res Lett 22: 791-794

GPCC (1993) Global area-mean monthly precipitation totals for the year 1988 (preliminary estimates, derived from rain-gauge measurements, satellite observations and numerical weather prediction results). WCRP/GPCP Report No. DWD/WZN-1993/07-1. Deutscher Wetterdienst, Offenbach am Main, 16 pp

Gregory D, Allen S (1991) The effect of convective scale downdraughts upon NWP and climate simulations. 9th conference on numerical weather prediction, Denver, CO, Amer Meteor Soc: 122-123

Gregory D, Rowntree PR (1990) A mass flux convection scheme with representation of ensemble characteristics and stability dependent closure. Mon Wea Rev 118: 1483-1506

Hall MM, Bryden H (1982) Direct Estimates and Mechanisms of Ocean Heat Transport. Deep Sea Res 29: 339-359

Hameed S, Dignon J (1992) Global emissions of nitrogen and sulfur oxides in fossil fuel combustion 1970-1986. JAPCA (Journal of the Air & Waste Management Association) 42: 159-186

Harrison EP, Minnis P, Barkstrom BR, Ramanathan V, Cess RD, Gibson GG (1990) Seasonal variation of cloud radiative forcing derived from the Earth Radiation Budget Experiment. J Geophys Res 95: 18687-18703

Hasselmann K, Sausen R, Maier-Reimer E, Voss R (1993) On the cold start problem in transient simulations with coupled atmosphere-ocean models, Clim Dyn 9: 53-61

Hellerman S, Rosenstein M (1983) Normal monthly wind stress over the World Ocean with error estimates. J Phys Oceanogr 13: 1093-1104

Hibler WD (1979) A dynamic-thermodynamic sea ice model. J Phys Oceanogr 9: 815-846

Houghton JT, Jenkins GJ, Ephraums JJ (eds) (1990) Climate Change. The IPCC Scientific Assessment. WMO-UNEP, Cambridge University Press, 366 pp

Houghton JT, Callender BA, Varney SK (eds) (1992) Climate Change 1992. The Supplementary Report to the IPCC Scientific Assessment. WMO-UNEP, Cambridge University Press, 200 pp

Houghton JT, Meira Filho LG, Bruce J, Lee H, Callender BA, Haites E, Harris N, Maskell K (eds) (1994) Climate Change 1994. Radiative Forcing of Climate Change. WMO-UNEP, Cambridge University Press, 339 pp

Hulme M (1992) A 1951-80 global land precipitation climatology for the evaluation of General Circulation Models. Clim Dyn 7: 57-72

Isemer H-J, Hasse L (1987) The Bunker climate atlas of the North Atlantic Ocean. Vol.2. Air-Sea Interactions. Springer-Verlag, Berlin, 252 pp

Jaeger L (1986) Monatskarten des Niederschlags fur die ganze Erde. Ber. Dtsche. Wetterdienstes 18 (139): 38 pp

Johannessen OM, Miles M, Bjorgo E (1995) The Arctic's shrinking sea ice. Nature 376: 126-127

Johns TC (1996) A description of the Second Hadley Centre Coupled Model (HADCM2). Climate Research Technical Note, Meteorological Office, Bracknell, UK (In preparation)

Jones A, Roberts DL, Slingo A (1994) A climate model study of indirect radiative forcing by anthropogenic sulphate aerosols. Nature 370: 450-453

Karoly DJ, McIntosh PC, Berrisford P, McDougall TJ, Hirst AC (1996) Understanding the Indirect Vertical Circulation Cells of the Atmosphere and Ocean. Nature (submitted)

König W, Sausen R, Sielmann F (1993) Objective Identification of Cyclones in GCM Simulations. J Climate 6: 2217-2231

Kraus EB (1990) Diapycnal Mixing. In: Climate-Ocean Interaction, ed. M.E.Schlesinger, Kluwer, Amsterdam, Netherlands, pp 269-293

Kraus EB, Turner JS (1967) A one dimensional model of the seasonal thermocline. Part II. Tellus 19: 98-105

Ledley TS (1985) Sea ice: Multiyear cycles and white ice. J Geophys Res 90: 5676-5686

Ledwell JR, Watson AJ, Law CS (1993) Evidence for slow mixing across the pycnocline from an open-ocean tracer release experiment. Nature 364: 701-703

Legates DR, Willmott CJ (1990) Mean seasonal and spatial variability in gauge-corrected, global precipitation. Int J Climatology 10: 111-128

Levitus S (1982) Climatological Atlas of the World Ocean. NOAA Professional Paper 13, National Oceanic and Atmospheric Administration, Rockville, MD, USA, 173 pp

Mahfouf JF, Cariolle D, Royer J-F, Geleyn J-F, Timbal B (1994) Response of the Meteo-France climate model to changes in CO_2 and sea-surface temperatures. Clim Dyn 9: 345-362

Manabe S, Spelman MJ, Stouffer RJ (1992) Transient Responses of a Coupled Ocean-Atmosphere Model to Gradual Changes of Atmospheric CO_2. Part II: Seasonal Response. J Climate 5: 105-126

Manabe S, Stouffer R (1988) Two Stable Equilibria of a Coupled Ocean-Atmosphere Model. J Climate 1: 841-866

Manabe S, Stouffer RJ, Spelman MJ, Bryan K (1991) Transient Responses of a Coupled Ocean-Atmosphere Model to Gradual Changes of Atmospheric CO_2. Part I: Annual Mean Response. J Climate 4: 785-818

Matson M, Ropelewski CF, Varnadore MS (1986) An atlas of satellite-derived northern hemispheric snow cover frequency. NOAA Atlas. US Department of Commerce, National Oceanic and Atmospheric Administration, 75 pp

Meehl GA, Washington WM, Karl TR (1993) Low-frequency variability and CO_2 transient climate change. Part 1. Time-averaged differences. Clim Dyn 8: 117-133

Meehl GA (1995) Global Coupled General Circulation Models. Bull Amer Meteor Soc 76: 951-957

Mesinger F (1981) Horizontal advection schemes on a staggered grid, an enstrophy and energy conserving model. Mon Wea Rev 109: 467-478

Mitchell JFB, Davis RA, Ingram WJ, Senior CA (1995a) On Surface Temperature, Greenhouse Gases and Aerosols: Models and Observations. J Climate 8: 2364-2386

Mitchell JFB, Johns TC, Gregory JM, Tett SFB (1995b) Climate response to increasing levels of greenhouse gases and sulphate aerosols. Nature 376: 501-504

Mitchell JFB, Johns TC (1996) On the modification of global warming by sulphate aerosols. J Climate (submitted)

Murphy JM (1995) Transient Response of the Hadley Centre Coupled Ocean-Atmosphere Model to Increasing Carbon Dioxide. Part I: Control Climate and Flux Adjustment. J Climate 8: 36-56

Murphy JM, Mitchell JFB (1995) Transient Response of the Hadley Centre Coupled Ocean-Atmosphere Model to Increasing Carbon Dioxide. Part II: Spatial and Temporal Structure of Response. J Climate 8: 57-80

Oort AH (1983) Global atmospheric circulation statistics. 1958-1973. Nat Oceanic Atmos Adm (US) Prof Pap 14.

Oort AH, Liu H (1993) Upper-air temperature trends over the globe. 1958-1989. J Climate 6: 292-307

Pacanowski RC (1987) Effect of Equatorial Currents on Surface Stress. J Phys Oceanogr 17: 833-838

Pacanowski RC, Philander G (1981) Parameterisation of vertical mixing in numerical models of the tropical oceans. J Phys Oceanogr 11: 1443-1451

Palmer TN, Shutts GJ, Swinbank R (1986) Alleviation of a systematic westerly bias in general circulation and numerical weather prediction models through an orographic gravity wave drag parametrization. Quart J Roy Meteor Soc 112: 1001-1039

Parker DE, Folland CK, Bevan A, Ward MN, Jackson M, Maskell K (1994a) Marine surface data for analysis of climatic fluctuations on interannual to century timescales. In: Natural Climate Variability on Decade-to-Century Time Scales. Martinson DG, Bryan K, Ghil M, Hall MM, Karl TR, Sarachik ES, Sorooshian S, Talley LD (eds). National Academy Press, Washington DC (in press)

Parker DE, Jones PD, Folland CK, Bevan A (1994b) Interdecadal changes of surface temperature since the late nineteenth century. J Geophys Res 99: 14373-14399

Power SB (1995) Climate Drift in a Global Ocean General Circulation Model. J Phys Oceanogr 25: 1025-1036

Power SB, Colman R, McAvaney B, Dahni R, Smith N (1993) The BMRC coupled atmosphere/ocean/seaice model. The BMRC Research Report No 37.

Rahmstorf S, Willebrand J (1995) The Role of Temperature Feedback in Stabilizing the Thermohaline Circulation. J Phys Oceanogr 25: 787-805

Rayner NA, Folland CK, Parker DE, Horton EB (1995) A new global sea-ice and sea surface temperature (GISST) data set for 1903-1994 for forcing climate models. Hadley Centre Internal Note no. 69. UK Meteorological Office, Bracknell, UK.

Redi MH (1982) Oceanic isopycnal mixing by coordinate rotation. J Phys Oceanogr 12: 1154-1158

Rind D, Suozzo R, Balachandran NK, Prather MJ (1990) Climate change and the middle atmosphere. Part I: The doubled CO_2 climate. J Atmos Sci 47: 475-494

Roemmich D, Wunsch C (1985) Two transatlantic sections: meridional circulation and heat flux in the North Atlantic Ocean. Deep Sea Res 32: 619-664

Russell GL, Miller JR, Rind D (1995) A coupled atmosphere-ocean model for transient climate change studies. Atmos-Ocean (accepted).

Santer BD, Taylor KE, Wigley TML, Penner JE, Jones PD, Cubasch U (1995) Towards the detection and attribution of an anthropogenic effect on climate. Clim Dyn 12: 77-100.

Sato M, Hansen JE, McCormick MP, Pollack JB (1993) Stratospheric aerosol optical depths, 1850-1990. J Geophys Res 98: 22987-22994

Schlesinger ME, Ramankutty N (1994) An oscillation in the global climate system of period 65-70 years. Nature 367: 723-726

Semtner AJ (1976) A model for the thermodynamic growth of sea ice in numerical investigations of climate. J Phys Oceanogr 6: 379-389

Simmons AJ, Burridge DM (1981) An energy and angular-momentum conserving finite-difference scheme and hybrid coordinates. Mon Weather Rev 109: 758-766

Slingo A (1989) A GCM parametrization for the shortwave radiative properties of water clouds. J Atmos Sci 46: 1419-1427

Slingo A, Wilderspin RC (1986) Development of a revised longwave radiation scheme for an atmospheric general circulation model. Quart J Roy Meteor Soc 112: 371-386

Slingo A, Wilderspin RC, Smith RNB (1988) The effect of improved parameterizations on simulations of cloudiness and the earth's radiation budget in the tropics. J Geophys Res 94: 2281-2301

Smith RNB (1990) A scheme for predicting layer clouds and their water content in a general circulation model. Quart J Roy Meteor Soc 116: 435-460

Stockdale T, Anderson D, Davey M, Delecluse P, Kattenberg A, Kitamura Y, Latif M, Yamagata T (1993) Intercomparison of Tropical Ocean GCMs. WMO/TD-No.545, 43 pp

Stone PH, Risbey JS (1990) On the limitations of general circulation models. Geophys Res Lett 17: 2173-2176

Stössel A, Lemke P, Owens WB (1990) Coupled Sea Ice-Mixed Layer Simulations for the Southern Ocean. J Geophys Res 95: 9539-9555

Stouffer RJ, Manabe S, Vinnikov KY (1994) Model assessment of the role of natural variability in recent global warming. Nature 367: 634-636

Tett SFB, Johns TC, Mitchell JFB (1996) Global and Regional Variability in a Coupled AOGCM. Clim Dyn (submitted)

Tibaldi S, Molteni F (1990) On the operational predictability of blocking. Tellus 42A: 343-365

Tokioka T, Noda A, Kitoh A, Nikaidou Y, Nakagawa S, Motoi T, Yukimoto S, Takata K (1995) A transient CO_2 experiment with the MRI CGCM - Quick Report. J Meteorol Soc Japan 74: 817-826

Trenberth KE, Soloman A (1994) The global heat balance: heat transports in the atmosphere and ocean. Clim Dyn 10: 107-134

Warrilow DA, Sangster AB, Slingo A (1986) Modelling of land surface processes and their influence on European climate. Met O 20 Dynamical Climatology Technical Note 38, Meteorological Office, Bracknell, UK.

Washington WM, Meehl GA (1989) Climate sensitivity due to increased CO_2: Experiments with a coupled atmosphere and ocean general circulation model. Clim Dyn 4: 1-38

WCRP (1995) Proceedings of the workshop on Global Coupled General Circulation Models (Scripps Institution of Oceanography, La Jolla, California, USA, 10-12 October 1994), WMO/TD-No. 655, 51 pp

Wood, RA (1996) Timestep sensitivity and accelerated spinup of an ocean GCM with a complex mixing scheme. J Atmos Oceanic Technol (submitted)

White AA, Bromley, RA (1995) Dynamically consistent, quasi-hydrostatic equations for global models with a complete representation of the Coriolis force. Quart J Roy Meteor Soc 121: 399-418

Wigley TML (1995) A successful prediction? Nature 376: 463-464

TABLES

Layer	A (Pa) layer centre	A (Pa) layer boundary	B layer centre	B layer boundary	Hybrid coordinate
		0.005×10^4		0.000	0.0005
19	0.046×10^4		0.000		0.005
		0.100×10^4		0.000	0.010
18	0.148×10^4		0.000		0.015
		0.200×10^4		0.000	0.020
17	0.296×10^4		0.000		0.030
		0.400×10^4		0.000	0.040
16	0.553×10^4		0.002		0.057
		0.718×10^4		0.003	0.075
15	0.886×10^4		0.011		0.100
		1.065×10^4		0.018	0.125
14	1.180×10^4		0.031		0.149
		1.300×10^4		0.045	0.175
13	1.366×10^4		0.063		0.200
		1.434×10^4		0.082	0.225
12	1.458×10^4		0.104		0.250
		1.482×10^4		0.127	0.275
11	1.469×10^4		0.153		0.300
		1.456×10^4		0.179	0.325
10	1.401×10^4		0.215		0.355
		1.345×10^4		0.251	0.385
9	1.232×10^4		0.299		0.422
		1.118×10^4		0.348	0.460
8	0.947×10^4		0.410		0.505
		0.773×10^4		0.473	0.550
7	0.581×10^4		0.541		0.599
		0.385×10^4		0.611	0.650
6	0.241×10^4		0.675		0.699
		0.094×10^4		0.741	0.750
5	0.047×10^4		0.788		0.793
		0.000×10^4		0.835	0.835
4	0.000×10^4		0.870		0.870
		0.000×10^4		0.905	0.905
3	0.000×10^4		0.930		0.930
		0.000×10^4		0.956	0.956
2	0.000×10^4		0.975		0.975
		0.000×10^4		0.994	0.994
1	0.000×10^4		0.997		0.997
		0.000×10^4		1.000	1.000

Table 1: Distribution of 19 hybrid vertical layers and layer boundaries in atmosphere model.

Note: The hybrid coordinate is defined as $(A/10^5 \text{ Pa}) + B$.

Level	Depth (m)	Thickness (m)	Vertical diffusivity (10^{-5} m^2/s)
1	5.0	10.0	-
2	15.0	10.0	1.03
3	25.0	10.0	1.06
4	35.1	10.2	1.08
5	47.9	15.3	1.11
6	67.0	23.0	1.16
7	95.8	34.5	1.22
8	138.9	51.8	1.32
9	203.7	77.8	1.46
10	301.0	116.8	1.68
11	447.1	175.3	2.01
12	666.3	263.2	2.50
13	995.6	395.3	3.23
14	1501.0	615.0	4.34
15	2116.0	615.0	6.06
16	2731.0	615.0	7.79
17	3347.0	615.0	9.51
18	3962.0	615.0	11.23
19	4577.0	616.0	12.95
20	5193.0	616.0	14.68

Table 2: Vertical levels and background tracer vertical diffusivity between level and level above in the ocean model.

Aspect	UKTR	HADCM2
Resolution (atmosphere)	96x72 L11 (A-grid, sigma coord)	96x73 L19 (B-grid, hybrid)
Resolution (ocean)	Congruent, 17 depth levels	Congruent, 20 depth levels
Timestep (atmosphere)	10 minutes	30 minutes
Timestep (ocean)	20 minutes	60 minutes
Coupling cycle	5 days	1 day
Atmospheric dynamics	Centred explicit, leapfrog	Split-explicit, Heun
Solar radiation scheme	Single spectral band	Multiple spectral bands
Atmospheric convection	Ignores downdraughts	Includes downdraughts
Boundary layer fluxes	No account of ocean currents	Ocean currents used
Surface hydrology	Assumes homogeneous rainfall	Uses gridbox distribution
River runoff	Not included	Included
Ocean diffusivity	Constant with latitude	1+cos(latitude) function
Vertical tracer mixing	Uniform with depth	Increasing with depth
Mediterranean mixing	Not included	Included
Sea ice dynamics	Not included	Included
Leads fluxes at ice pts	Applied solely to ice budget	Split between ice/ocean
Fields flux adjusted	Ocean SST,SSS and sea ice mass	Ocean SST and SSS only
Reference SST's	Levitus, modified at seaice	Levitus, unmodified
Reference SSS's	Levitus, unmodified	Levitus, modified
Averaging of adjustments	5 day means, 10 year average	5-day means, 25 year average

Table 3: Summary of the main differences between UKTR and HADCM2.

Month	Adjusted Salinity at southern row (75 or 77.5 S) (psu)	Northernmost latitude (row number) for interpolation
May	34.5	72.5 S (row 7)
Jun	34.7	70.0 S (row 8)
Jul	34.9	67.5 S (row 9)
Aug	34.9	67.5 S (row 9)
Sep	34.8	70.0 S (row 8)
Oct	34.6	72.5 S (row 7)

Table 4: Adjustments to Levitus (1982) reference sea surface salinities in the ocean model. Note: The southern row is defined as row 6 (75 S) in the Ross Sea sector, row 5 (77.5 S) elsewhere. Reference salinities are linearly interpolated from the adjusted value at the southern row to the standard Levitus (1982) value at the northern latitude listed. No adjustments are made in other months.

River Name	Outflow Point	Model Flow ($10^3 m^3/s$)	Observed Flow ($10^3 m^3/s$)	Precip Error L&W (%)	Precip Error GPCC (%)
Amazona	48.75W, 0 N	190.5	149.0	9.7	27.4
Ganges	86.25E, 20 N	58.5	11.3	-0.6	16.5
Zaire	7.5E, 0 N	55.7	40.0	53.0	98.0
Parana	52.5 W, 35 S	45.0	16.0	29.2	36.3
Indus	67.5 E, 22.5N	31.2	3.9	56.4	74.6
Chang Jiang	120 E, 35 N	23.9	25.0	69.2	69.0
Unnamed	135 W, 55 N	19.7	—	48.9	54.5
Yenisei	78.75E, 72.5N	19.2	17.7	76.8	73.2
Ramu	150 E, 7.5S	18.6	—	70.5	69.4
Niger	3.75E, 5 N	18.3	1.5	-39.2	-3.7
Orinoco	60 W, 10 N	18.1	31.0	-90.2	-24.1
Ob	67.5 E, 72.5N	18.0	12.5	-29.6	39.9
Nile	26.25E, 32.5N	17.6	2.8	39.7	74.5
Unnamed	142.5E, 2.5S	17.5	—	65.4	73.6
Columbia	127.5W, 47.5N	17.0	5.5	54.0	99.3

Table 5: Comparison of modelled and observed river flows for 15 major rivers. Note: Precipitation errors in the final two columns are the integrated model minus observed totals, expressed as a percentage of the model flow.

Model	Mean Heat flux adjustment (W/m^2)	RMS Heat flux adjustment (W/m^2)	Mean Water flux adjustment (mm/day)	RMS Water flux adjustment (mm/day)
UKTR	4.92	34.18	0.40	4.00
HADCM2	0.43	47.57	0.13	5.74

Table 6: Annual area weighted mean and root-mean-squared flux adjustments over the ocean surface for UKTR and HADCM2.

Layer Depth (m)	Temperature (Model) (Deg C)	Temperature (Levitus) (Deg C)	Temperature (Error) (Deg C)	Salinity (Model) (psu)	Salinity (Levitus) (psu)	Salinity (Error) (psu)
5	17.988	17.986	0.003	34.573	34.638	-0.066
15	17.981	17.870	0.112	34.574	34.690	-0.116
25	17.885	17.678	0.207	34.605	34.746	-0.140
35	17.693	17.382	0.311	34.644	34.795	-0.152
48	17.330	16.935	0.394	34.694	34.851	-0.157
67	16.870	16.361	0.509	34.865	34.956	-0.091
96	15.971	15.206	0.765	34.949	35.013	-0.064
139	14.650	13.605	1.046	35.015	35.031	-0.016
204	12.867	11.719	1.148	34.989	34.983	0.006
301	11.041	9.827	1.213	34.876	34.869	0.007
447	9.380	7.878	1.502	34.760	34.729	0.031
666	7.661	5.886	1.775	34.649	34.619	0.030
996	5.980	4.136	1.844	34.573	34.609	-0.036
1501	4.289	2.821	1.468	34.576	34.681	-0.105
2116	3.230	2.062	1.168	34.676	34.726	-0.050
2731	2.399	1.628	0.771	34.729	34.737	-0.008
3347	1.585	1.323	0.263	34.737	34.737	0.001
3962	0.978	1.062	-0.083	34.740	34.732	0.008
4577	0.785	0.902	-0.117	34.740	34.723	0.017
5193	0.913	1.020	-0.107	34.734	34.721	0.013

Table 7: Average ocean temperature and salinity in each model layer averaged over 130 years compared with the Levitus (1982) climatology.

Trends	GHG	SUL	CTL (Mean)	CTL (SD)	Observed 1978-87	Observed 1987-94
Arctic	-0.046	+0.003	-0.001	0.017	-0.030	-0.049
Antarctic	+0.004	+0.033	+0.005	0.052	-0.027	-0.003

Table 8: Sea ice area trends (millions of square km per year) simulated in GHG and SUL for 1978 to 1994, with statistics for such trends from the control run (CTL), and observed trends from satellite data (Johannessen et al. 1995).

FIGURE CAPTIONS

Figure 1: Comparison between (a) the interdecadal standard deviation of ice thickness in the first 400 years of the coupled control run; and (b) the difference between the mean ice thickness from years 160 to 170 of an ocean-only spinup run and the last 10 years of the coupled spinup, plotted for the Antarctic. Contours at -0.1, -0.05, 0.05, 0.1, 0.2, 0.5, 1, 2, 3 and 4 m; dark shading below -0.1 m, light shading above 0.2 m.

Figure 2: Latitude-depth cross-sections of interdecadal standard deviation of average oceanic temperature in the control run compared with the initial readjustment from the end of the spinup to the start of the control run. Contours every 0.05 K, shaded below -0.1 and above +0.1 K. (a) Interdecadal standard deviation from years 200 to 400 of the control; (b) First decade of the control minus last decade of the spinup.

Figure 3: Meridional overturning streamfunction averaged over the last decade of two 50 year ocean-only spinup runs with restoration to (a) un-adjusted Levitus (1982) climatological surface salinities, and (b) surface salinities adjusted near the Antarctic coast in austral winter as described in the text. Contour 4 Sv, positive values shaded.

Figure 4: Time-depth cross-sections of global average annual oceanic temperature and salinity relative to the Levitus (1982) climatology at each level throughout the spinup phase and for the first 400 years of the control run. (a) Oceanic temperature difference (K); (b) Oceanic salinity difference (psu). During the spinup phase, restoring-type boundary conditions were used for years 1 to 65, 156 to 210, 391 to 440 and 456 to 510 (marked with a thick bar on the time axis). Flux adjustment type boundary conditions were used for years 66 to 155, 211 to 390 and 441 to 455. The flux adjustment terms used in the control run (years 511 onwards, to the right of the vertical line) were calibrated over the final 25 years (486 to 510) of the spinup phase.

Figure 5: Anomalies, with respect to the average over the 130 years from 1860 to 1990, of zonally averaged decadal surface air temperature (land and sea combined) over the first 400 years of the model control run. Contour 0.1K, negative values shaded.

Figure 6: Timeseries of decadal average hemispheric sea ice areal coverage and volume over the first 400 years of the model control run.

Figure 7: Latitude versus month, zonal average radiation budget (W/m^2), HADCM2 difference from ERBE climatology (Harrison et al. 1990; averaged from February 1985 to January 1989). (a) Net downward shortwave; contours every 10 W/m^2, negative values shaded. (b) Net outgoing longwave; contours every 5 W/m^2, negative values shaded.

Figure 8: Zonal average (a) shortwave and (b) longwave cloud forcing difference between January and July (W/m^2) in HADCM2, compared with ERBE (period as in Fig. 7) and UKTR. The shortwave cloud forcing is normalised by the incoming solar radiation to eliminate the strong seasonal cycle.

Figure 9: Annual average zonally integrated northward heat transport (peta-Watts) by the climate system estimated from ERBE fluxes (period as in Fig. 7) and simulated by the model, and by the ocean (climatological estimates redrawn from Trenberth and Soloman 1994, compared with simulated values). Actual ocean transports and those implied by net fluxes from the atmosphere (excluding flux adjustments) are shown separately for the model. Modelled and observed fluxes at the top of the atmosphere were independently adjusted in this calculation to give an exact global energy balance.

Figure 10: Mean sea level pressure simulated by the model for DJF and JJA seasons (a and b), compared with mean UKMO operational model analyses between May 1983 and September 1995 (c and d). Contour interval 5 hPa.

Figure 11: Height-latitude cross-section of atmospheric temperature errors compared with mean UKMO operational model analyses over the same period as in Fig. 10. Contours every 1K between -2 and +2, then every 2K. Negative values shaded. (a) DJF (model minus analyses); (b) JJA (model minus analyses).

Figure 12: Height-latitude cross-section of atmospheric zonal wind errors compared with mean UKMO operational model analyses over the same period as in Fig. 10. Contours every 2 m/s. Negative values shaded. (a) DJF (model minus analyses); (b) JJA (model minus analyses).

Figure 13: Zonal average atmospheric meridional mass streamfunction in the model for (a) DJF, and (b) JJA. Contours every 20×10^9 kg/s, negative values shaded.

Figure 14: 2 to 6 day band pass filtered (Blackmon 1976) standard deviation of daily 500mb height for DJF. Shading above 6 dam. Ten seasons are included in the analysis; a ten year period starting 220 years into the HADCM2 control run, and June 1983 to February 1993 from UKMO operational model analyses interpolated to climate model resolution.

Figure 15: As Fig. 14, but for JJA.

Figure 16: DJF storm tracks, determined by an objective low-counting technique from (a) the HADCM2 control run and (b) UKMO analyses for the same periods as in Fig. 14, and (c) years 115-125 in the UKTR control run, for the Northern Hemisphere north of 30 degrees N. Units are number of lows per million square km per season. Contours every 2; shaded above 4.

Figure 17: DJF blocking frequency as a function of longitude from the UKTR and HADCM2 control runs, and UKMO analyses. A blocking index based on latitudinal gradients of 500mb height north of 40N is computed at each longitude for each day, over the same periods as for Fig. 16. The ordinate plotted is the percentage of days for which the blocking index is greater than zero.

Figure 18: Zonally averaged total precipitation (mm/day) in the model compared with the Jaeger (1976) and Legates and Willmott (1990) climatologies for (a) DJF and (b) JJA.

Figure 19: Maps of seasonal total precipitation at the surface (mm/day) in the model. Contours at 1,2,5,10 and 20 mm/day, shaded above 5 mm/day. (a) DJF; (b) JJA.

Figure 20: Maps of seasonal soil moisture content (mm) in the model. Contours at 0.1,1,10,50,100 and 200 mm, light shading below 1 mm and dark shading above 100 mm. (a) DJF; (b) JJA.

Figure 21: Zonally averaged seasonal heat flux (W/m^2) from atmosphere to ocean in the model, excluding flux adjustment, (dashed line) compared with the climatology of Esbensen and Kushnir (1981) (solid line), and the zonal average heat flux adjustment (dot-dashed line) for (a) DJF and (b) JJA.

Figure 22: Zonally averaged seasonal P-E flux (mm/day) from atmosphere to ocean in the model, excluding flux adjustment, (dashed line) compared with observations based on the precipitation climatology of Jaeger (1976) and evaporation climatology of Esbensen and Kushnir (1981) (solid line), and the zonal average water flux adjustment (dot-dashed line) for (a) DJF and (b) JJA.

Figure 23: Zonally averaged westerly wind stress (N/m^2) at the atmosphere-ocean surface in the model (dashed line) compared with the climatology of Hellerman and Rosenstein (1983) (solid line) for (a) DJF and (b) JJA.

Figure 24: Annual average flux adjustments resulting from the final calibration leg of the spinup phase of the experiment (negative values shaded). (a) Heat flux adjustment; contours at 0 and +/- 50,100,200,300 W/m^2. (b) Water flux adjustment; contours at 0 and +/- 5,10,20,30 mm/day.

Figure 25: Zonal average global oceanic potential temperature in the model averaged over 130 years, and difference from the climatology of Levitus (1982). (a) Model; contour 2 deg C up to 8, then 4 deg C, shaded below 0 deg C. (b) Difference from Levitus; contour 0.5 deg C, negative values shaded.

Figure 26: As Fig. 25, but for salinity. (a) Model; contour 0.25 psu down to 34.0, then 1 psu, shaded above 35.0 psu. (b) Difference from Levitus; contour 0.1 psu between +0.5 and -0.5, then every 0.5 psu, negative values shaded.

Figure 27: Zonally integrated oceanic meridional mass streamfunction in the model, averaged over 130 years. Contour 4 Sv, positive values shaded. (a) Globally averaged. (b) Averaged over the Atlantic basin north of the tip of South Africa.

Figure 28: Seasonal cycle of sea ice areal coverage in the NH and SH compared with the GISST2.2 1961-1990 climatology (Rayner et al. 1995).

Figure 29: Average September sea ice areal coverage in the model and the GISST2.2 1961-1990 climatology (Rayner et al. 1995). Contours at 0.15, 0.50 and 0.85 fractional cover.

Figure 30: As Fig. 29, but for March.

Figure 31: Effective global average forcing (W/m^2) as a function of model simulated year in the GHG run (dotted curve) and SUL run (solid curve) from 1860 to 1990. The forcing in SUL is the net forcing due to effective CO_2 as in the GHG run plus a negative forcing from sulphate aerosols (dashed curve). Sulphate forcing is diagnosed explicitly in the model runs, whereas CO_2 forcing is scaled from a calibrated diagnostic of forcing at the tropopause due to instantaneous doubling of CO_2 computed during a 5 year period from the control run, adjusted to account for a reduction in downward longwave flux from stratospheric cooling. The globally averaged instantaneous net flux change is 4.04 W/m^2, reduced to 3.47 W/m^2 by the stratospheric cooling adjustment. Scaling of CO_2 forcing in time is according to the formula $F(t) = F^*\log[C(t)/C_0]/\log 2$ where F is the forcing due to instantaneous doubling, C(t) is the CO_2 concentration at time t and C_0 is the CO_2 concentration in the control run.

Figure 32: Annual average surface air temperature change between the beginning of the 20th century (40 year average centred on 1900) and the present day (20 year average from 1970 to 1990). Contour 0.5K, negative values shaded. (a) Simulated in GHG run; (b) Simulated in SUL run; (c) Observed, based on blended UEA land temperature and UKMO MOHSST historical sea surface temperature dataset (Parker et al. 1994b).

Figure 33: Evolution of decadal surface air temperature anomaly correlations between observed temperatures (Parker et al. 1994b) and corresponding decades of GHG run (dashed line) and SUL run (solid line). A 10% significance level is also shown for each run, computed by fitting a normal distribution to the sampling distribution of correlations for each decade of each run, where the sampling distribution is obtained from correlations between the decade concerned and each of the first 40 decades of the control run after applying the observed data mask for the decade concerned.

Figure 34: Zonally averaged surface air temperature anomalies relative to 1950 to 1980 for (a) GHG; (b) SUL; and (c) observed, expressed as decadal running averages over the modelled and observed period 1890 to 1993. Observed values are as in Parker et al. (1994b; Fig. 4). Model anomalies are computed in a similar manner to the observed but using all data. Contours every 0.1K; positive values shaded.

Figure 35: Anomalies of monthly sea ice area from October 1978 to December 1994 in GHG (dashed) and SUL (solid). Anomalies are relative to the corresponding monthly average over the period. Best fit linear regression lines are also shown. (a) Arctic totals for 60-90 degrees N; (b) Antarctic totals for 45-90 degrees S.

Figure 36: 1963 to 1988 best fit linear trends in zonal average atmospheric temperature plotted against pressure for (a) GHG; (b) SUL and (c) observed (Oort 1983; Oort and Liu 1993). Contours every 0.01 between -0.04 and +0.04, otherwise every 0.02 K/yr.

(a) Coupled control run:
Decadal standard deviation (m)

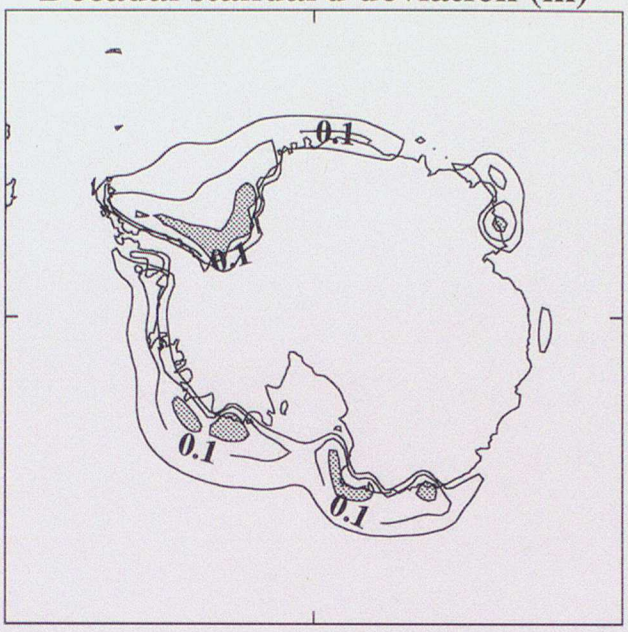

(b) Ocean-only minus coupled spinup:
Ice thickness difference (m)

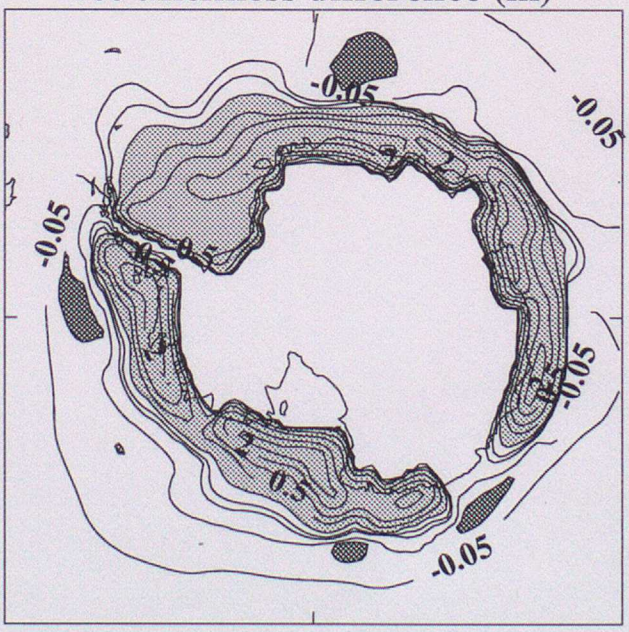

Figure 1

(a) Interdecadal standard deviation over years 200 to 400 of Control (K)

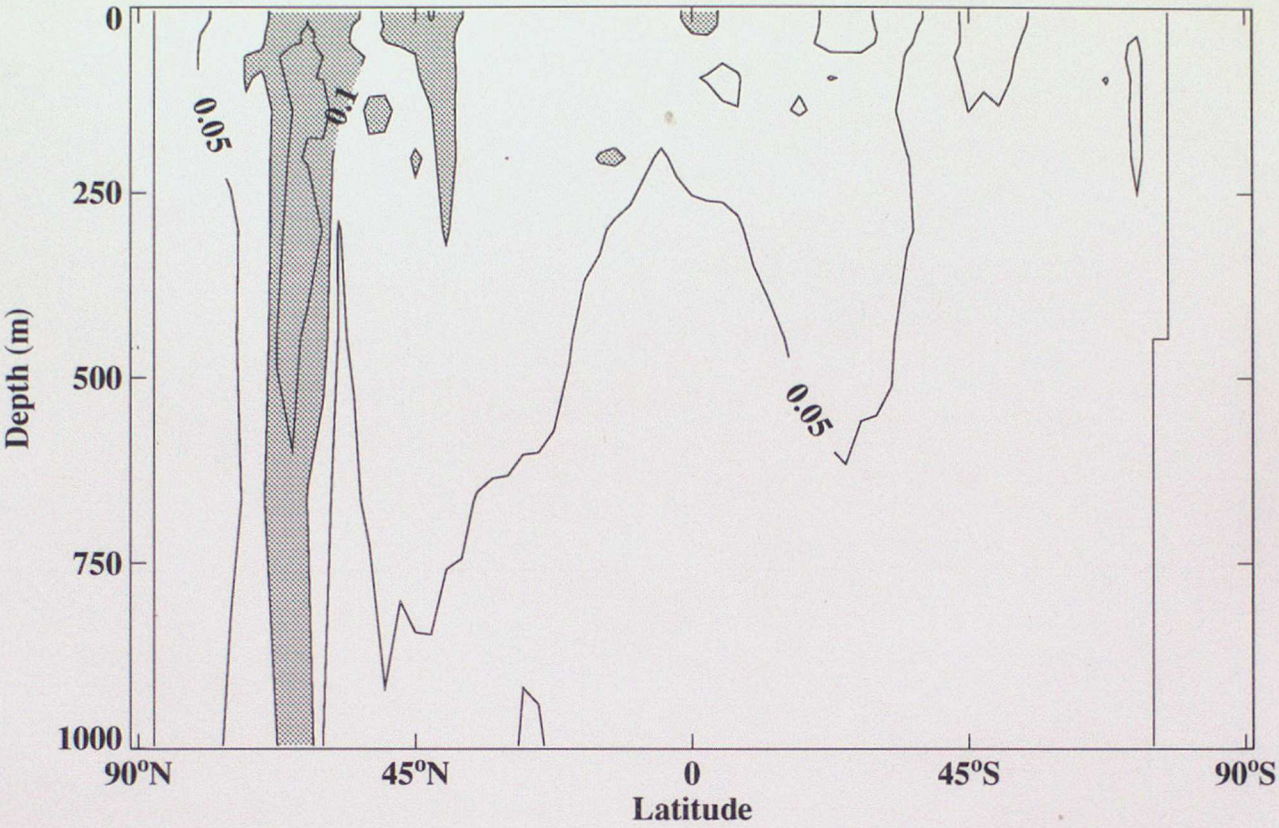

(b) First decade of Control minus last decade of Spinup (K)

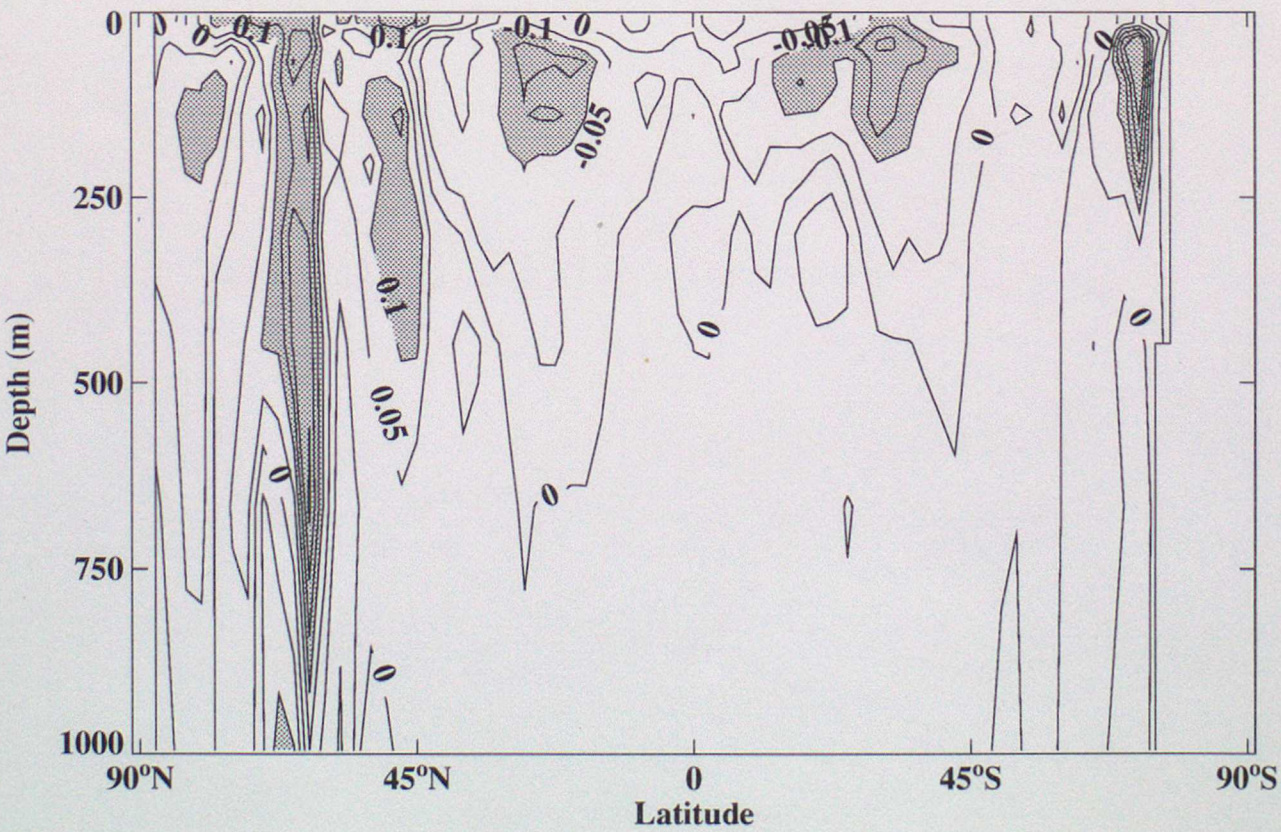

Figure 2

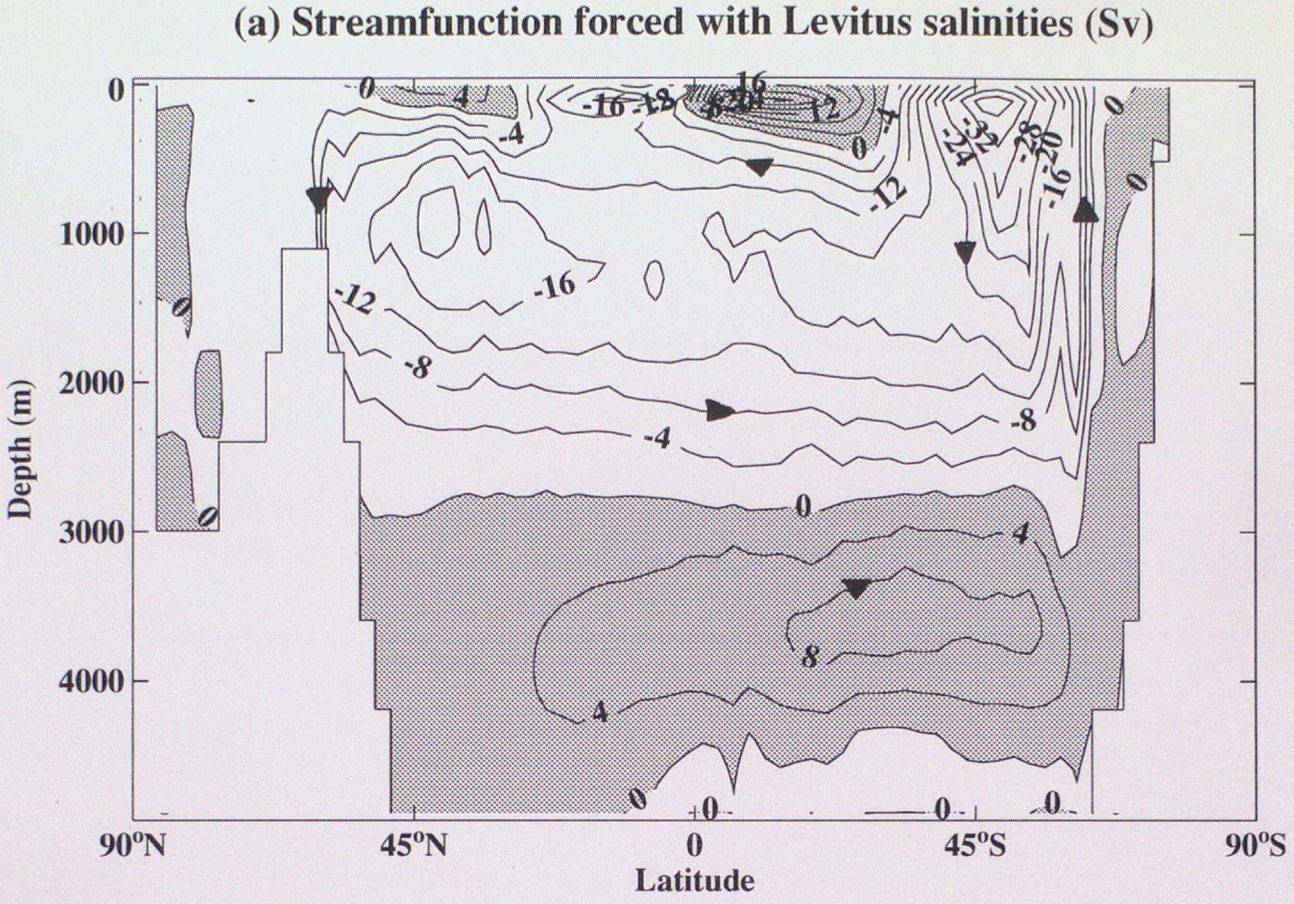
(a) Streamfunction forced with Levitus salinities (Sv)
Depth (m)
0
1000
2000
3000
4000
90°N
45°N
0
45°S
90°S
Latitude

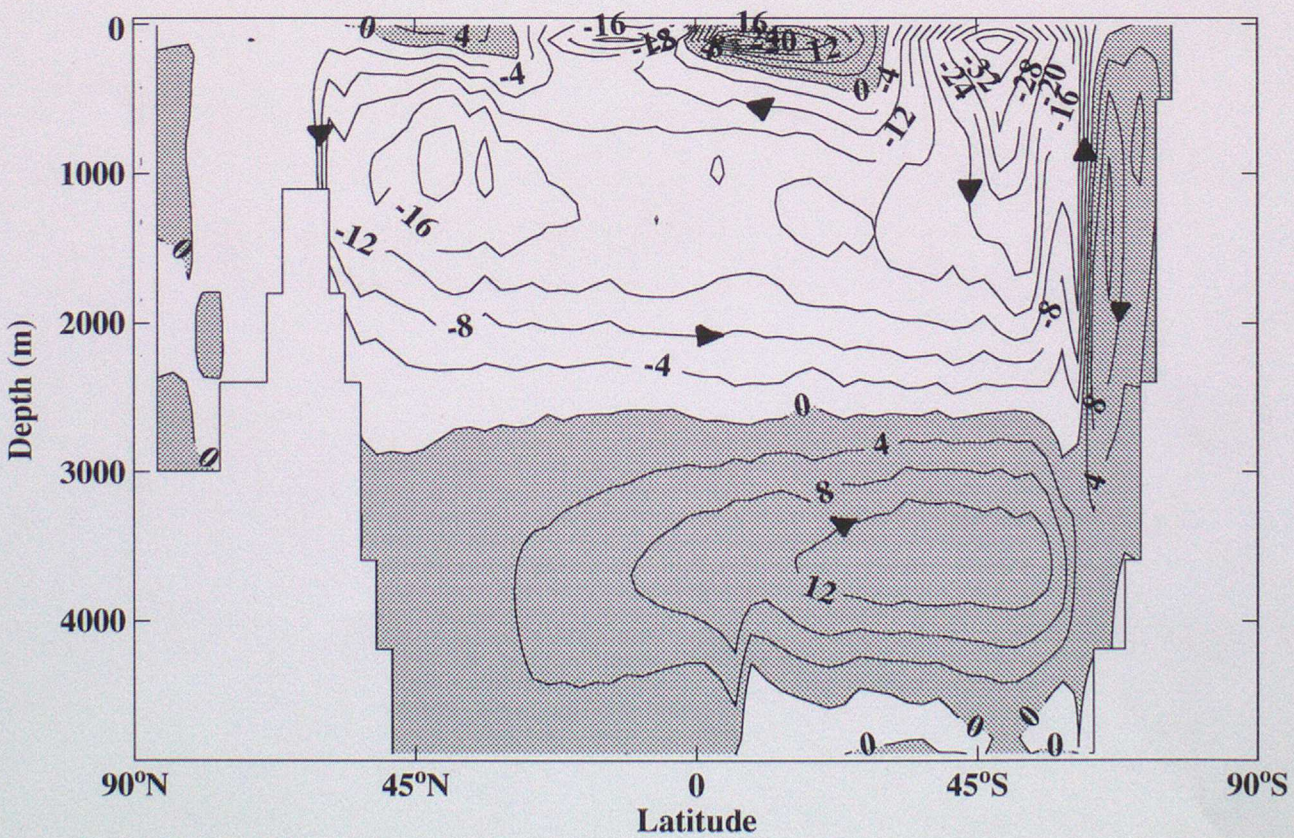
(b) Streamfunction forced with adjusted salinities (Sv)
Depth (m)
0
1000
2000
3000
4000
90°N
45°N
0
45°S
90°S
Latitude

Figure 3

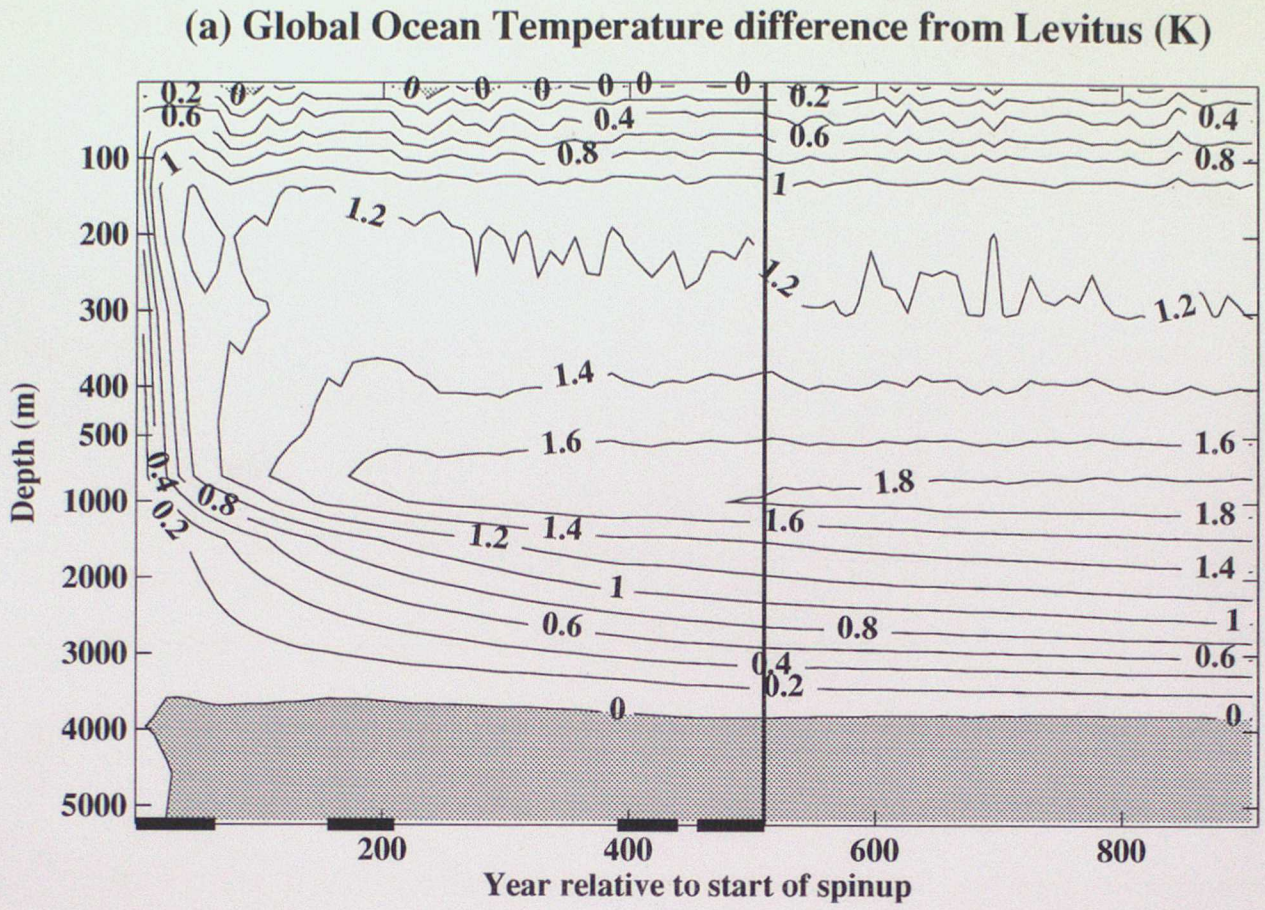
(a) Global Ocean Temperature difference from Levitus (K)
Depth (m)
100
200
300
400
500
1000
2000
3000
4000
5000
200
400
600
800
Year relative to start of spinup

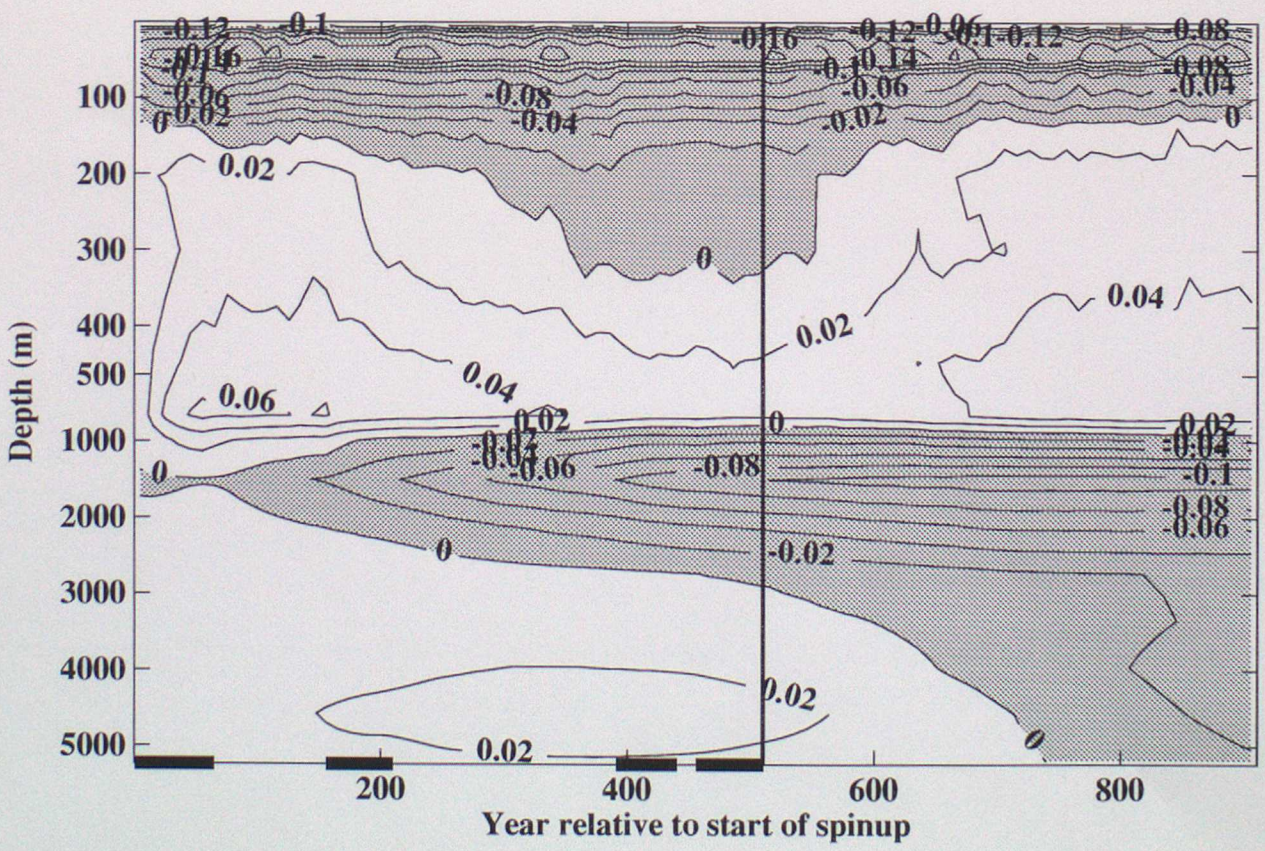
(b) Global Ocean Salinity difference from Levitus (psu)
Depth (m)
100
200
300
400
500
1000
2000
3000
4000
5000
200
400
600
800
Year relative to start of spinup

Figure 4

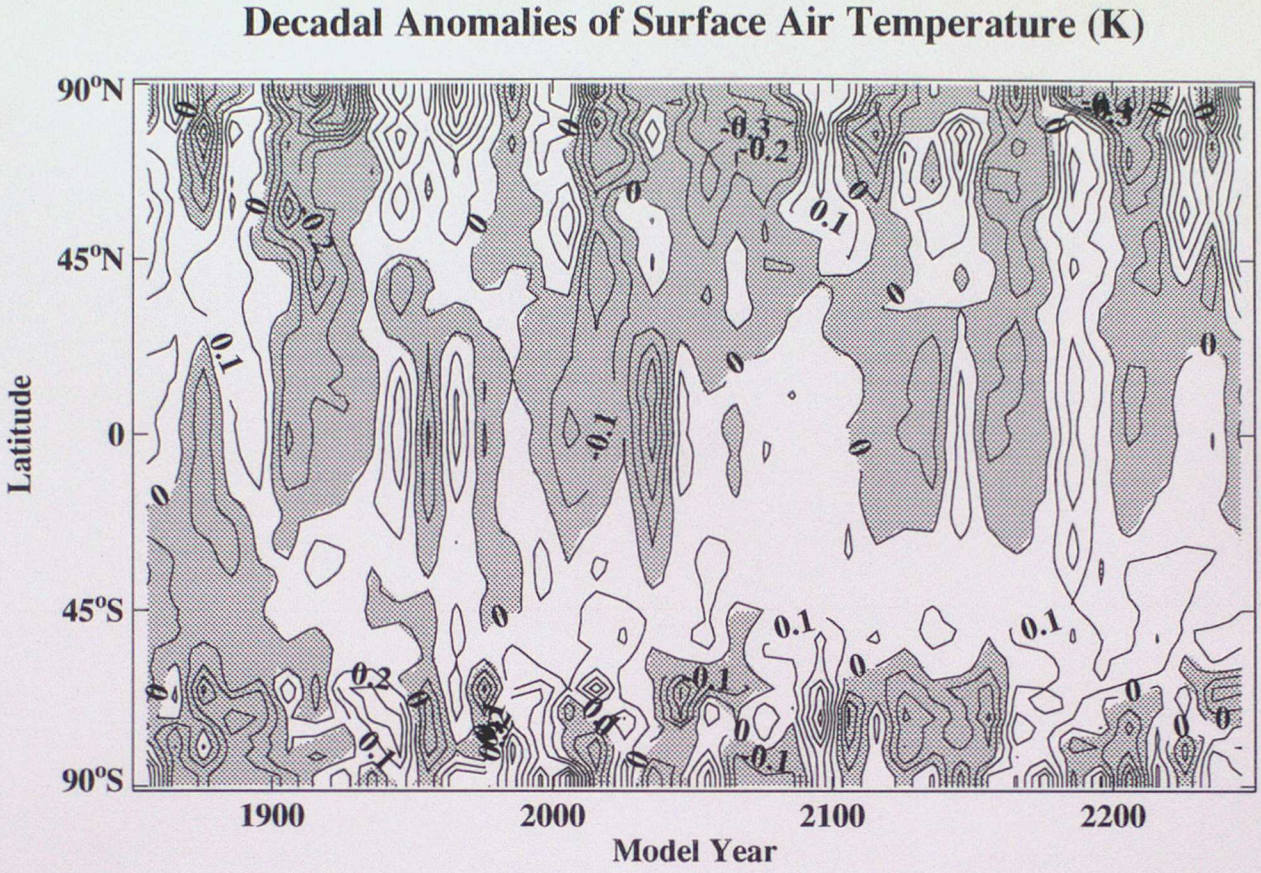
Decadal Anomalies of Surface Air Temperature (K)
90°N
45°N
0
45°S
90°S
Latitude
1900
2000
2100
2200
Model Year

Figure 5

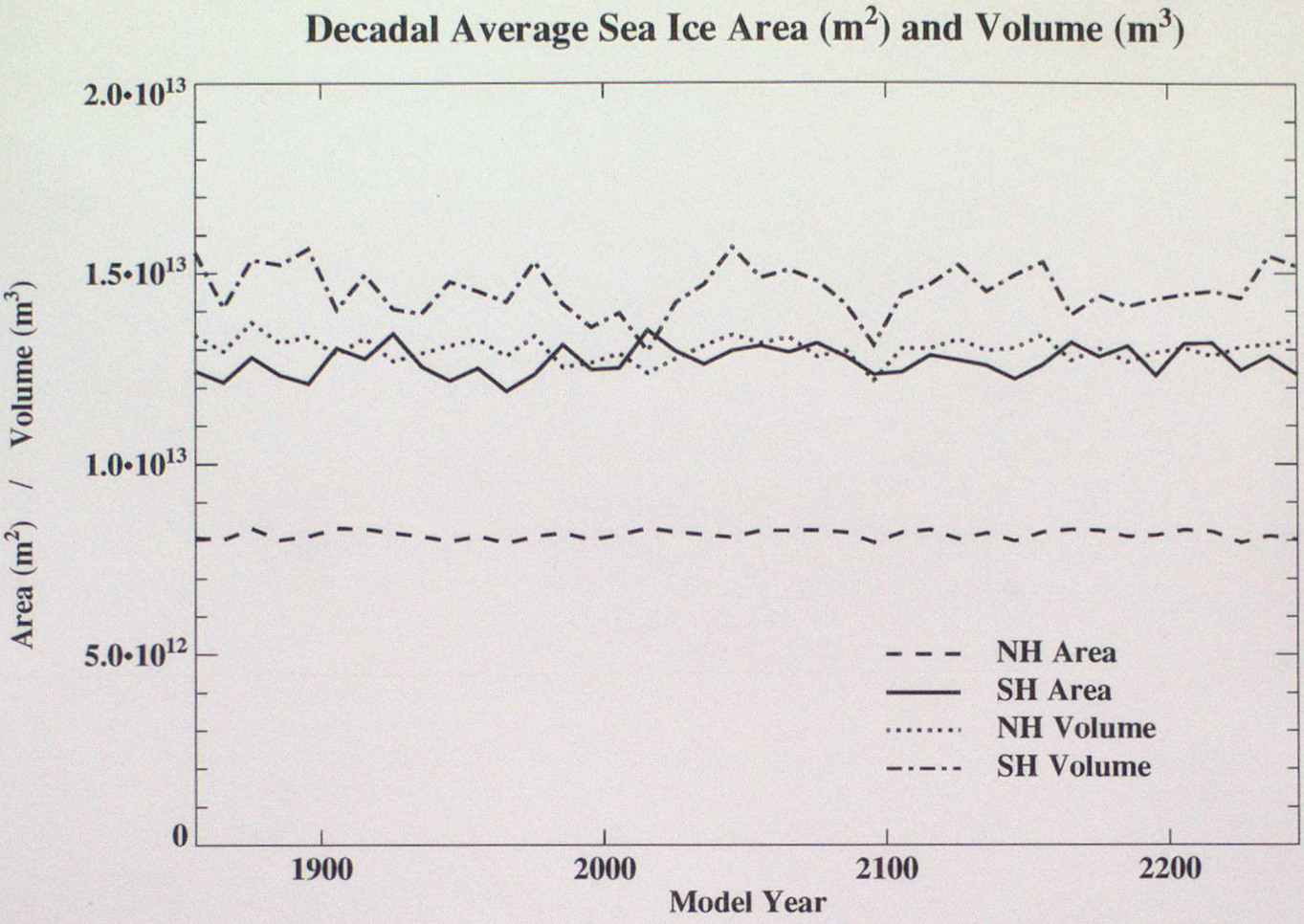
Decadal Average Sea Ice Area (m^2) and Volume (m^3)
$2.0 \cdot 10^{13}$
$1.5 \cdot 10^{13}$
$1.0 \cdot 10^{13}$
$5.0 \cdot 10^{12}$
0
Area (m^2) / Volume (m^3)
1900
2000
2100
2200
Model Year
NH Area
SH Area
NH Volume
SH Volume

Figure 6

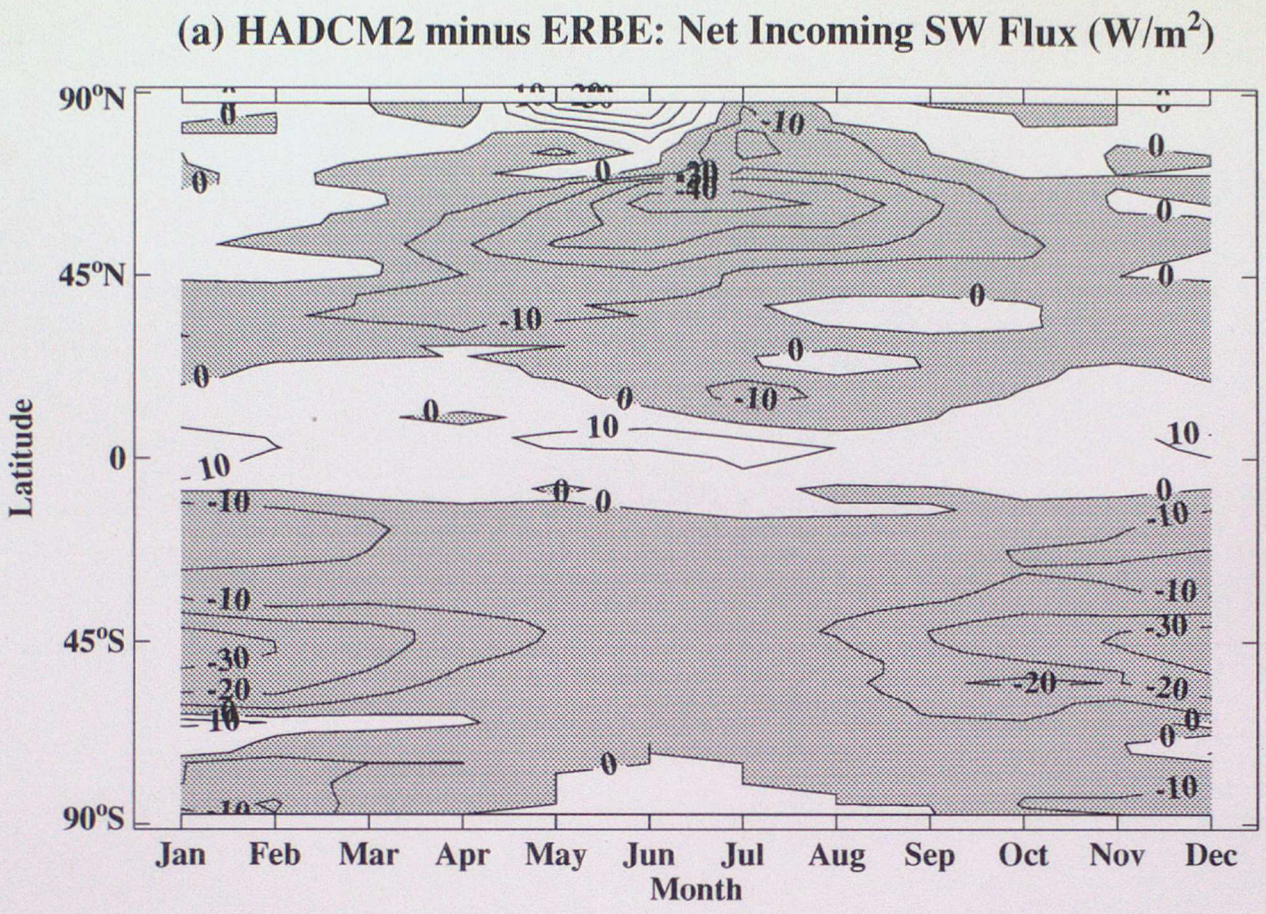
(a) HADCM2 minus ERBE: Net Incoming SW Flux (W/m^2)
90°N
45°N
0
45°S
90°S
Latitude
Jan
Feb
Mar
Apr
May
Jun
Jul
Aug
Sep
Oct
Nov
Dec
Month

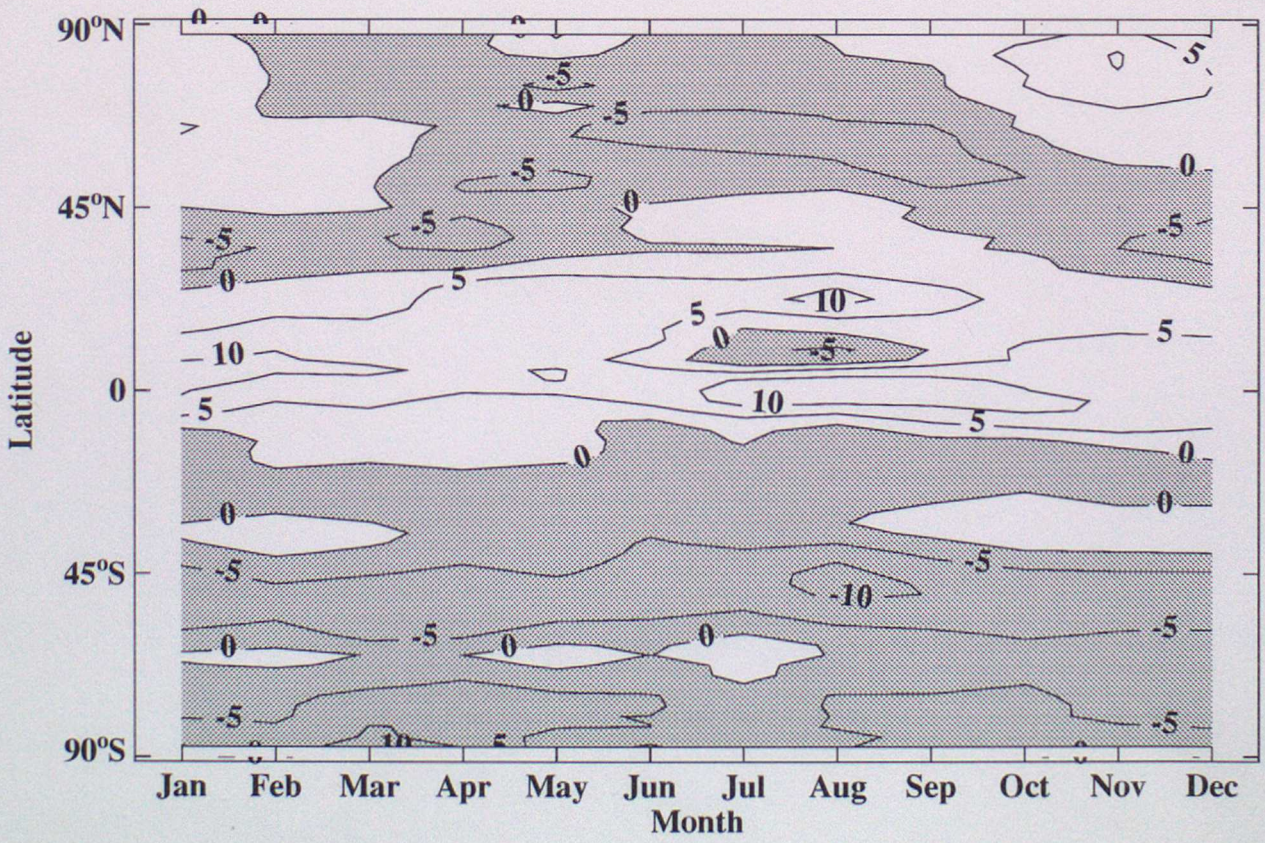
(b) HADCM2 minus ERBE: Net Outgoing LW Flux (W/m^2)
90°N
45°N
0
45°S
90°S
Latitude
Jan
Feb
Mar
Apr
May
Jun
Jul
Aug
Sep
Oct
Nov
Dec
Month

Figure 7

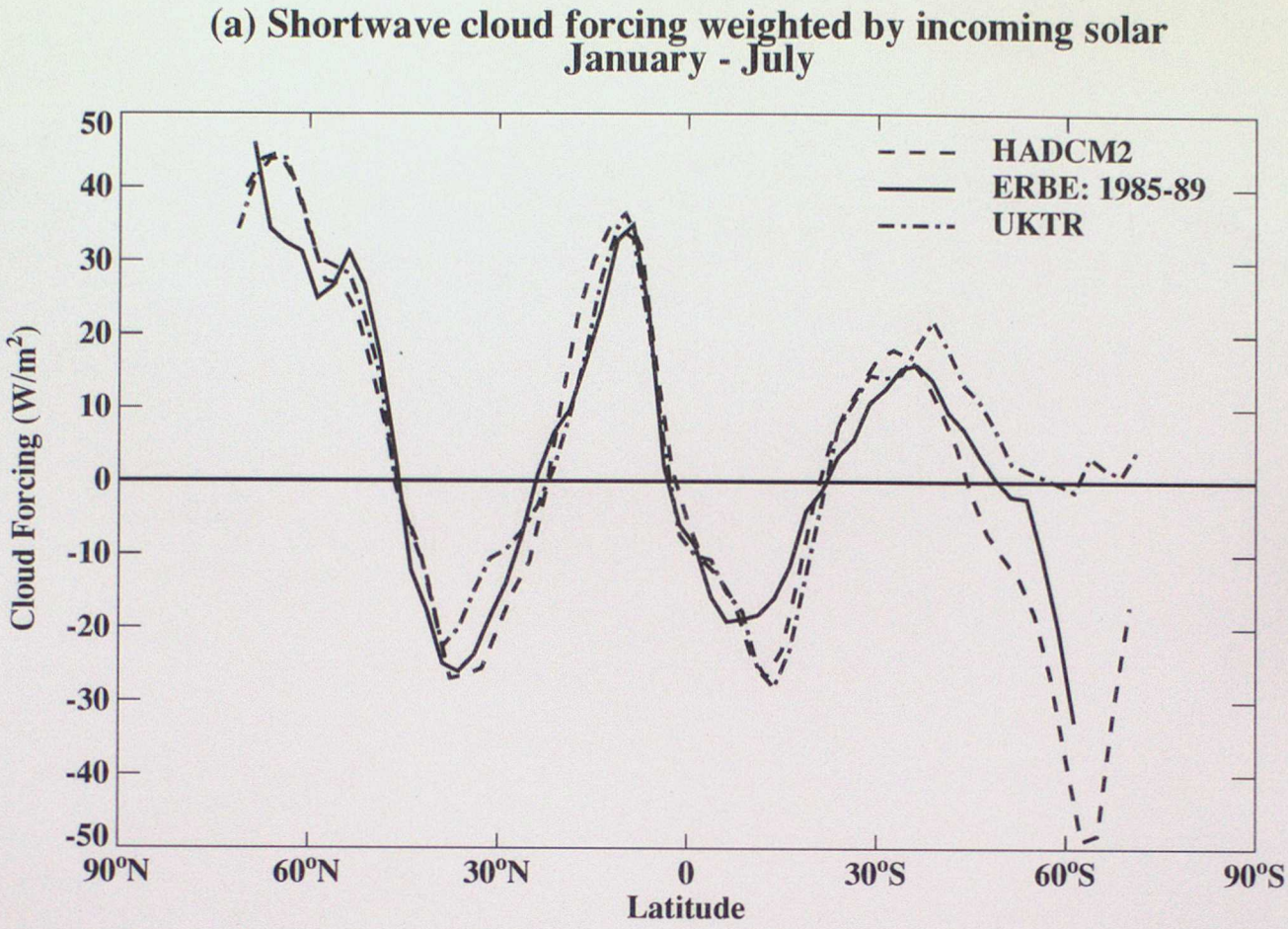
(a) Shortwave cloud forcing weighted by incoming solar
January - July
HADCM2
ERBE: 1985-89
UKTR
Cloud Forcing (W/m²)
50
40
30
20
10
0
-10
-20
-30
-40
-50
90°N
60°N
30°N
0
30°S
60°S
90°S
Latitude

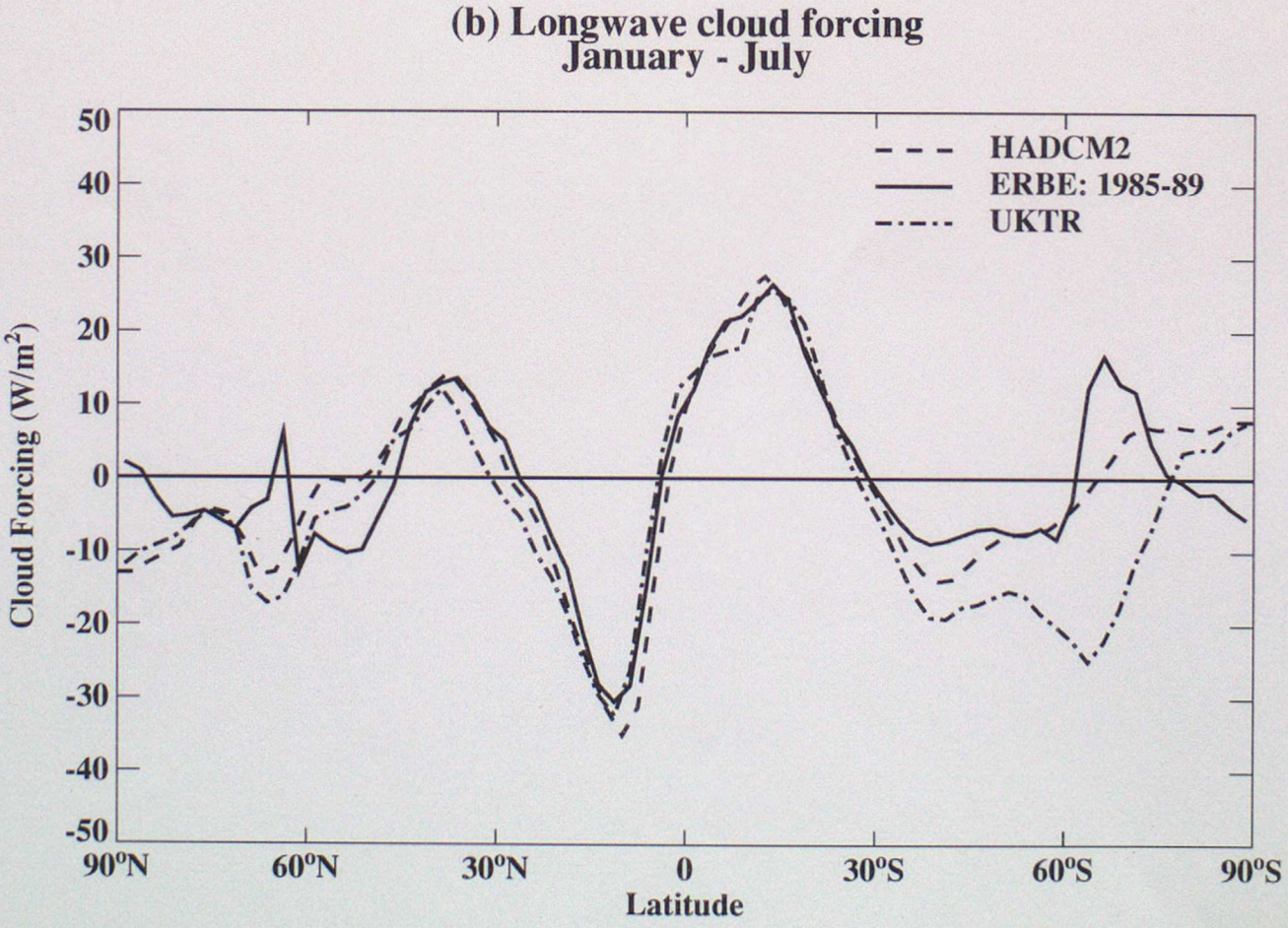
(b) Longwave cloud forcing
January - July
HADCM2
ERBE: 1985-89
UKTR
Cloud Forcing (W/m²)
50
40
30
20
10
0
-10
-20
-30
-40
-50
90°N
60°N
30°N
0
30°S
60°S
90°S
Latitude

Figure 8

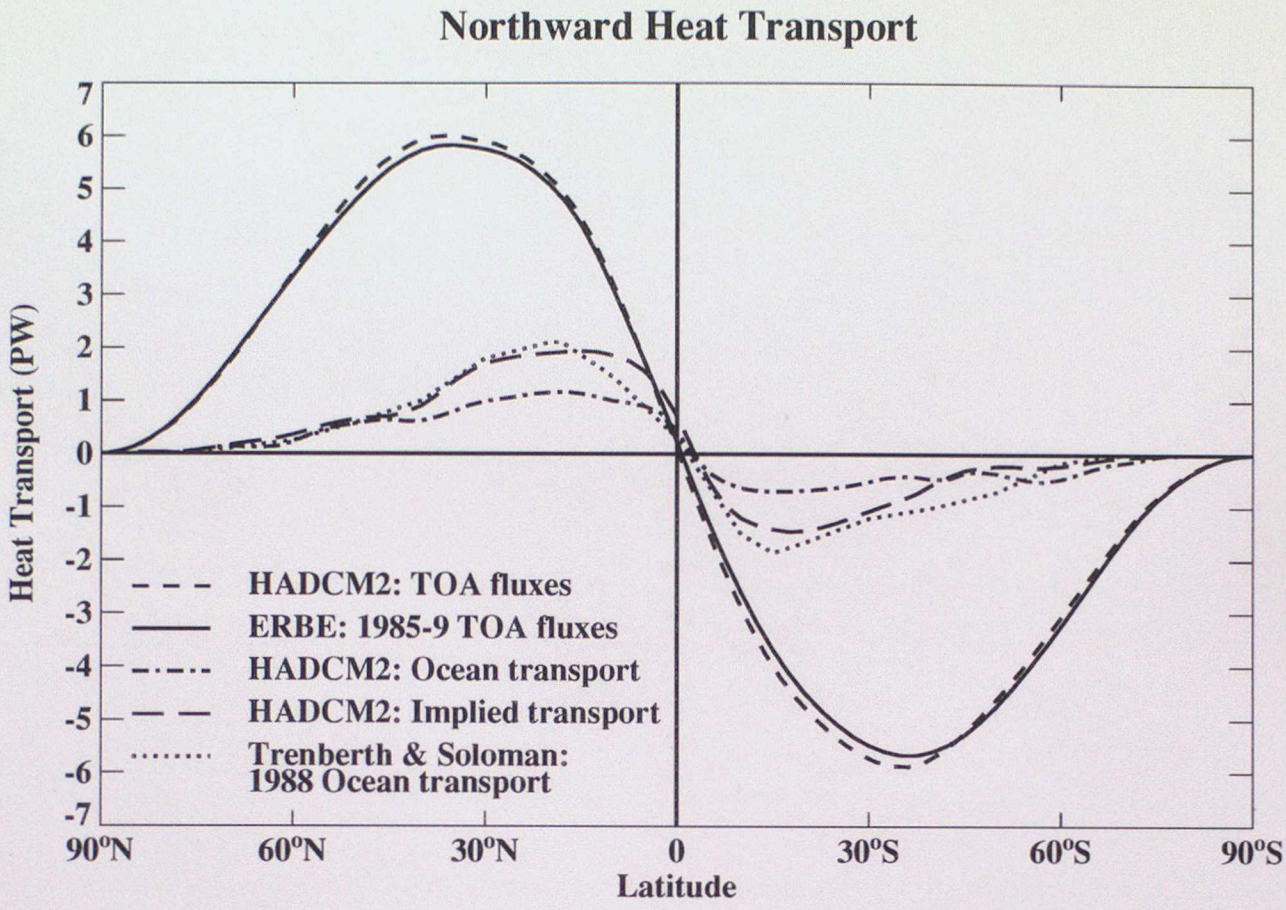
Northward Heat Transport
Heat Transport (PW)
7
6
5
4
3
2
1
0
-1
-2
-3
-4
-5
-6
-7
HADCM2: TOA fluxes
ERBE: 1985-9 TOA fluxes
HADCM2: Ocean transport
HADCM2: Implied transport
Trenberth & Soloman:
1988 Ocean transport
90°N
60°N
30°N
0
30°S
60°S
90°S
Latitude

Figure 9

Figure 10

(a) HADCM2: DJF Mean Sea Level Pressure (hPa)

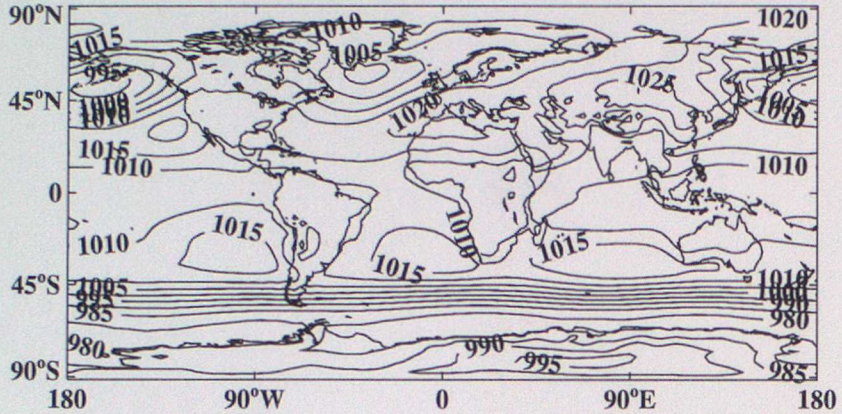

(b) HADCM2: JJA Mean Sea Level Pressure (hPa)

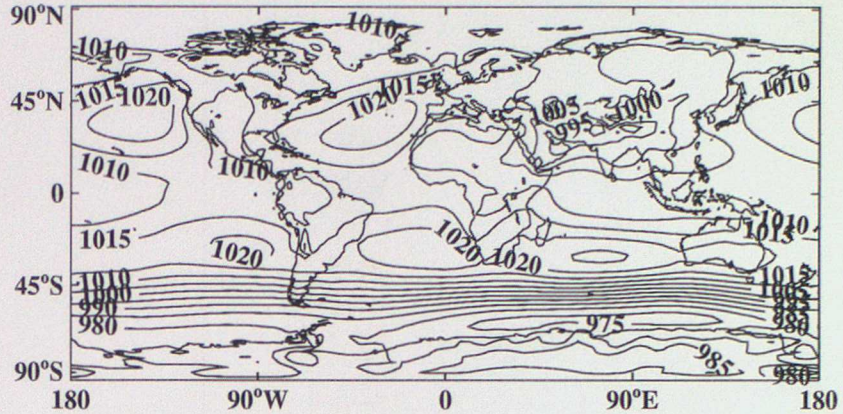

(c) ANALYSIS: DJF Mean Sea Level Pressure (hPa)

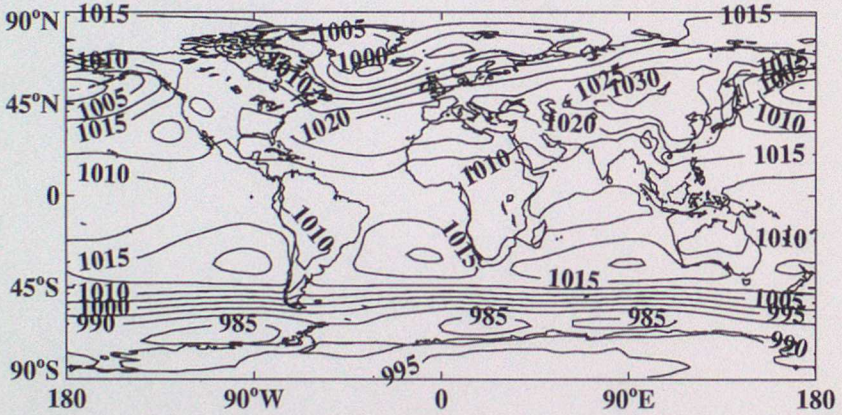

(d) ANALYSIS: JJA Mean Sea Level Pressure (hPa)

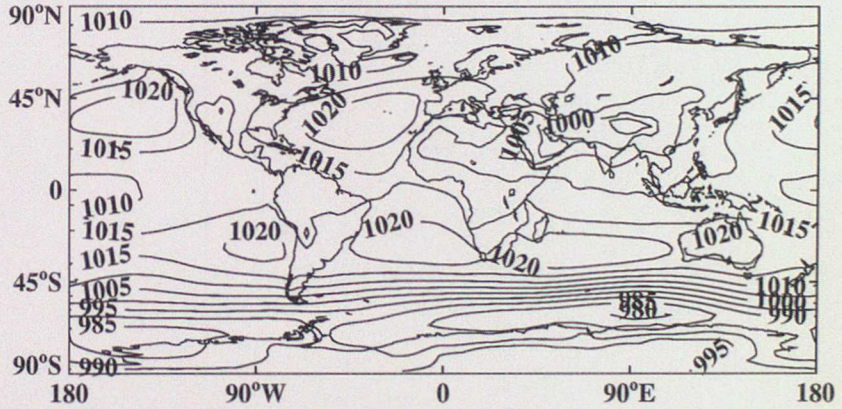

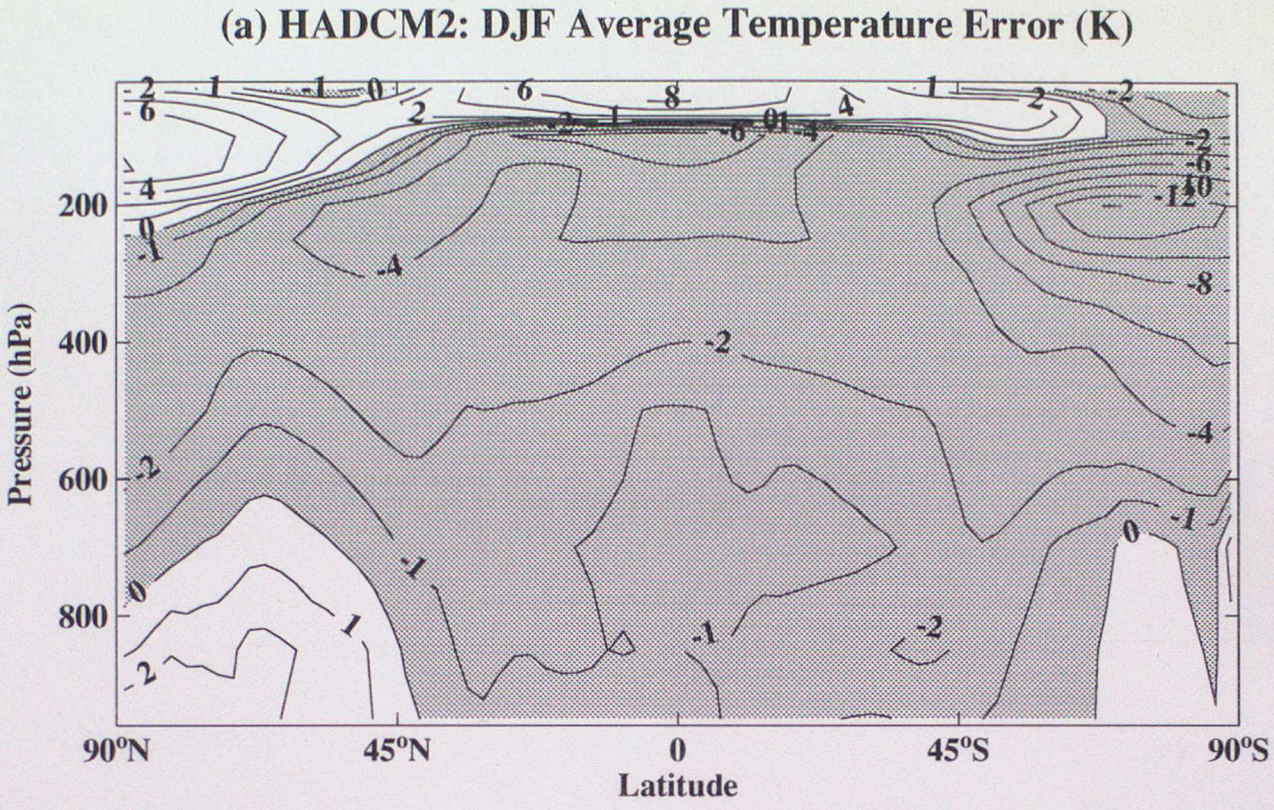
(a) HADCM2: DJF Average Temperature Error (K)
Pressure (hPa)
200
400
600
800
90°N
45°N
0
45°S
90°S
Latitude

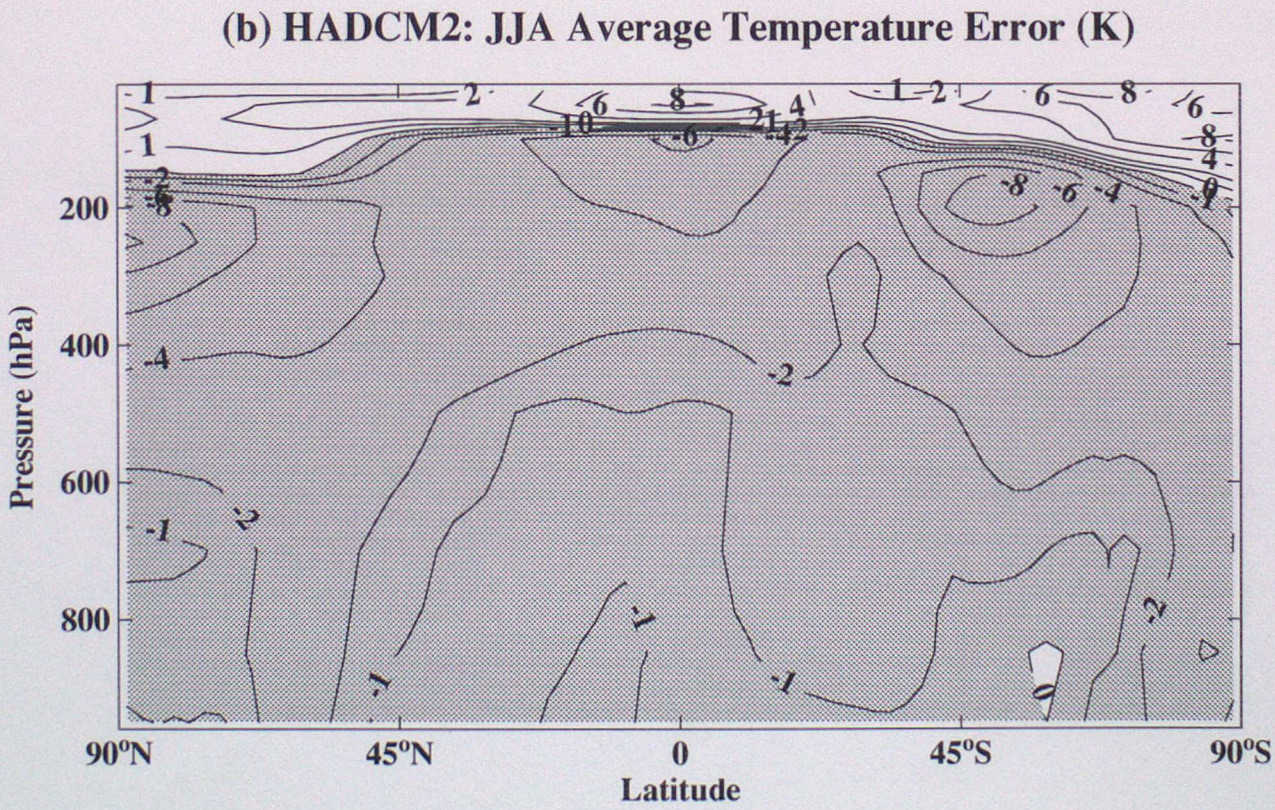
(b) HADCM2: JJA Average Temperature Error (K)
Pressure (hPa)
200
400
600
800
90°N
45°N
0
45°S
90°S
Latitude

Figure 11

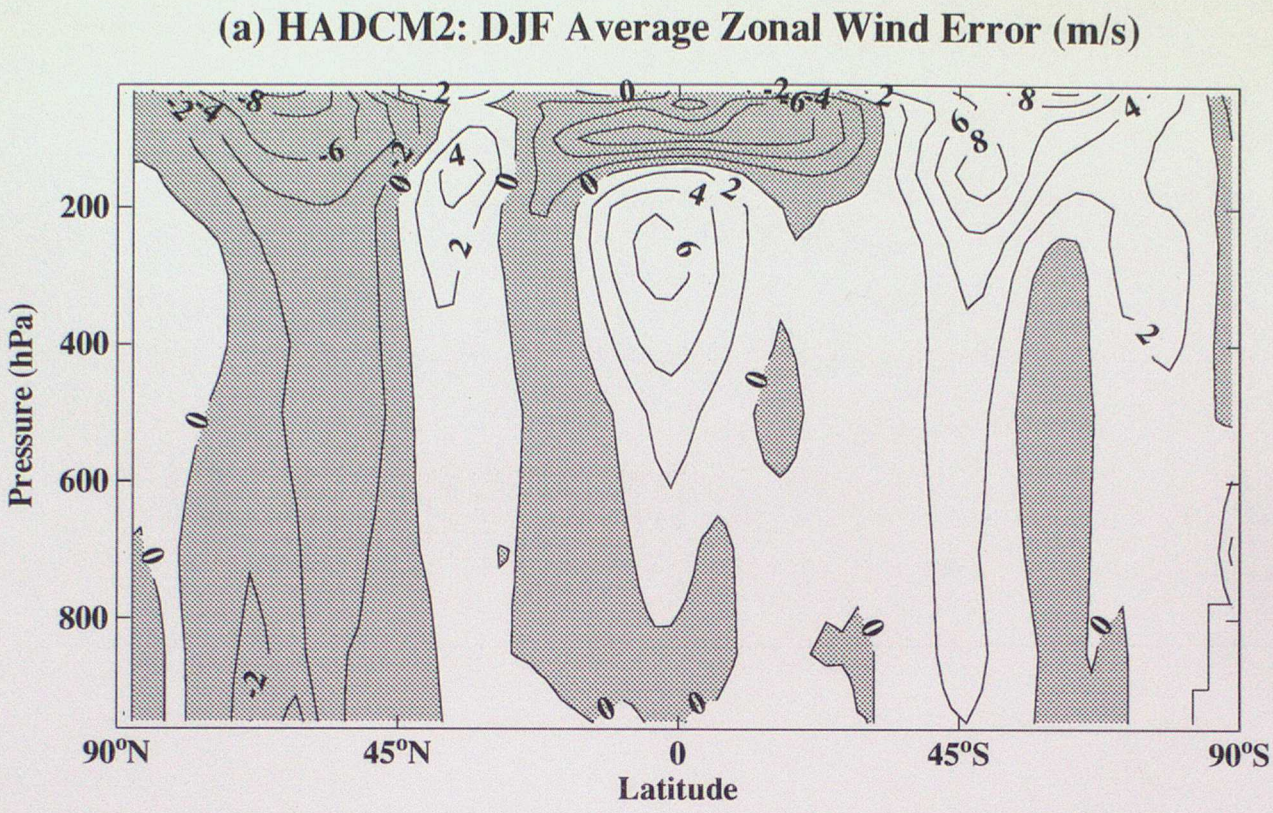
(a) HADCM2: DJF Average Zonal Wind Error (m/s)
Pressure (hPa)
200
400
600
800
90°N
45°N
0
45°S
90°S
Latitude

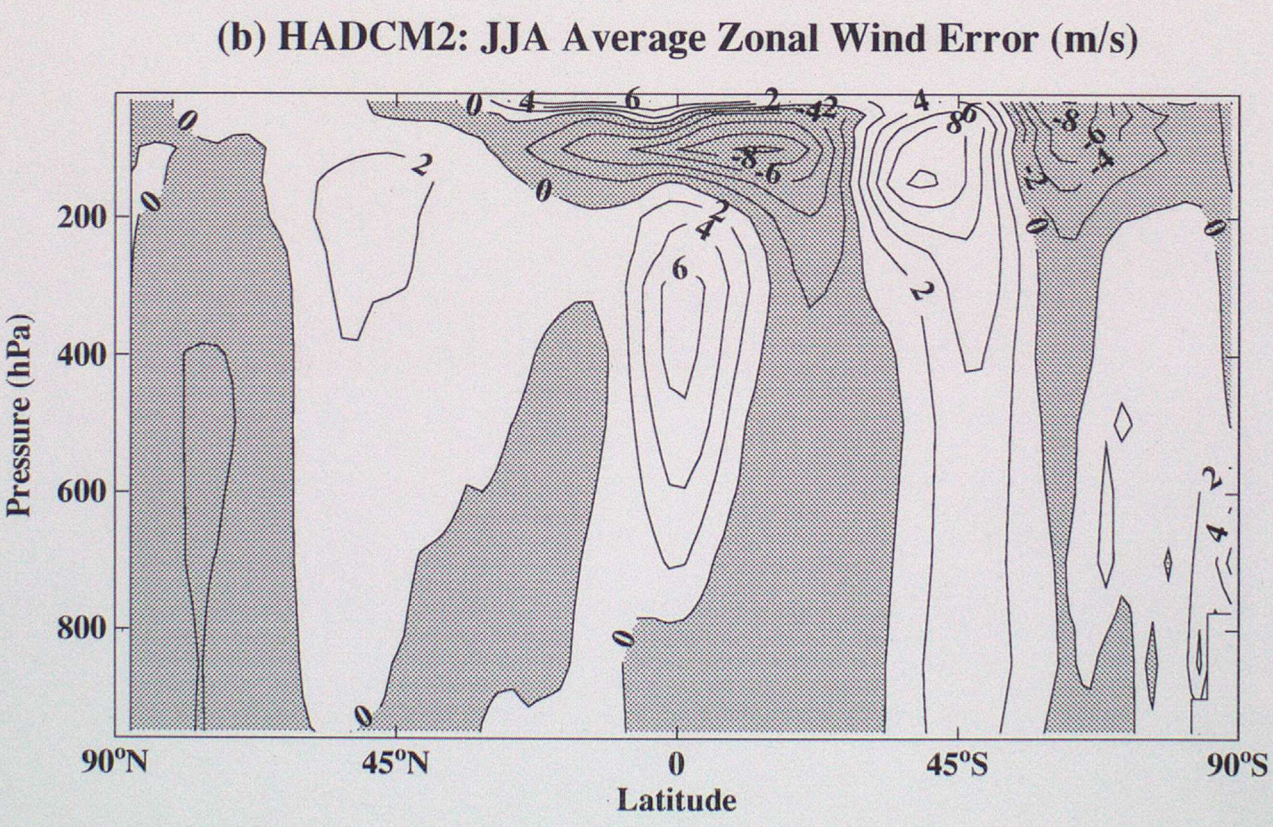
(b) HADCM2: JJA Average Zonal Wind Error (m/s)
Pressure (hPa)
200
400
600
800
90°N
45°N
0
45°S
90°S
Latitude

Figure 12

(a) HADCM2: DJF Average Streamfunction (10^9 kg/s)

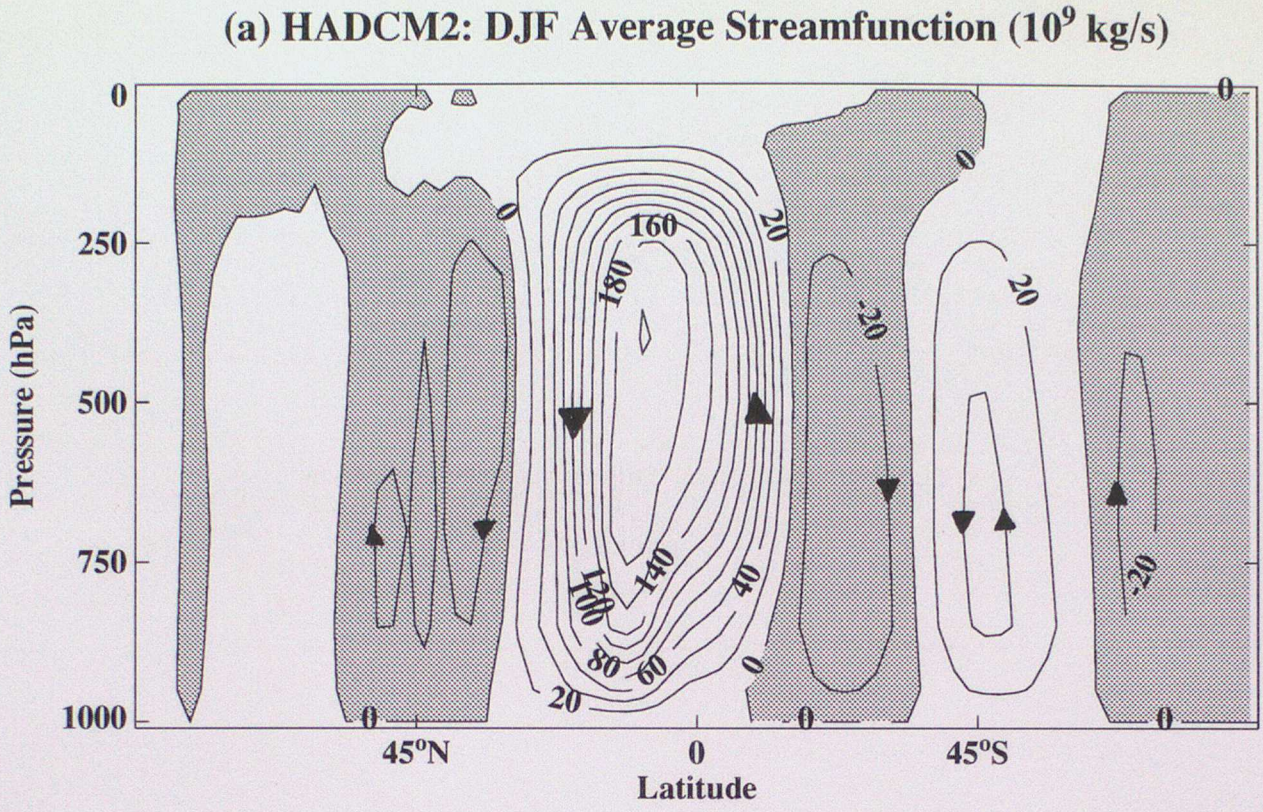

(b) HADCM2: JJA Average Streamfunction (10^9 kg/s)

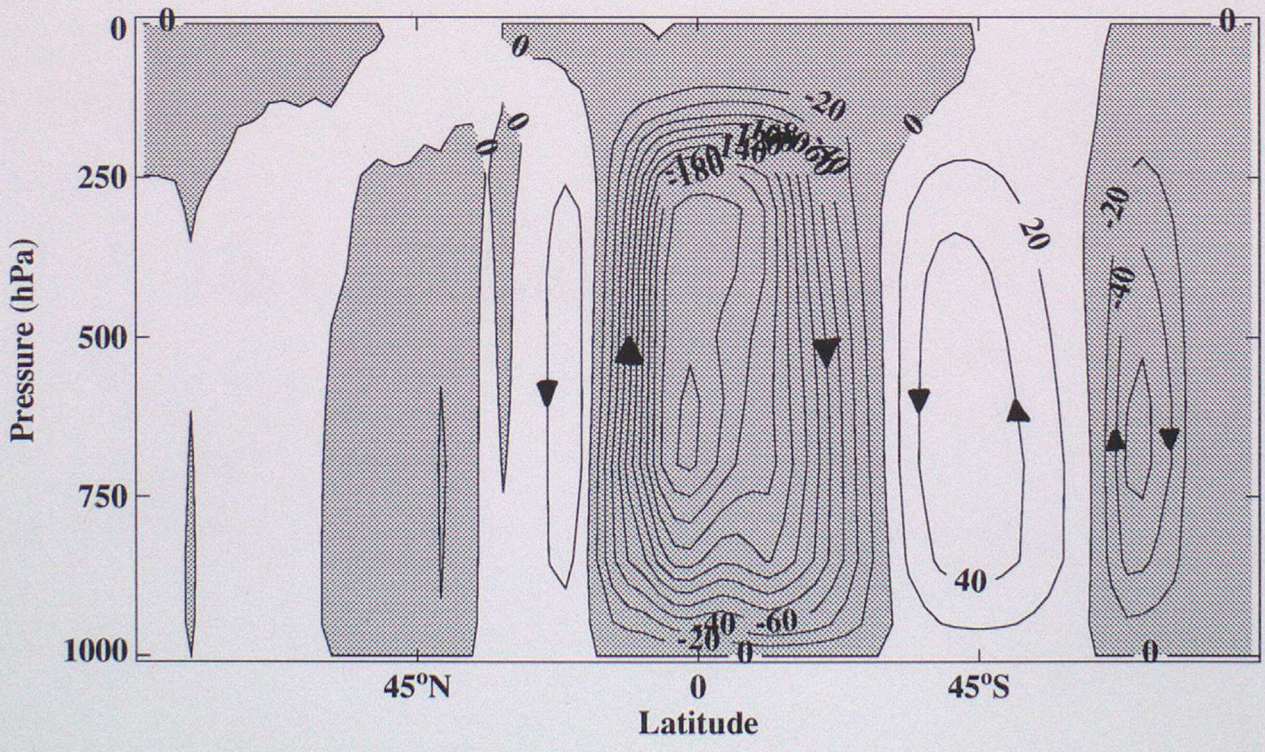

Figure 13

Band Pass Filtered 500 mb Height Field (dam)

HADCM2: DJF average

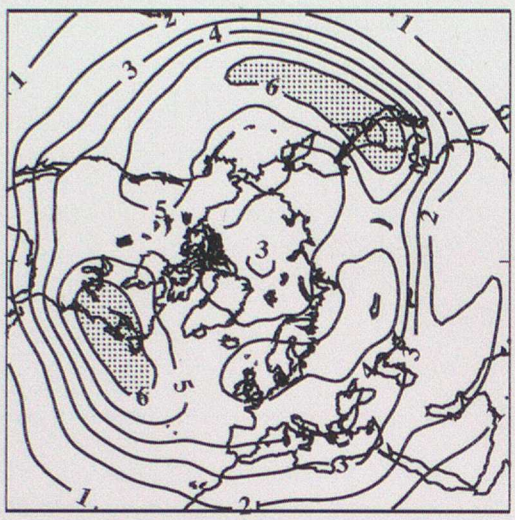

HADCM2: DJF average

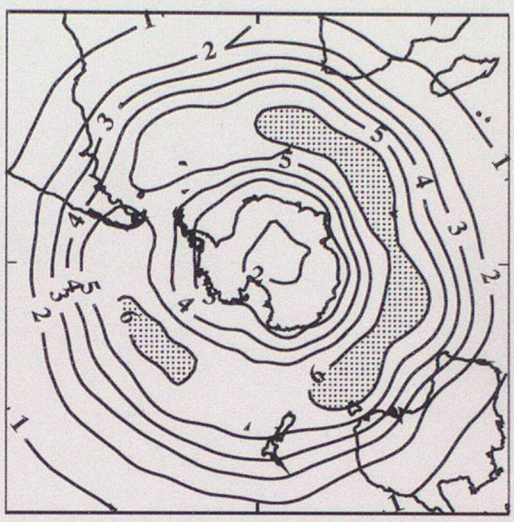

Analysis: DJF average

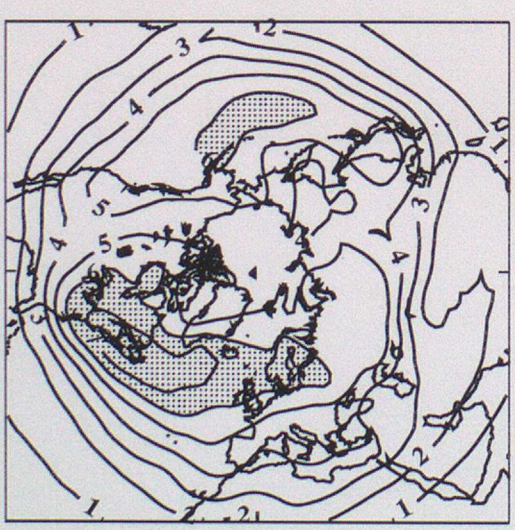

Analysis: DJF average

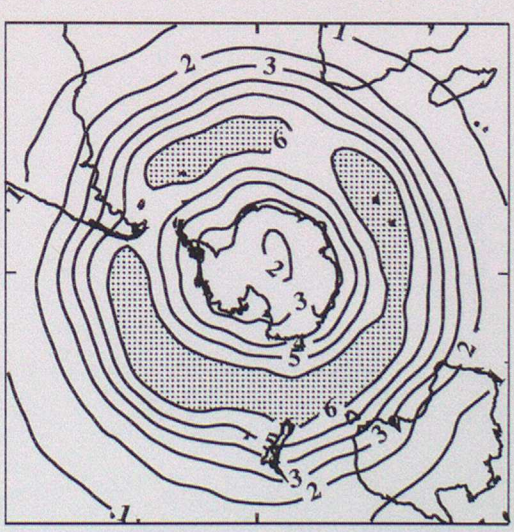

Figure 14

Band Pass Filtered 500 mb Height Field (dam)

HADCM2: JJA average

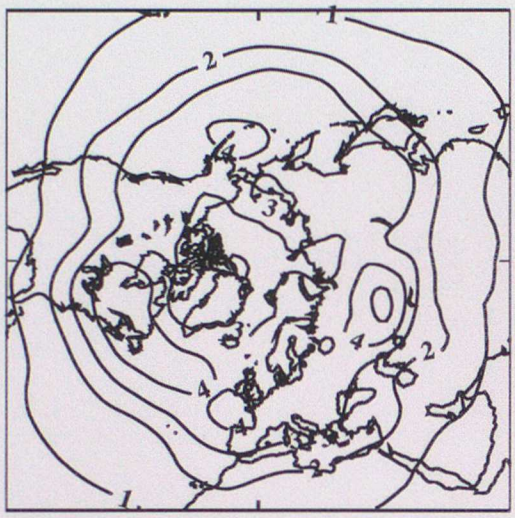

HADCM2: JJA average

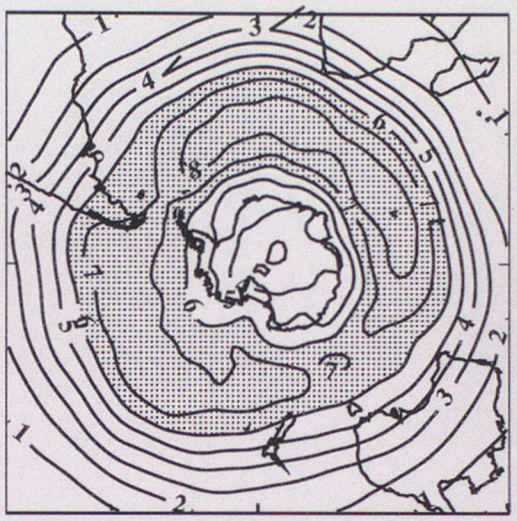

Analysis: JJA average

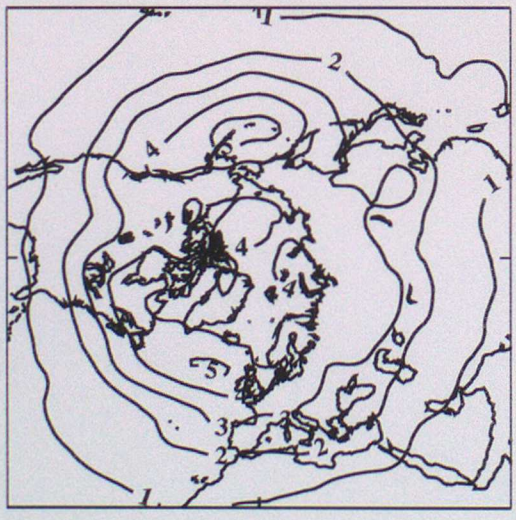

Analysis: JJA average

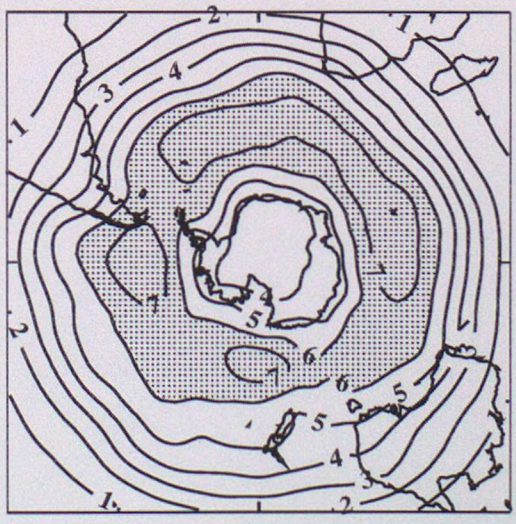

Figure 15

(a) HADCM2: Low counts

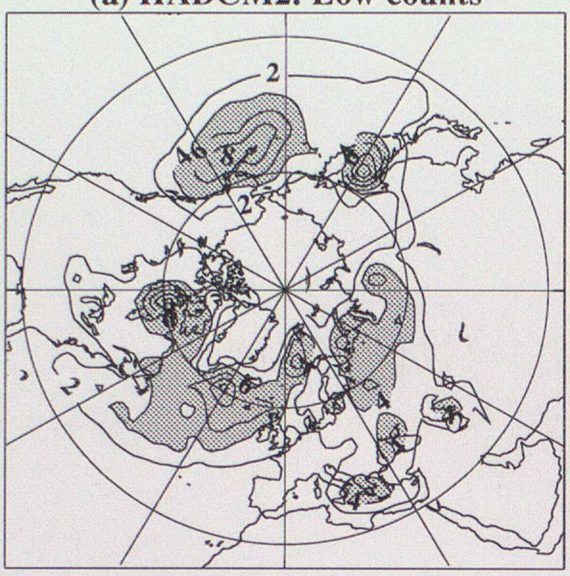

(b) Analysis: Low counts

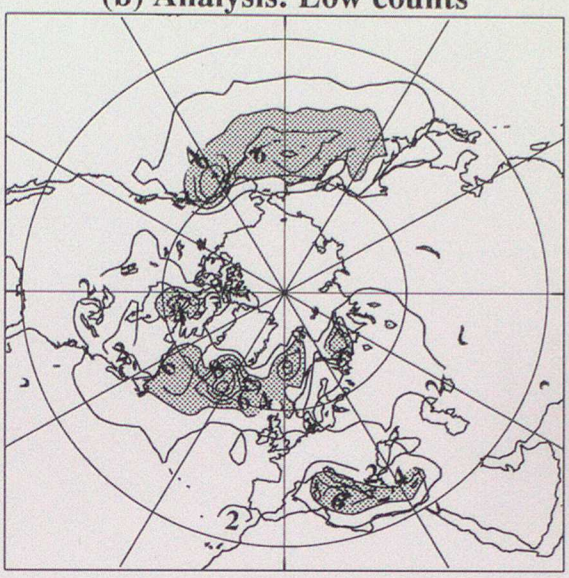

(c) UKTR: Low counts

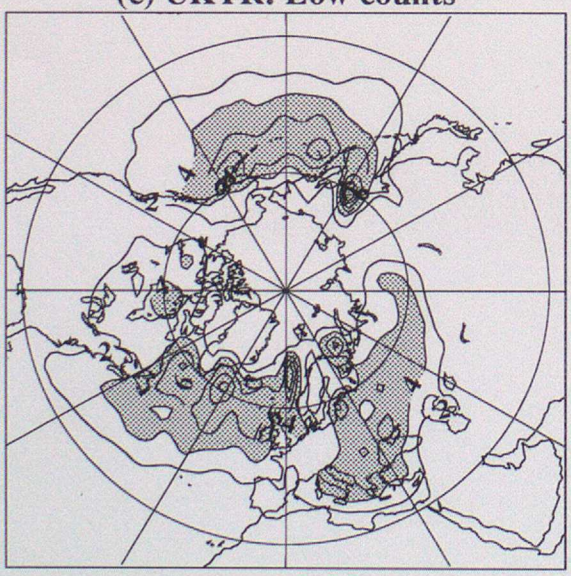

Figure 16

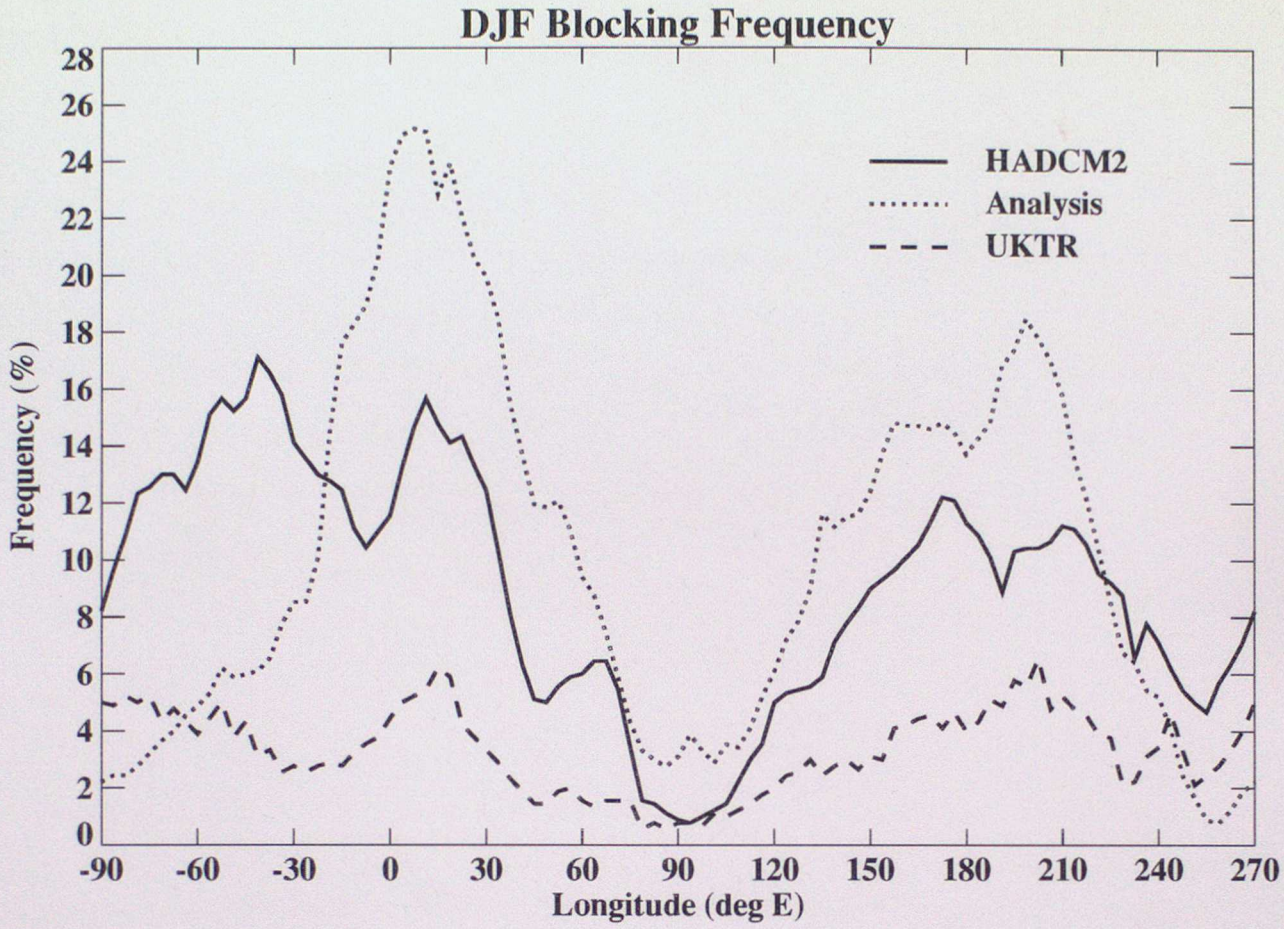
DJF Blocking Frequency
HADCM2
Analysis
UKTR
Frequency (%)
Longitude (deg E)
28
26
24
22
20
18
16
14
12
10
8
6
4
2
0
-90
-60
-30
0
30
60
90
120
150
180
210
240
270

Figure 17

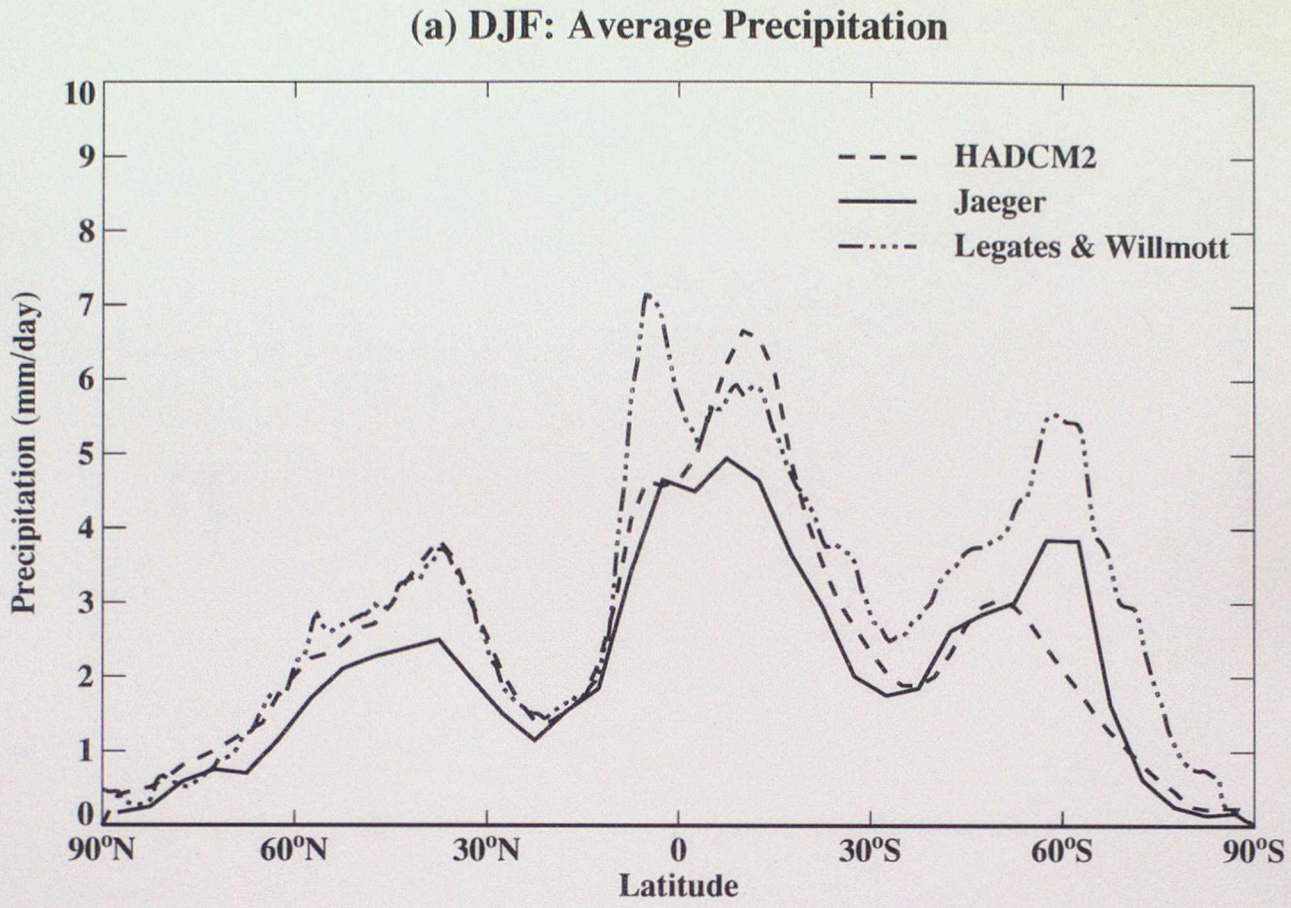
(a) DJF: Average Precipitation
HADCM2
Jaeger
Legates & Willmott
Precipitation (mm/day)
0
1
2
3
4
5
6
7
8
9
10
90°N
60°N
30°N
0
30°S
60°S
90°S
Latitude

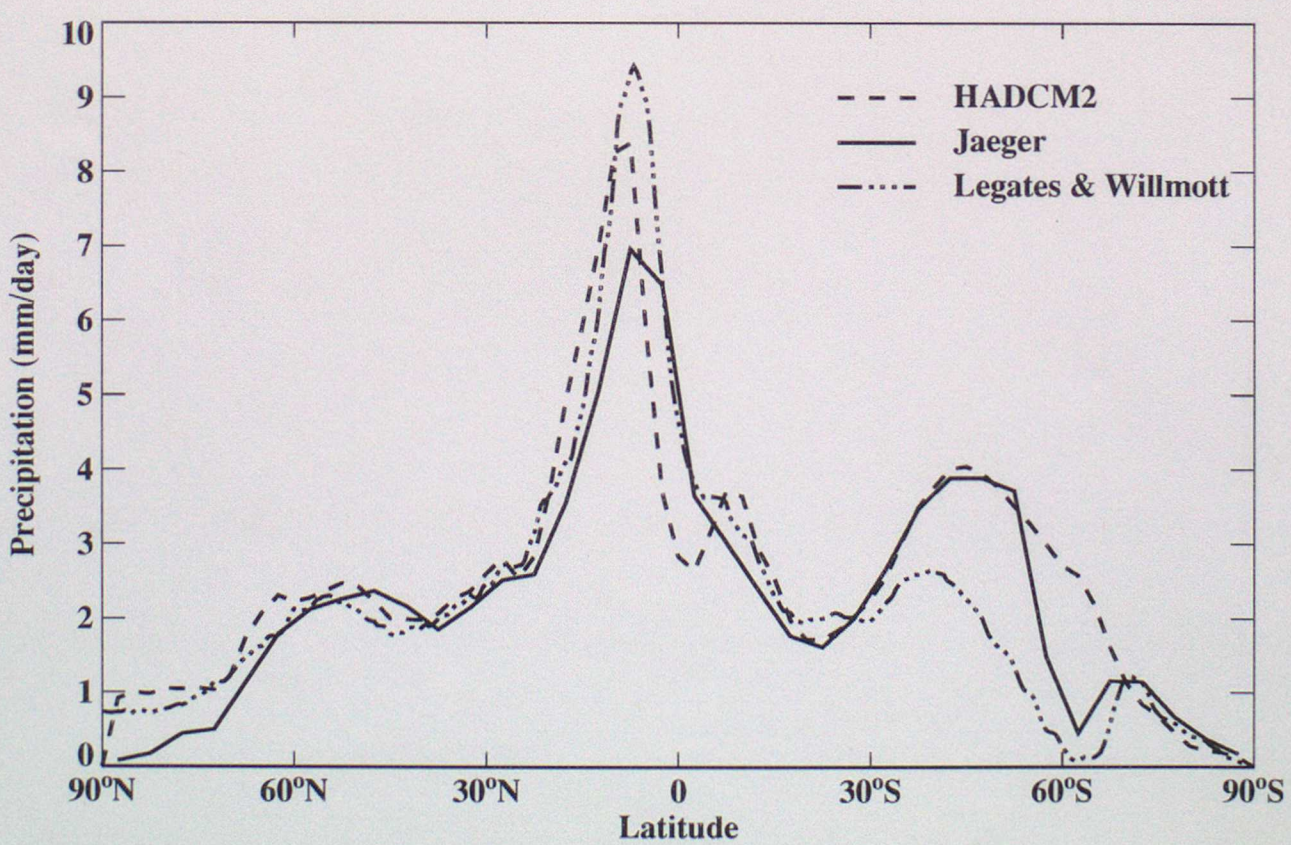
(b) JJA: Average Precipitation
HADCM2
Jaeger
Legates & Willmott
Precipitation (mm/day)
0
1
2
3
4
5
6
7
8
9
10
90°N
60°N
30°N
0
30°S
60°S
90°S
Latitude

Figure 18

(a) DJF: Average Precipitation (mm/day)

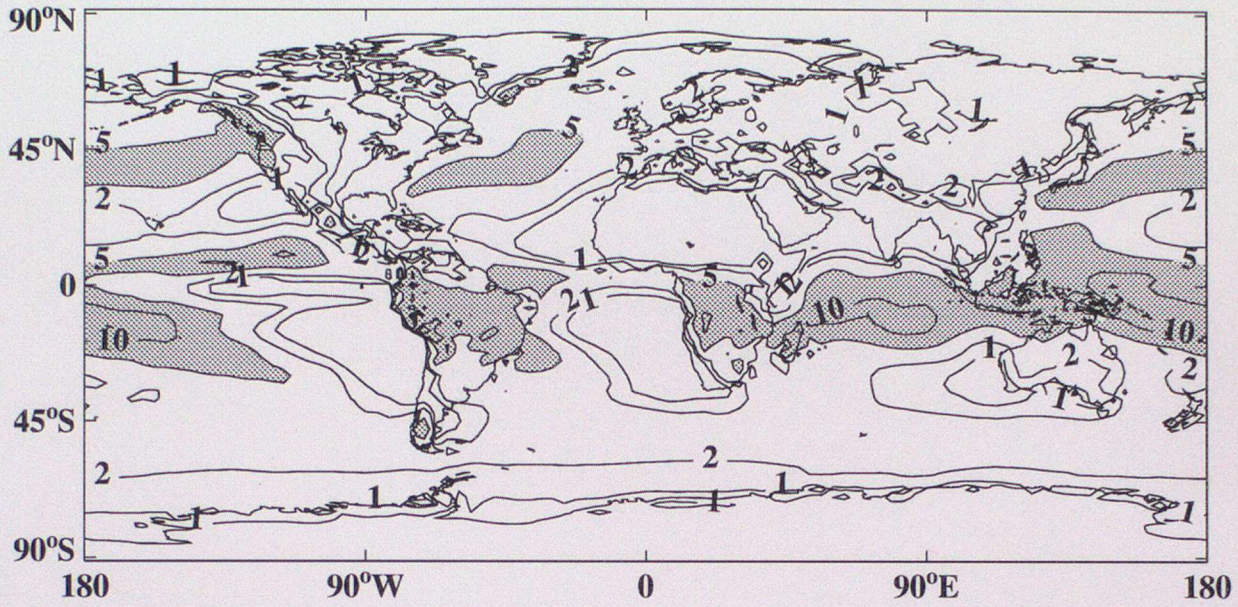

(b) JJA: Average Precipitation (mm/day)

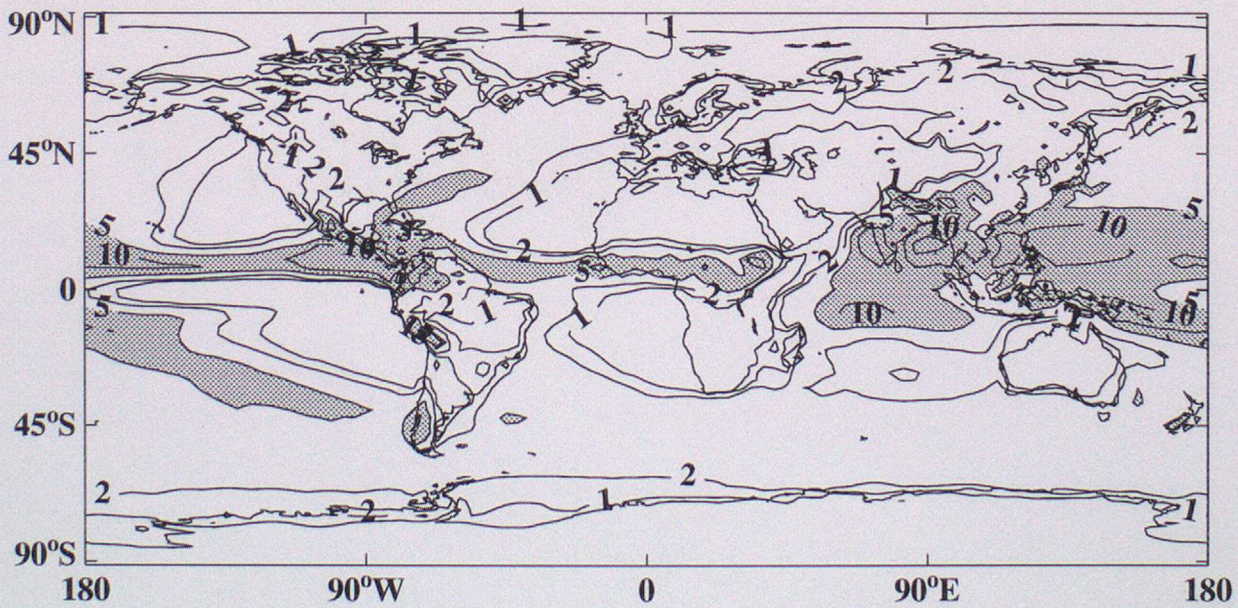

Figure 19

(a) DJF: Average Soil Moisture Content (mm)

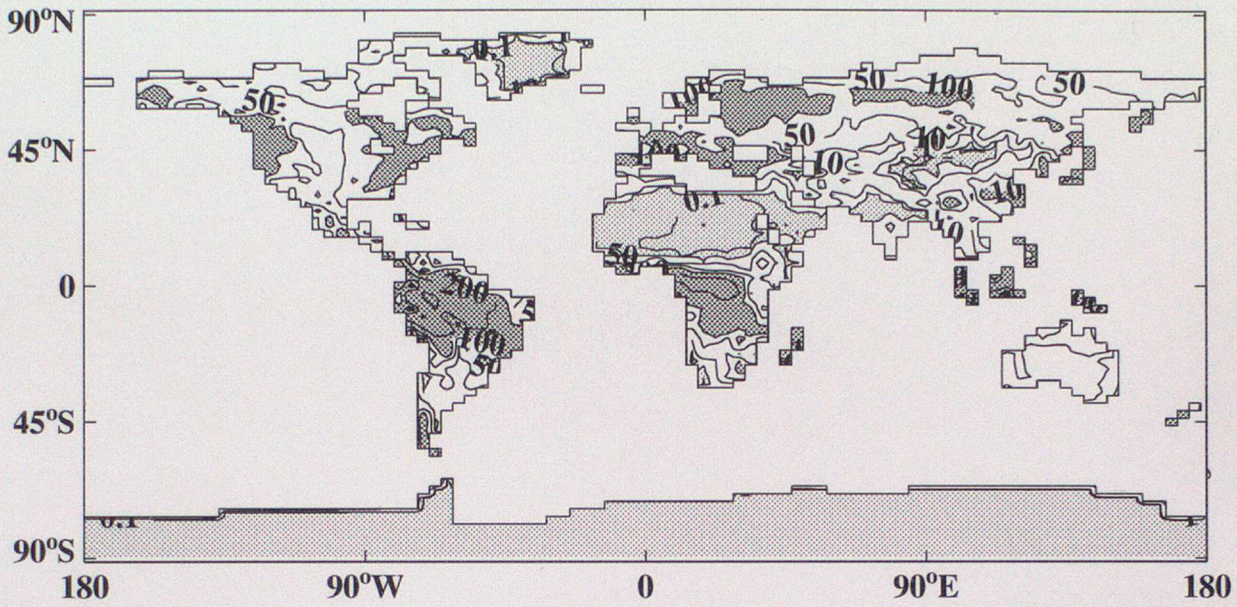

(b) JJA: Average Soil Moisture Content (mm)

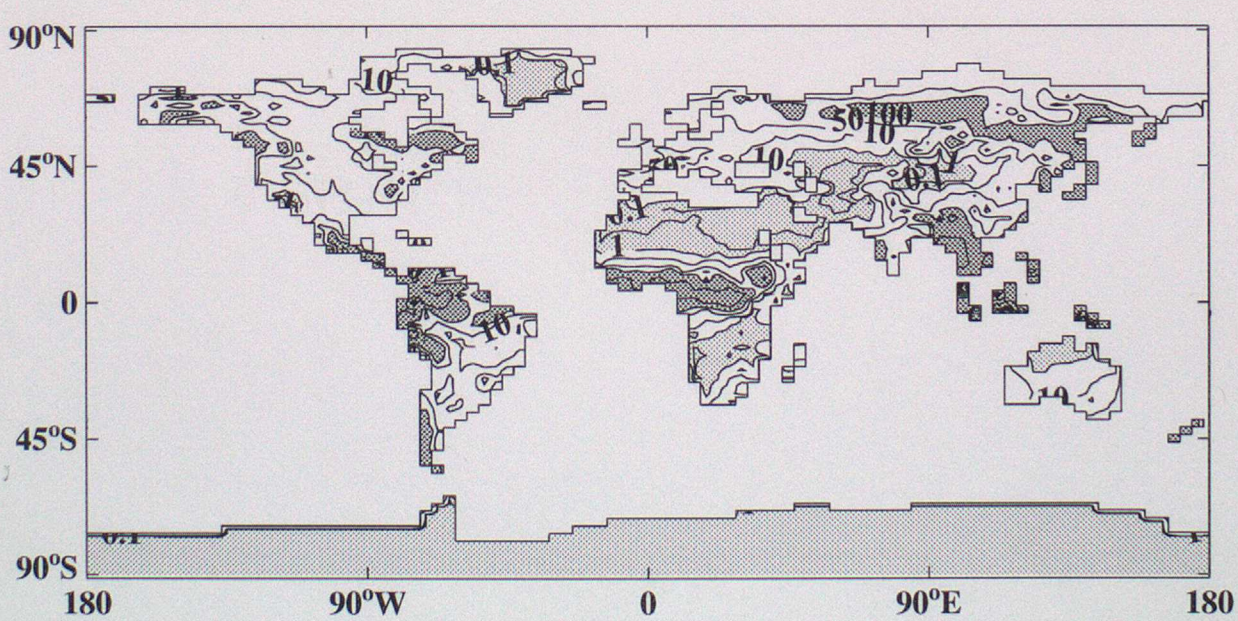

Figure 20

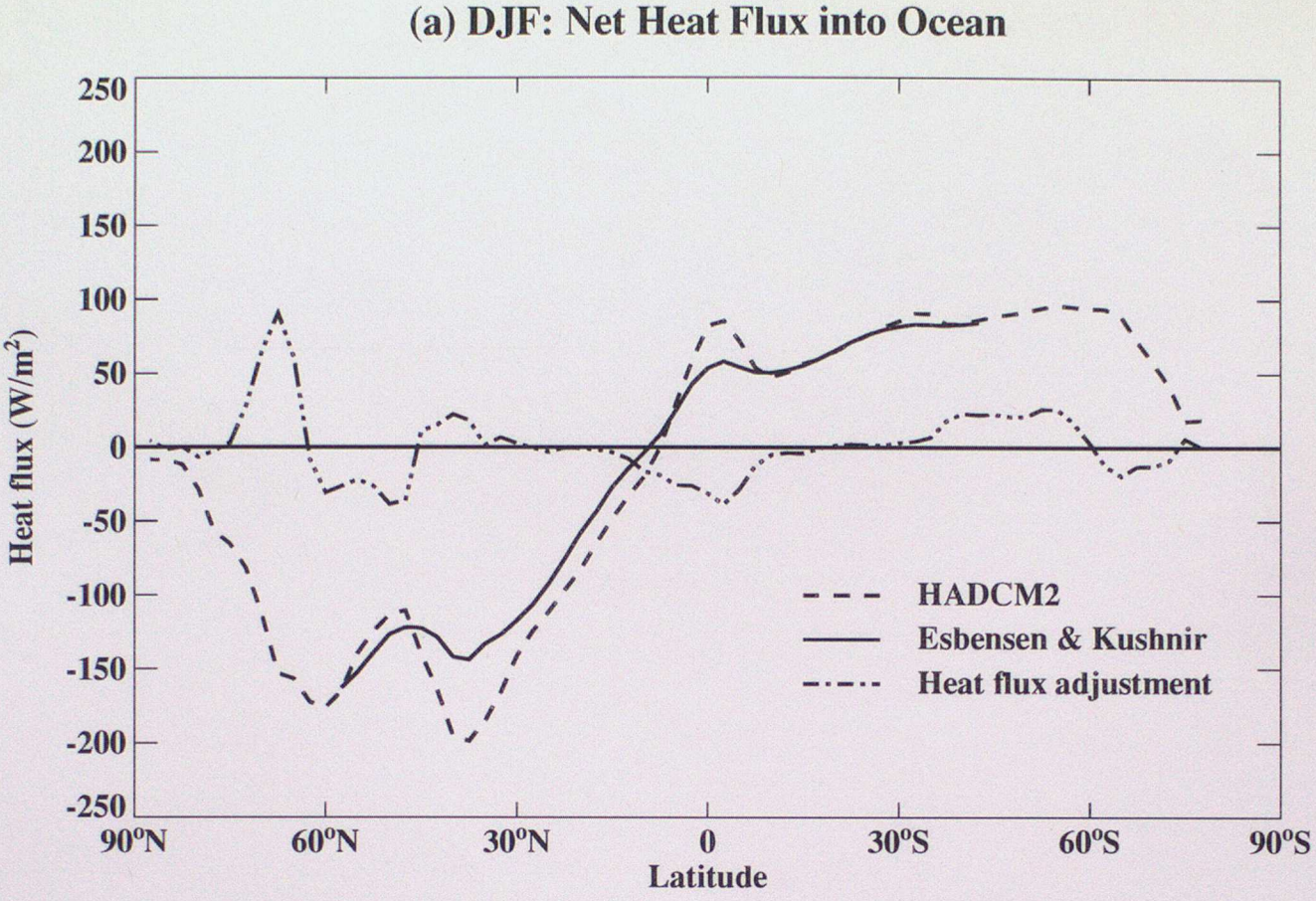
(a) DJF: Net Heat Flux into Ocean
Heat flux (W/m^2)
250
200
150
100
50
0
-50
-100
-150
-200
-250
90°N
60°N
30°N
0
30°S
60°S
90°S
Latitude
HADCM2
Esbensen & Kushnir
Heat flux adjustment

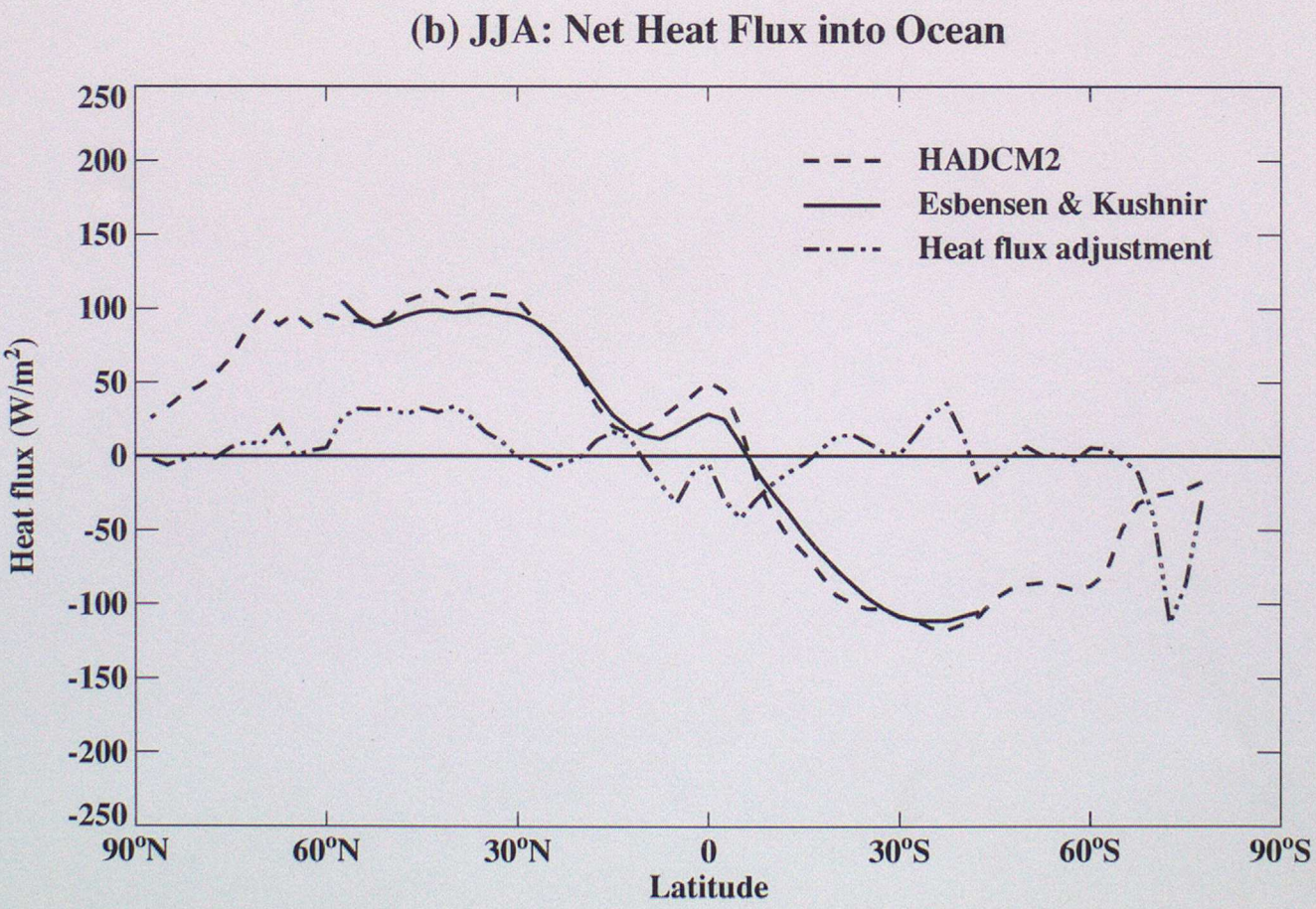
(b) JJA: Net Heat Flux into Ocean
Heat flux (W/m^2)
250
200
150
100
50
0
-50
-100
-150
-200
-250
90°N
60°N
30°N
0
30°S
60°S
90°S
Latitude
HADCM2
Esbensen & Kushnir
Heat flux adjustment

Figure 21

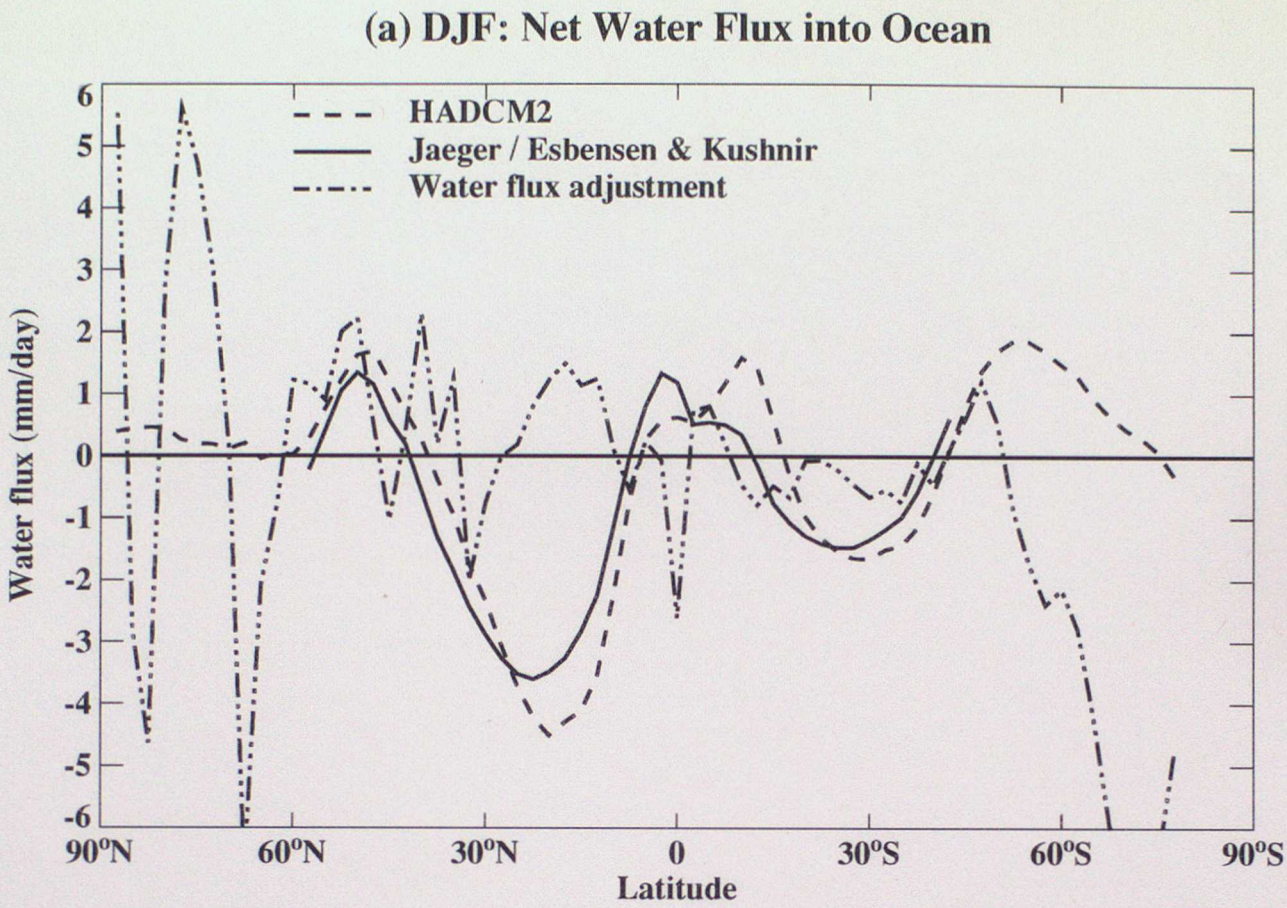
(a) DJF: Net Water Flux into Ocean
HADCM2
Jaeger / Esbensen & Kushnir
Water flux adjustment
Water flux (mm/day)
6
5
4
3
2
1
0
-1
-2
-3
-4
-5
-6
90°N
60°N
30°N
0
30°S
60°S
90°S
Latitude

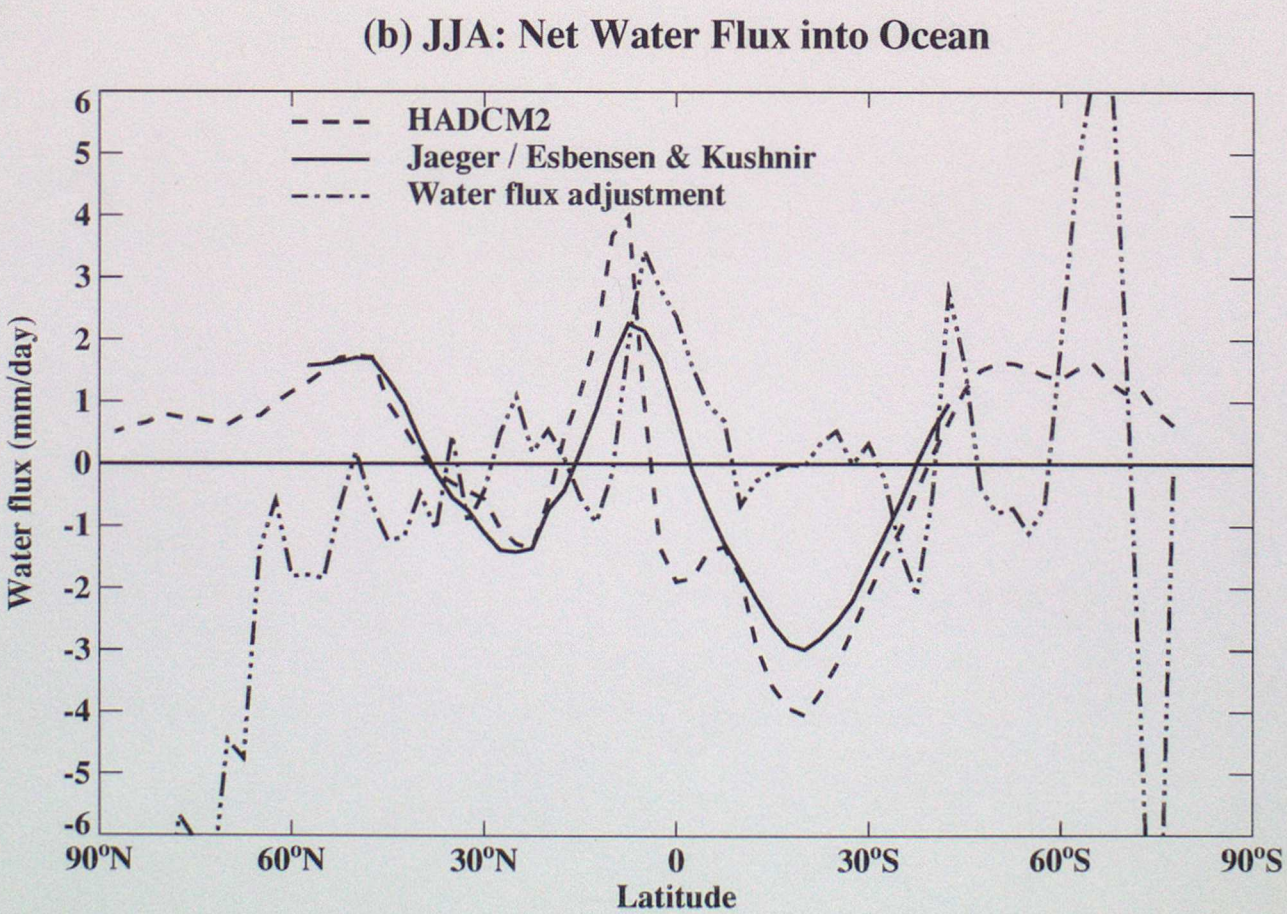
(b) JJA: Net Water Flux into Ocean
HADCM2
Jaeger / Esbensen & Kushnir
Water flux adjustment
Water flux (mm/day)
6
5
4
3
2
1
0
-1
-2
-3
-4
-5
-6
90°N
60°N
30°N
0
30°S
60°S
90°S
Latitude

Figure 22

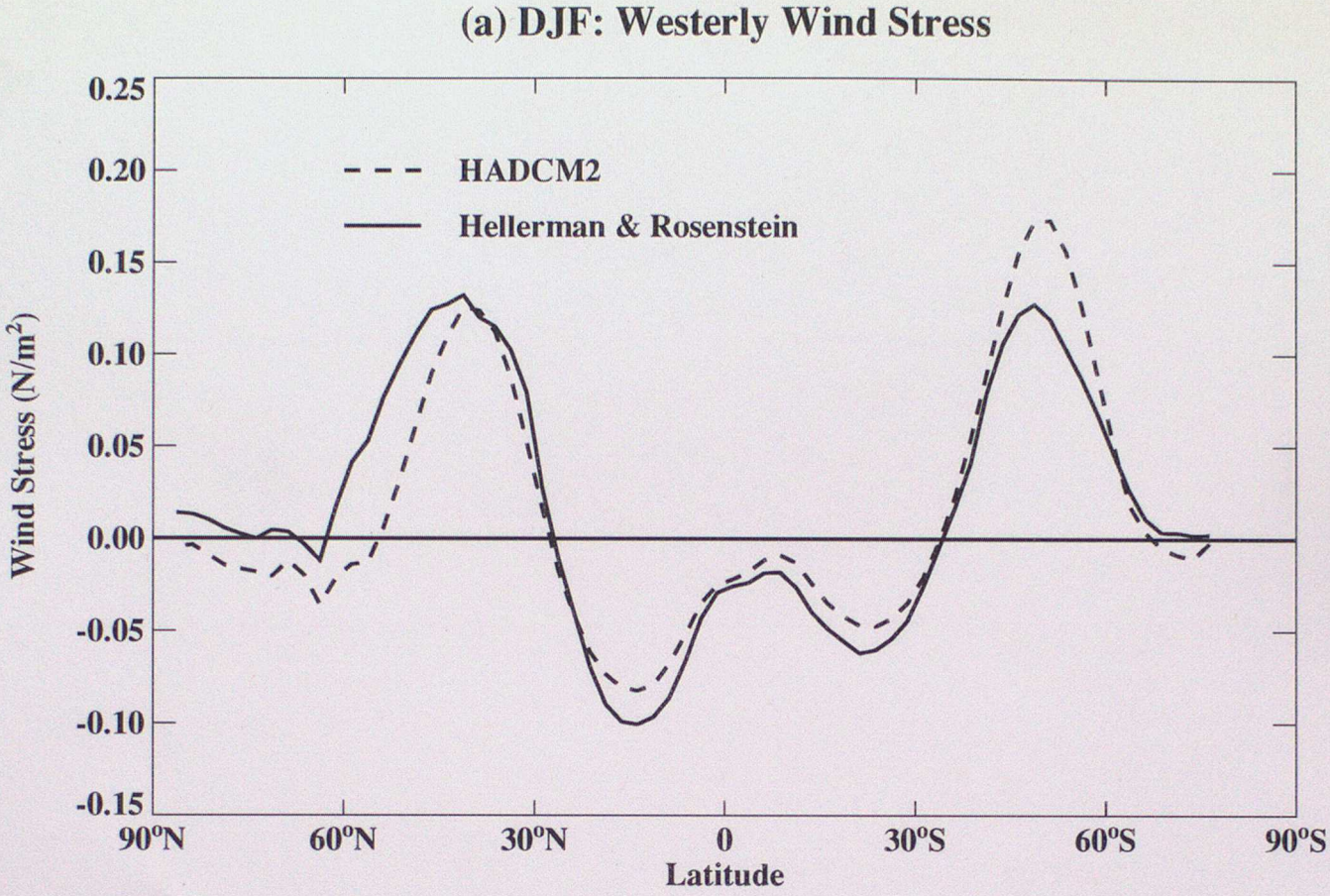
(a) DJF: Westerly Wind Stress
HADCM2
Hellerman & Rosenstein
Wind Stress (N/m²)
0.25
0.20
0.15
0.10
0.05
0.00
-0.05
-0.10
-0.15
90°N
60°N
30°N
0
30°S
60°S
90°S
Latitude

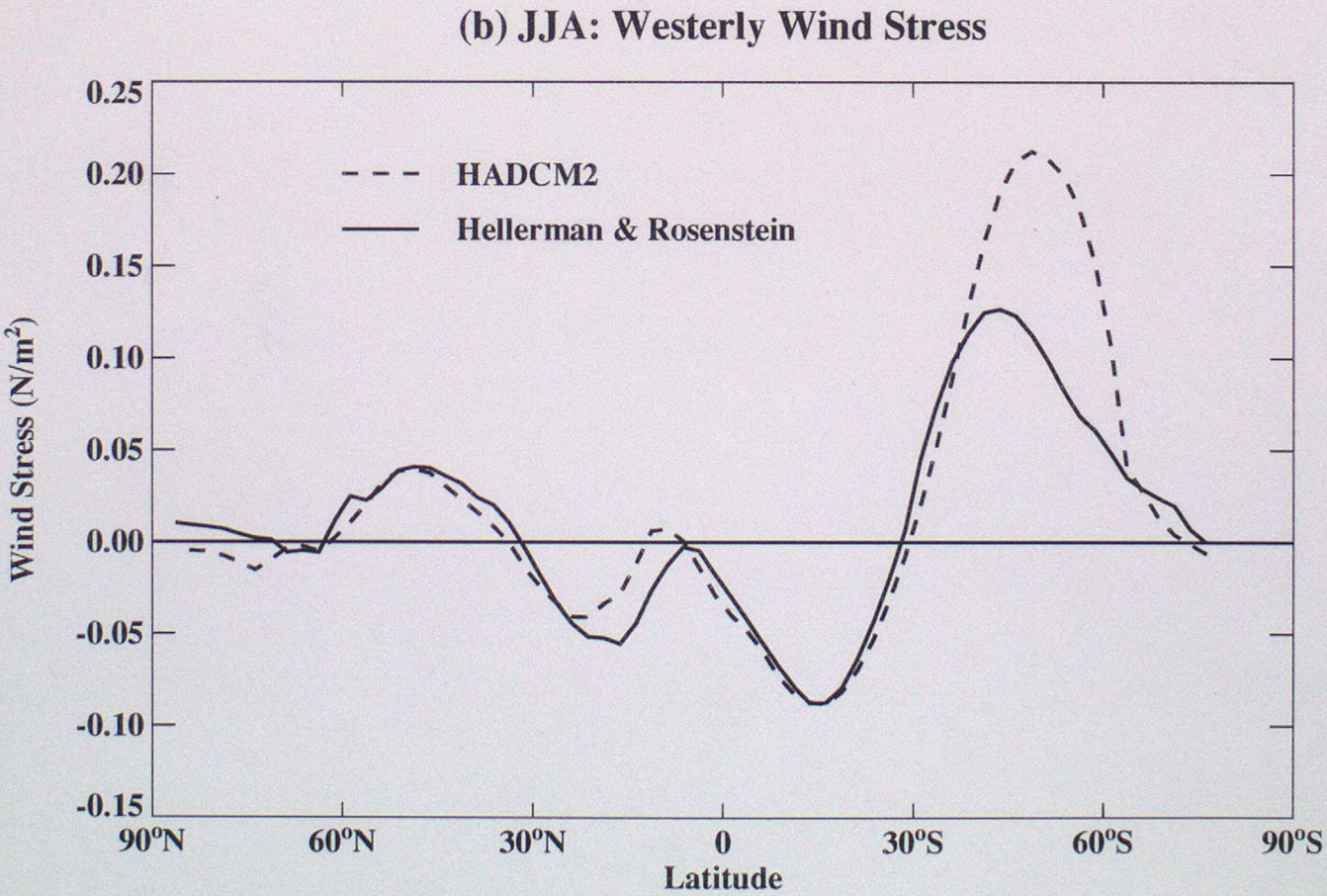
(b) JJA: Westerly Wind Stress
HADCM2
Hellerman & Rosenstein
Wind Stress (N/m²)
0.25
0.20
0.15
0.10
0.05
0.00
-0.05
-0.10
-0.15
90°N
60°N
30°N
0
30°S
60°S
90°S
Latitude

Figure 23

(a) Annual Average Heat Flux Adjustment (W/m^2)

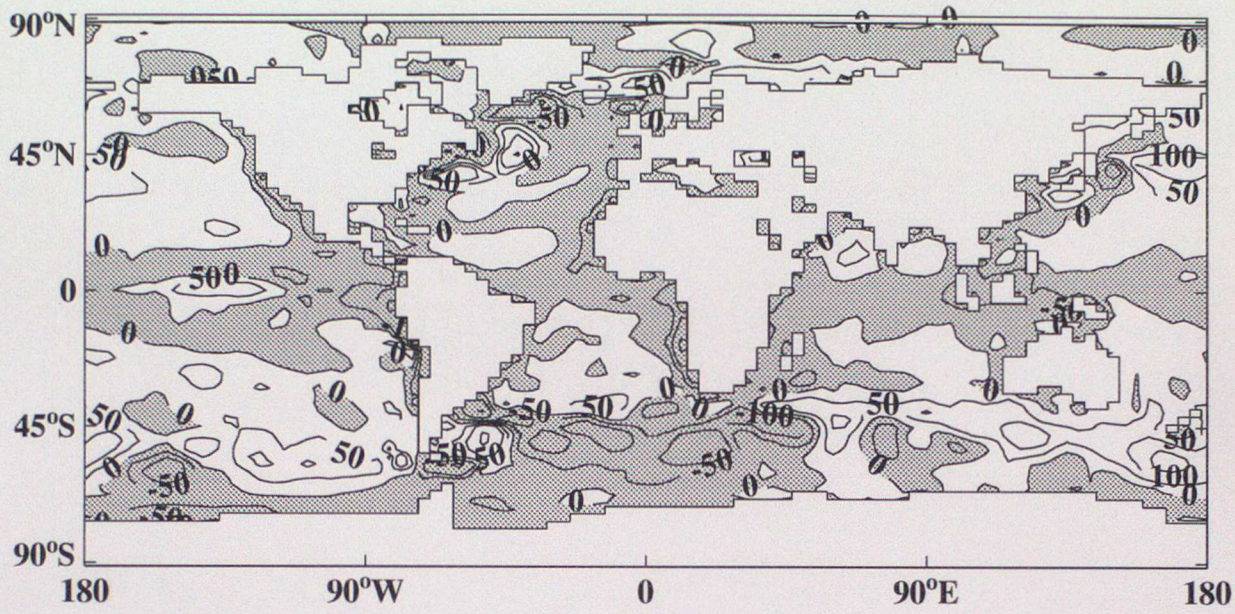

(b) Annual Average Water Flux Adjustment (mm/day)

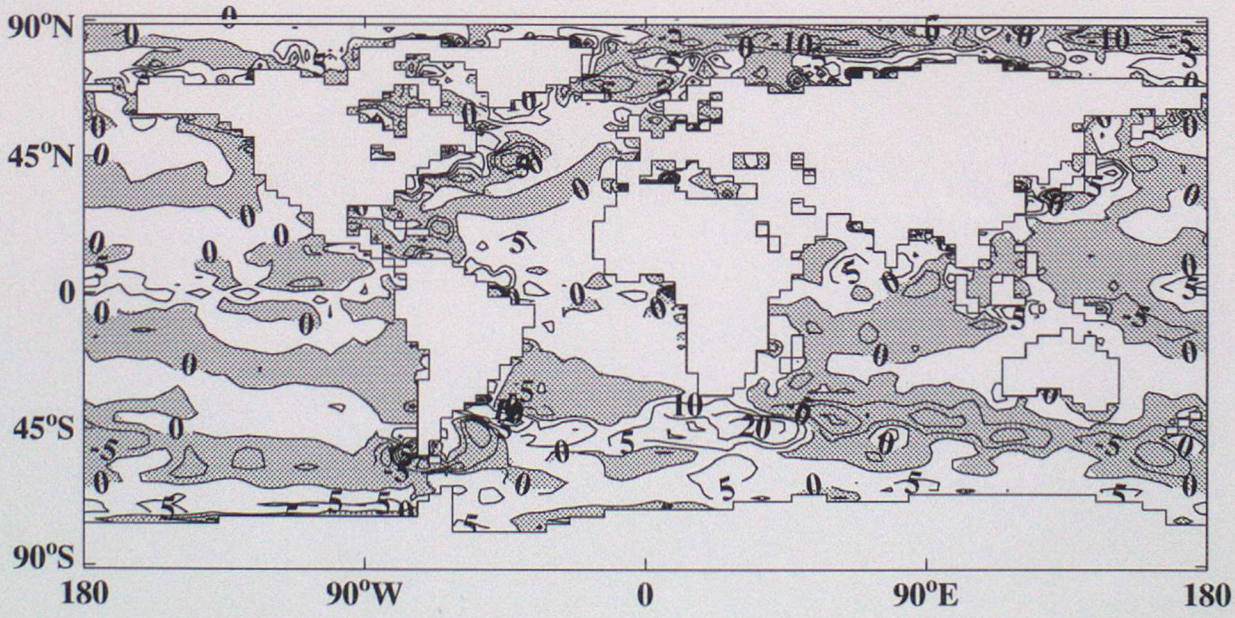

Figure 24

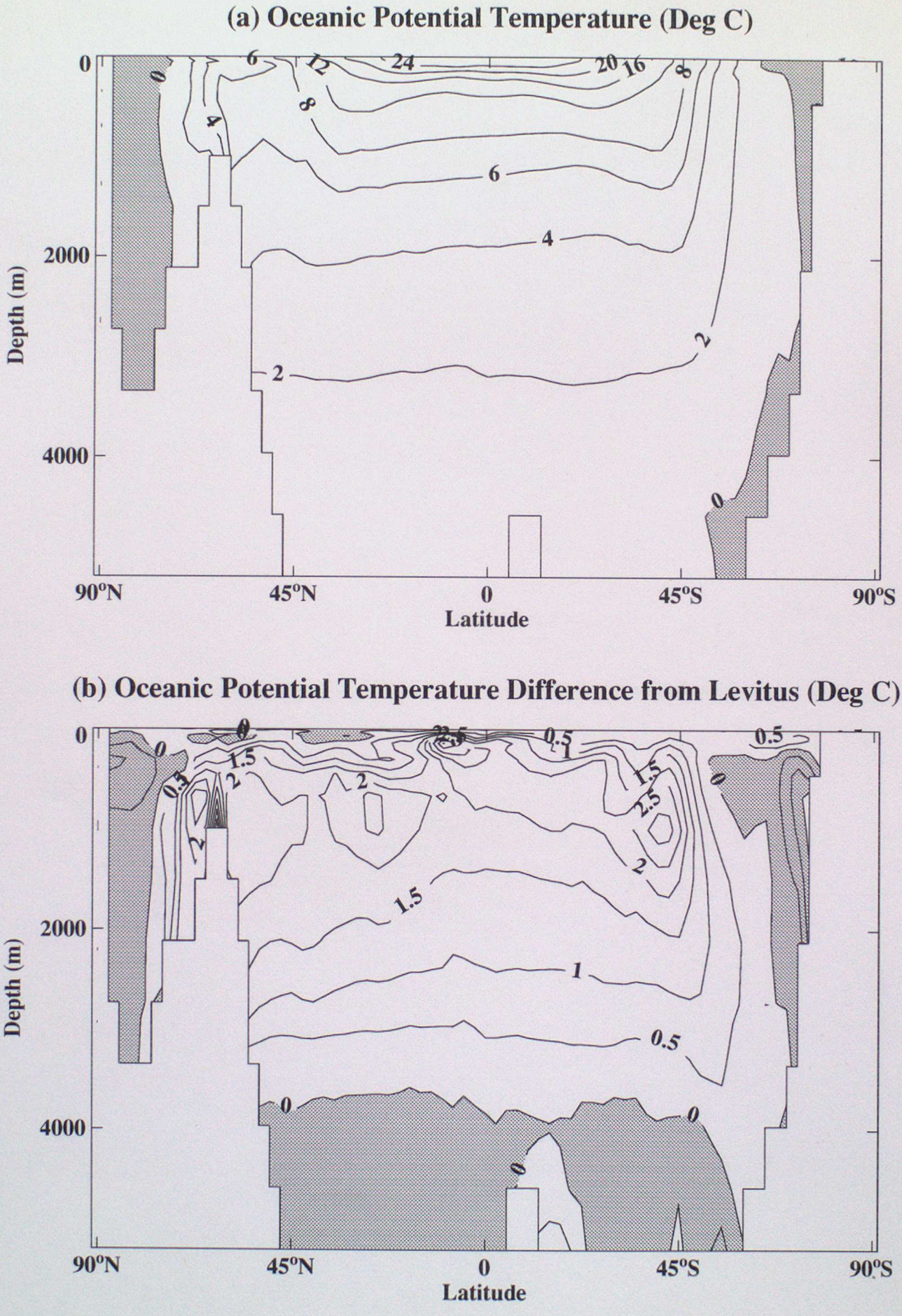
(a) Oceanic Potential Temperature (Deg C)
Depth (m)
0
2000
4000
90°N
45°N
0
45°S
90°S
Latitude
(b) Oceanic Potential Temperature Difference from Levitus (Deg C)
Depth (m)
0
2000
4000
90°N
45°N
0
45°S
90°S
Latitude

Figure 25

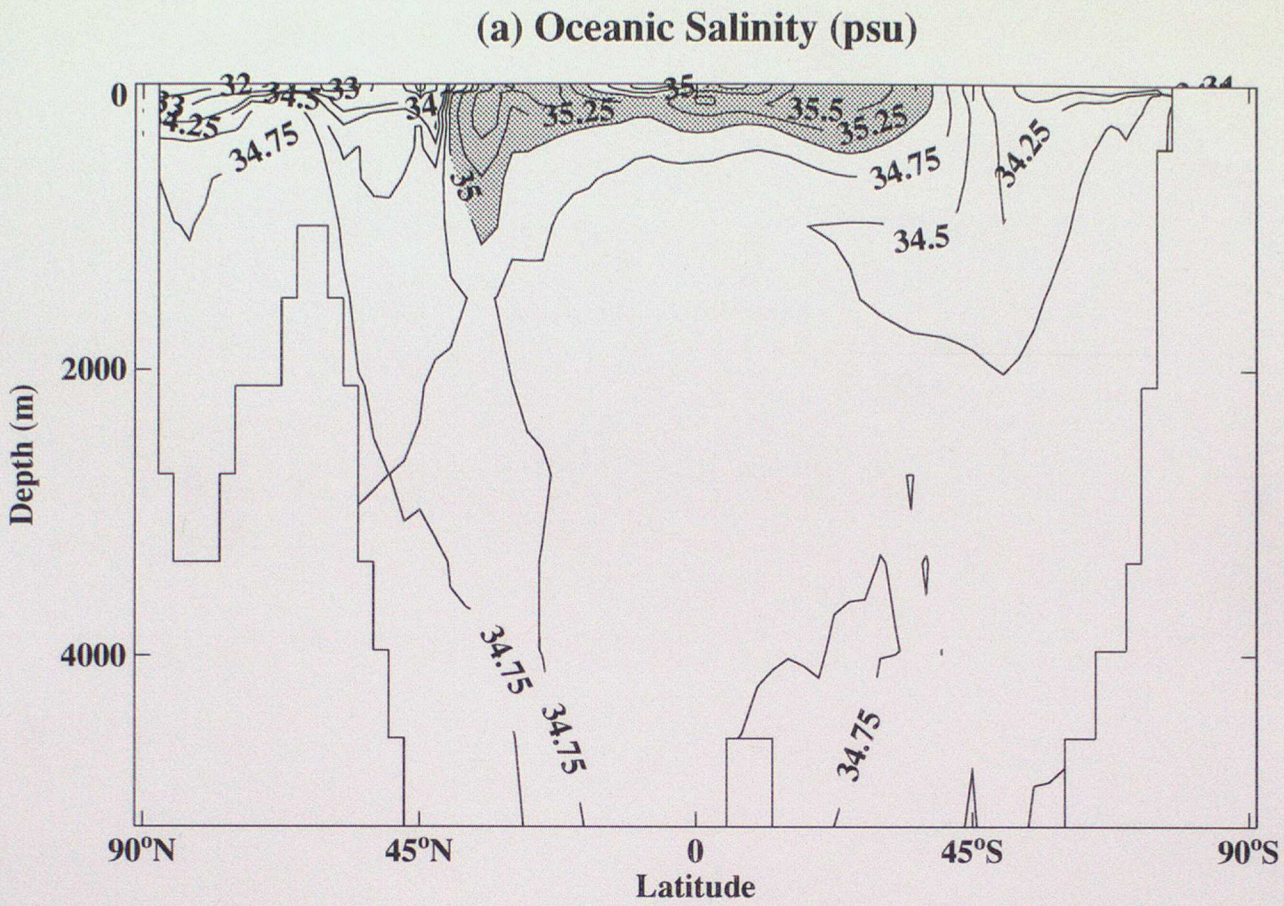
(a) Oceanic Salinity (psu)
Depth (m)
0
2000
4000
90°N
45°N
0
45°S
90°S
Latitude
34.75
35.25
35.5
34.25
34.5
35

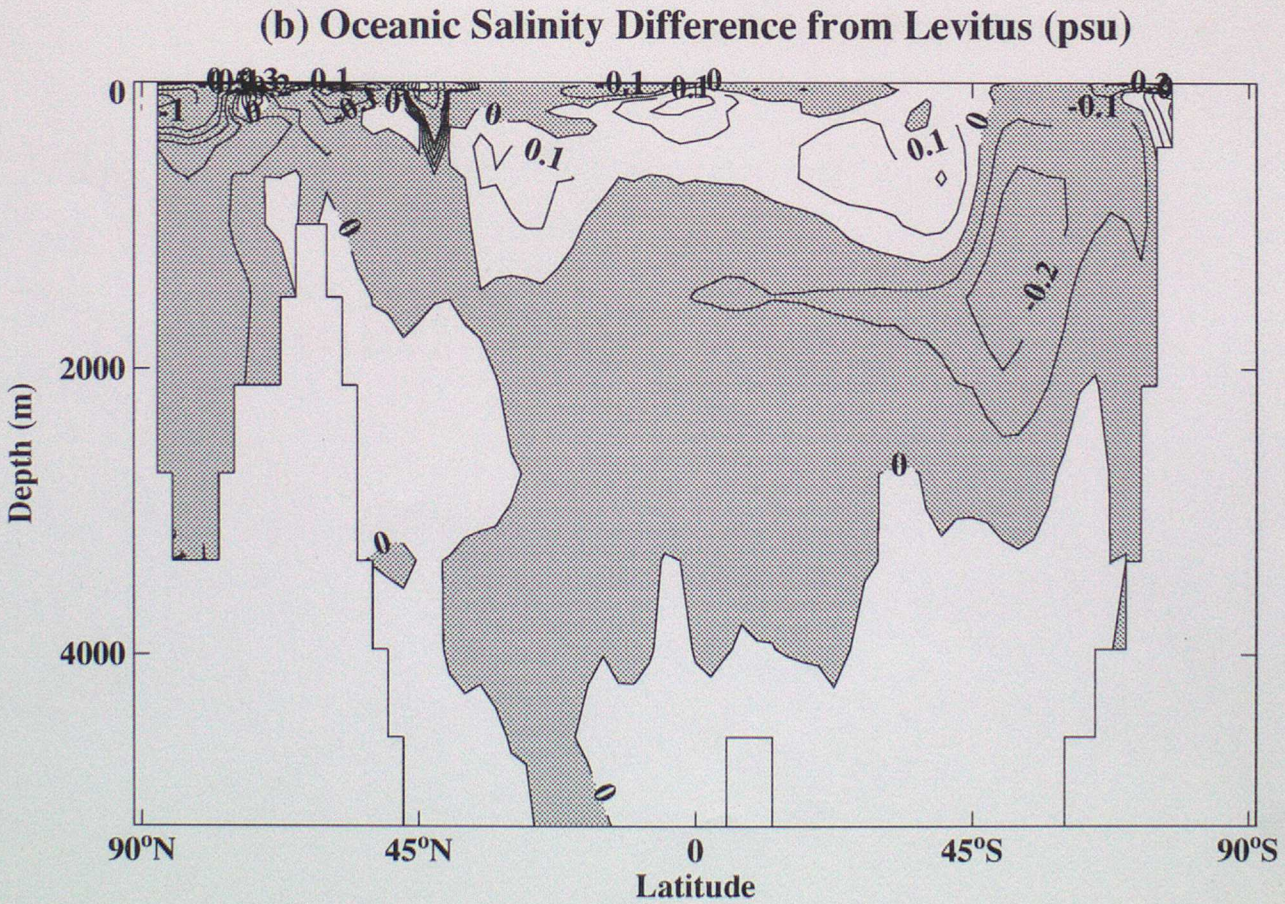
(b) Oceanic Salinity Difference from Levitus (psu)
Depth (m)
0
2000
4000
90°N
45°N
0
45°S
90°S
Latitude
0.1
-0.1
-0.2

Figure 26

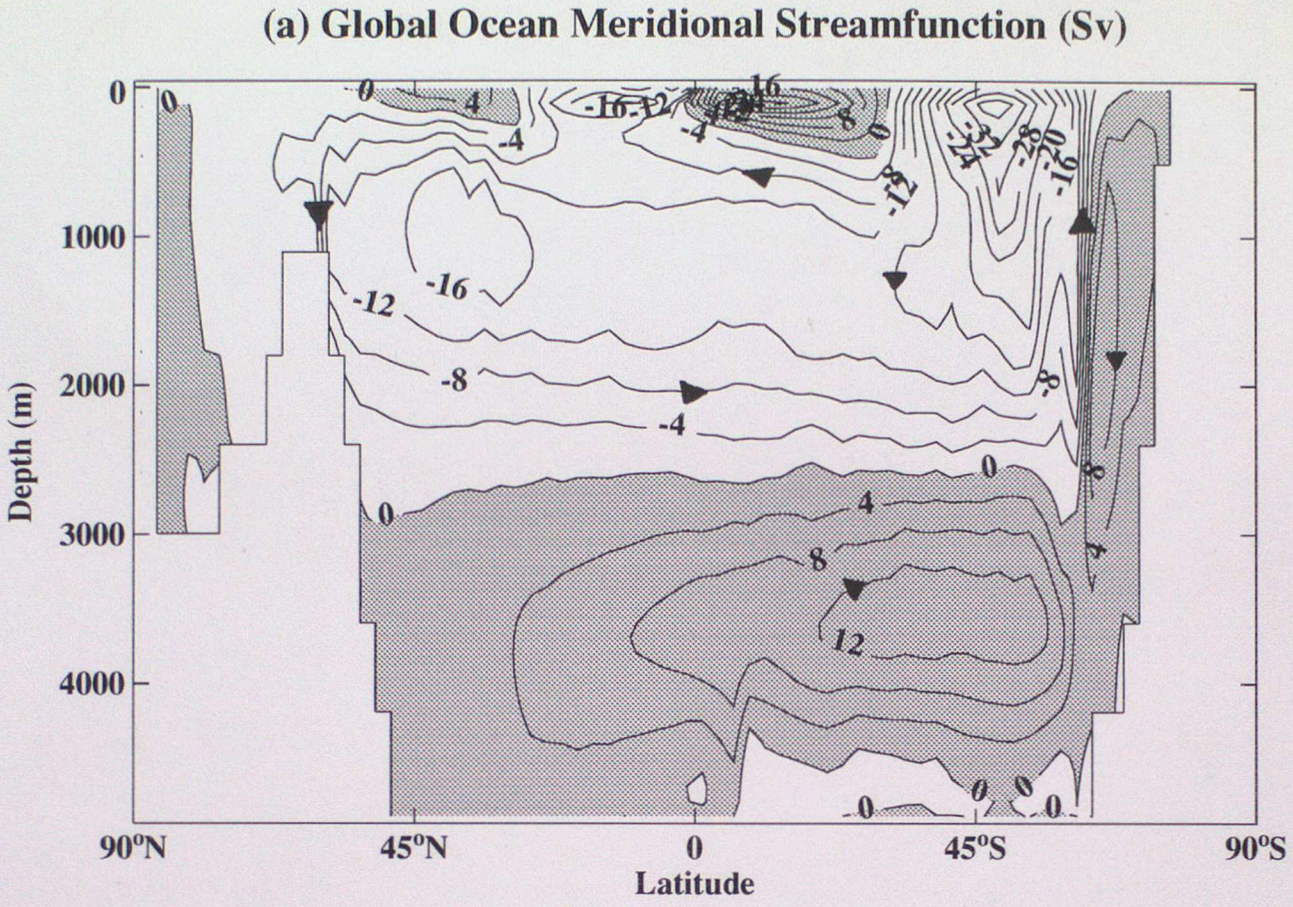
(a) Global Ocean Meridional Streamfunction (Sv)
Depth (m)
0
1000
2000
3000
4000
90°N
45°N
0
45°S
90°S
Latitude

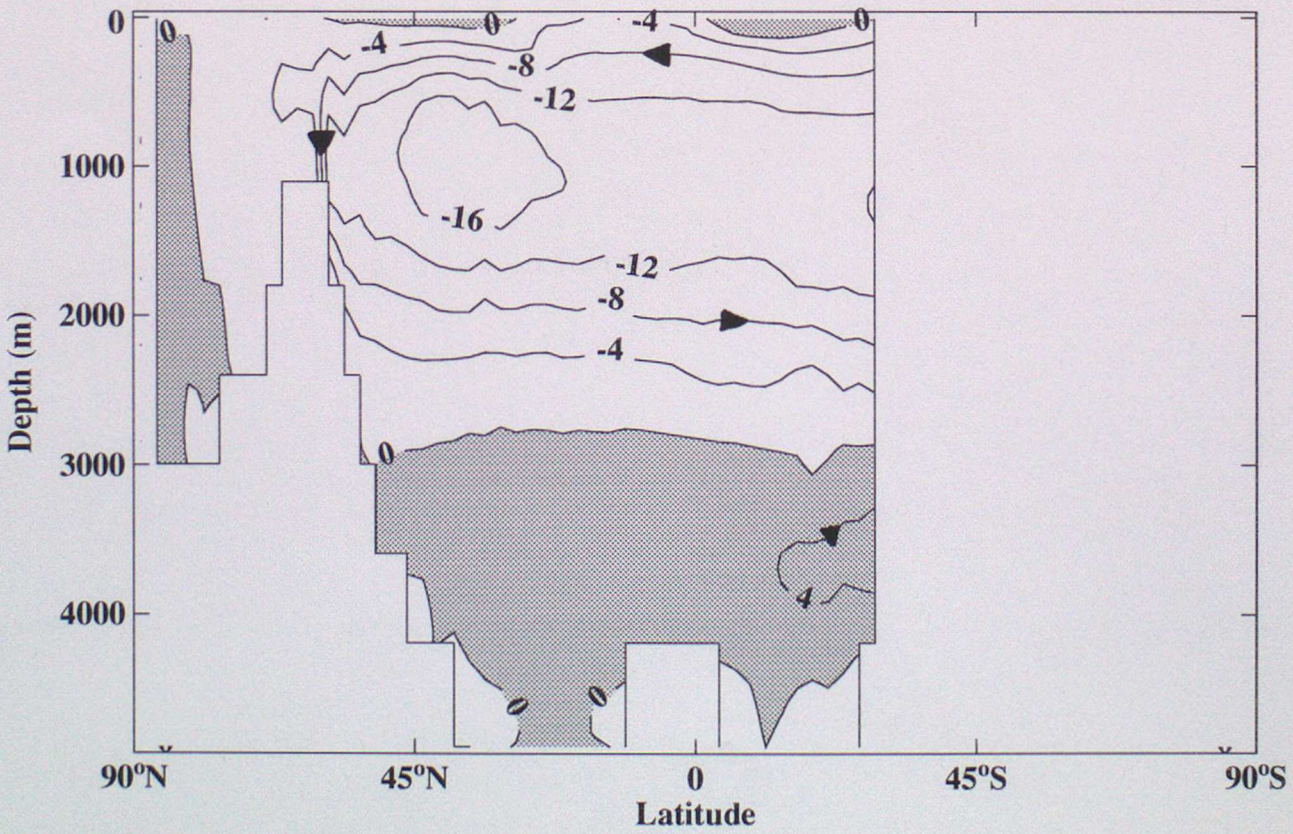
(b) Atlantic Ocean Meridional Streamfunction (Sv)
Depth (m)
0
1000
2000
3000
4000
90°N
45°N
0
45°S
90°S
Latitude

Figure 27

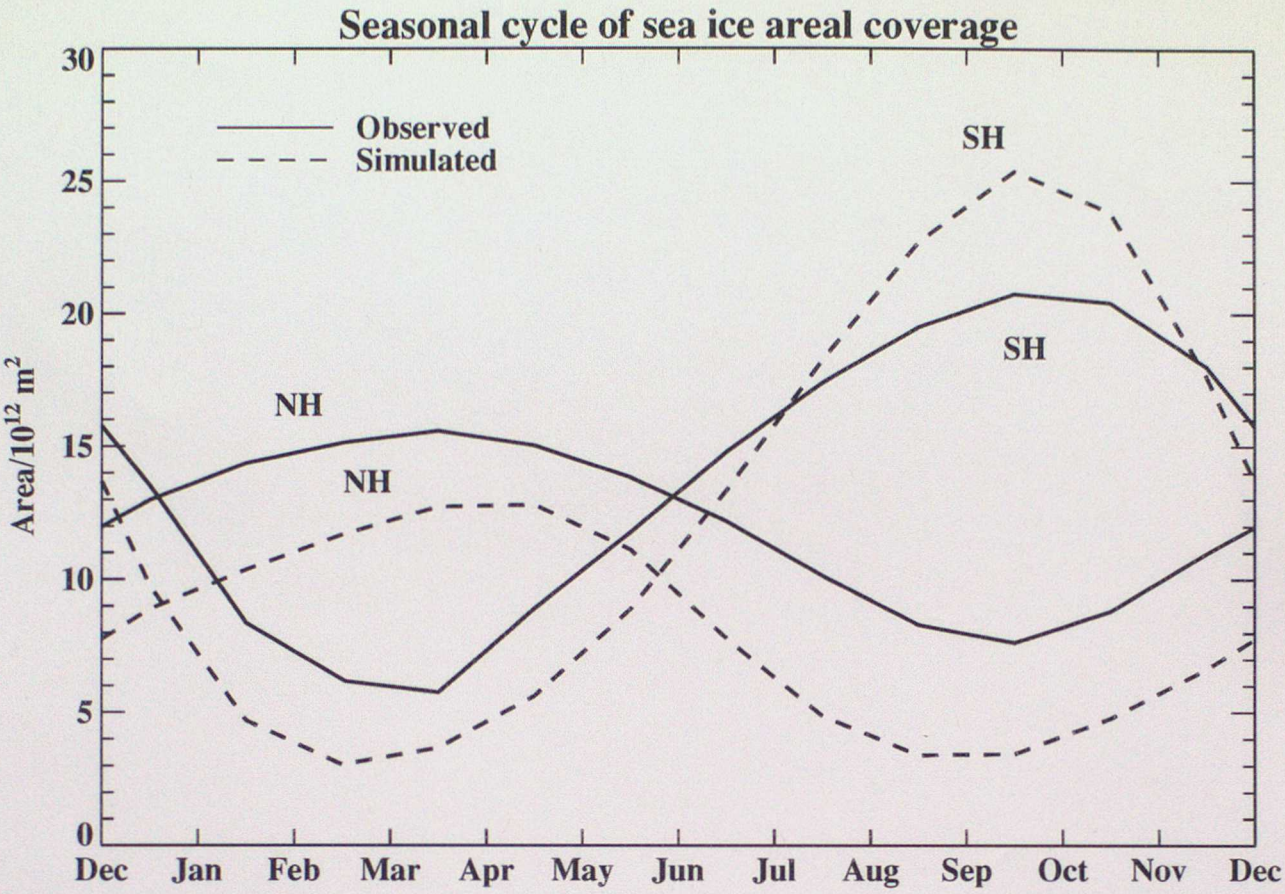
Seasonal cycle of sea ice areal coverage
Observed
Simulated
SH
SH
NH
NH
Area/10^12 m^2
30
25
20
15
10
5
0
Dec
Jan
Feb
Mar
Apr
May
Jun
Jul
Aug
Sep
Oct
Nov
Dec

Figure 28

Figure 29

HADCM2: September NH Ice Concentration

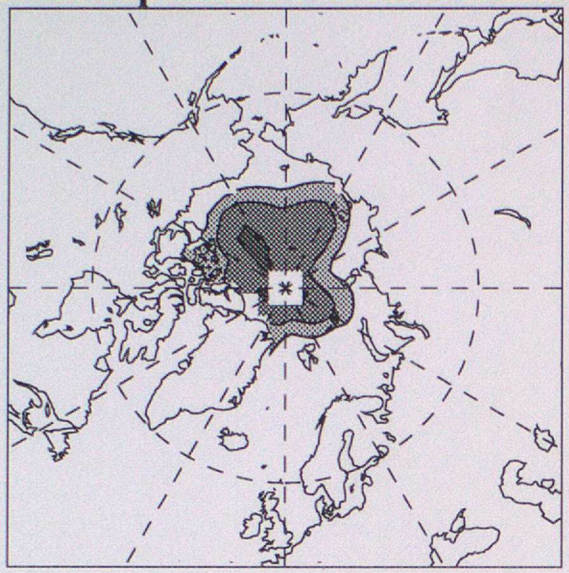

GISST: September NH Ice Concentration

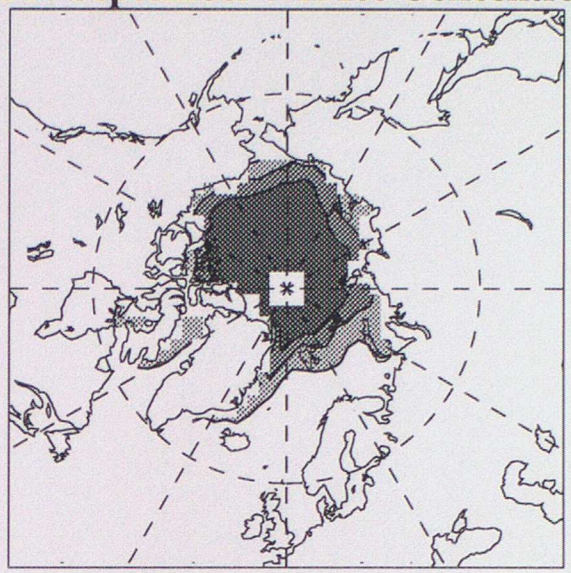

HADCM2: September SH Ice Concentration

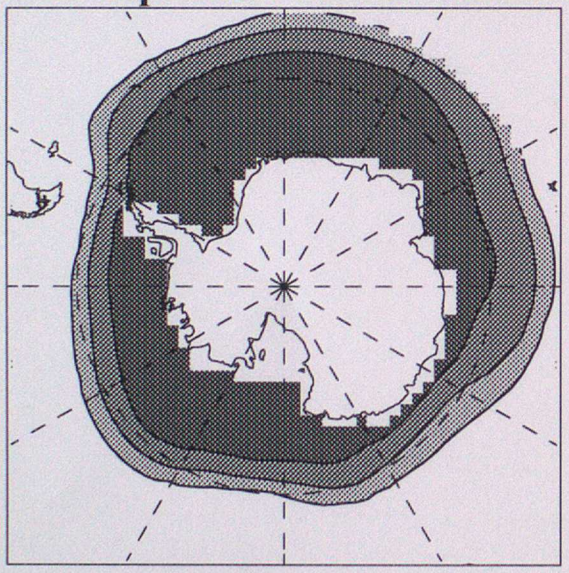

GISST: September SH Ice Concentration

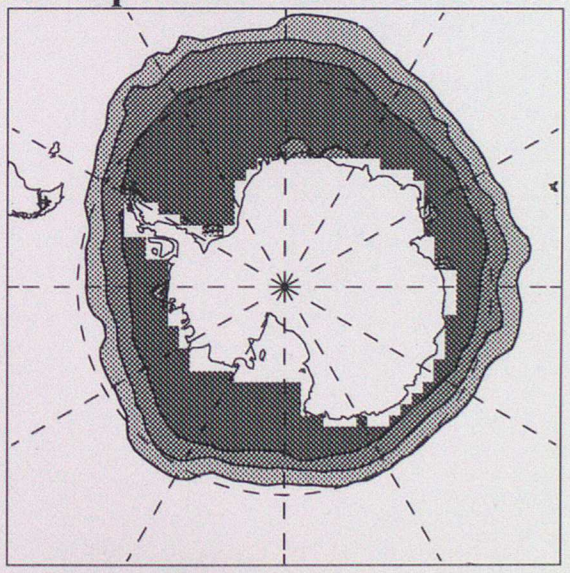

Figure 30

HADCM2: March NH Ice Concentration

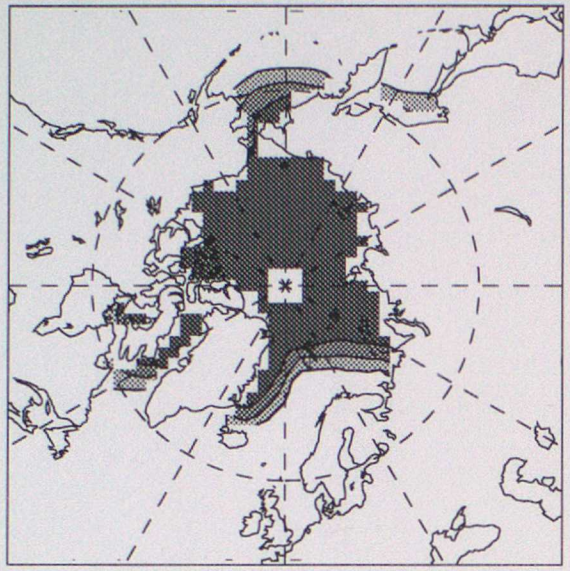

GISST: March NH Ice Concentration

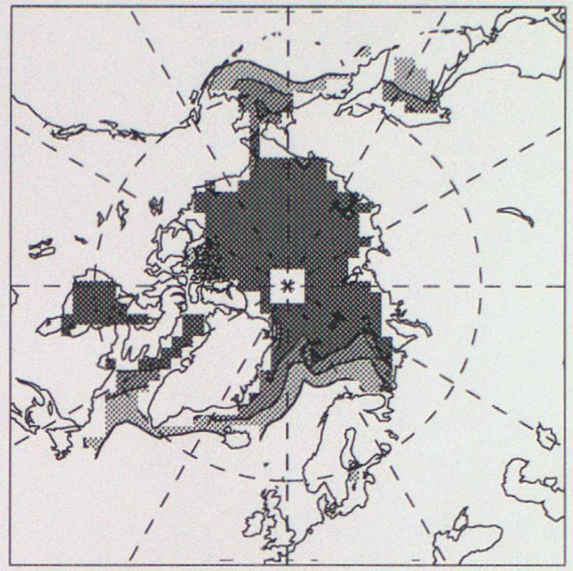

HADCM2: March SH Ice Concentration

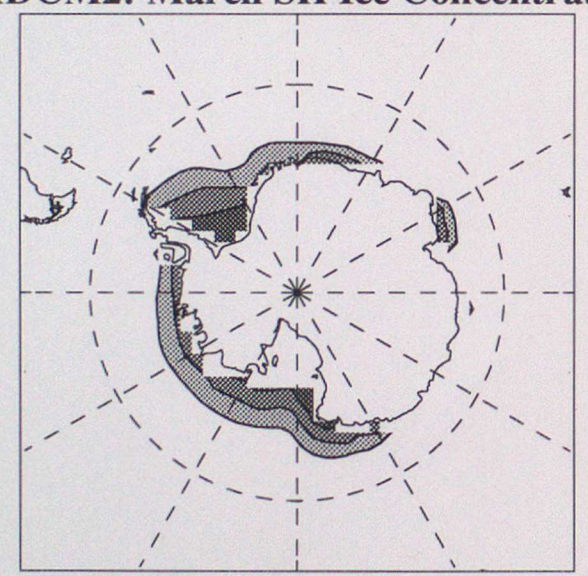

GISST: March SH Ice Concentration

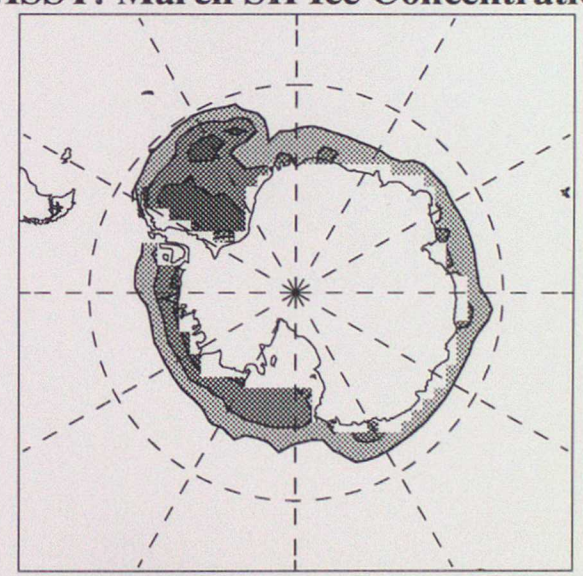

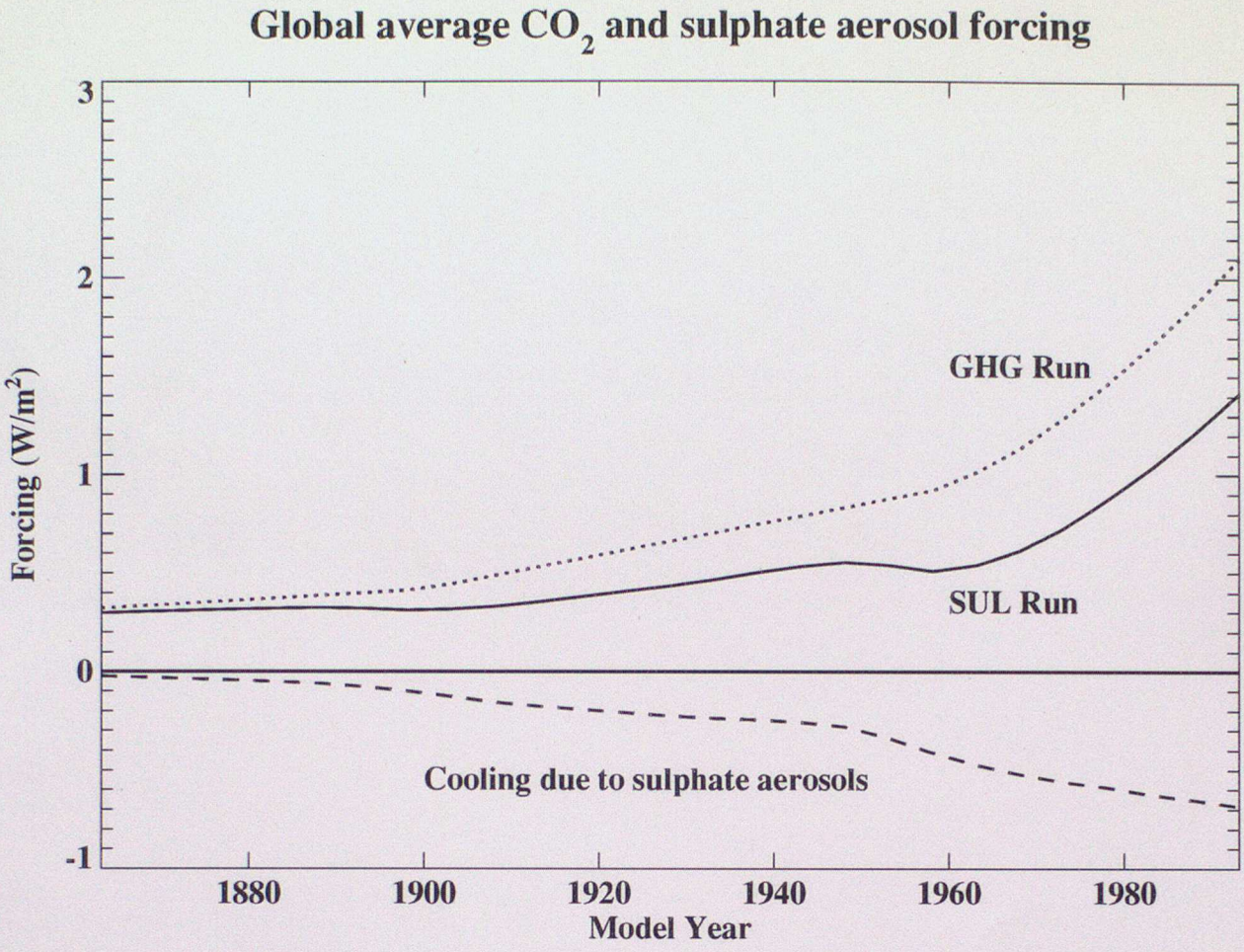
Global average CO_2 and sulphate aerosol forcing
Forcing (W/m^2)
3
2
1
0
-1
GHG Run
SUL Run
Cooling due to sulphate aerosols
1880
1900
1920
1940
1960
1980
Model Year

Figure 31

(a) GHG: Surface Air Temperature Change

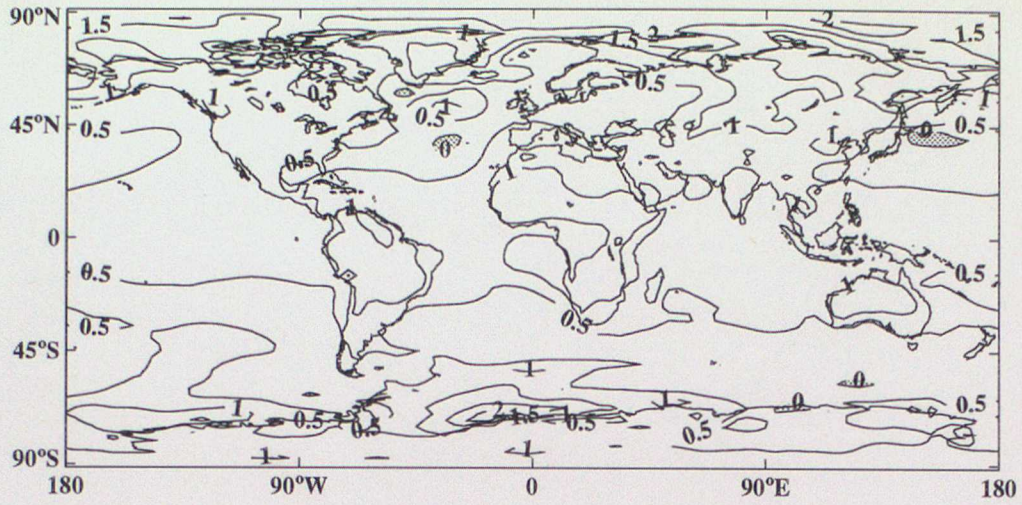

(b) SUL: Surface Air Temperature Change

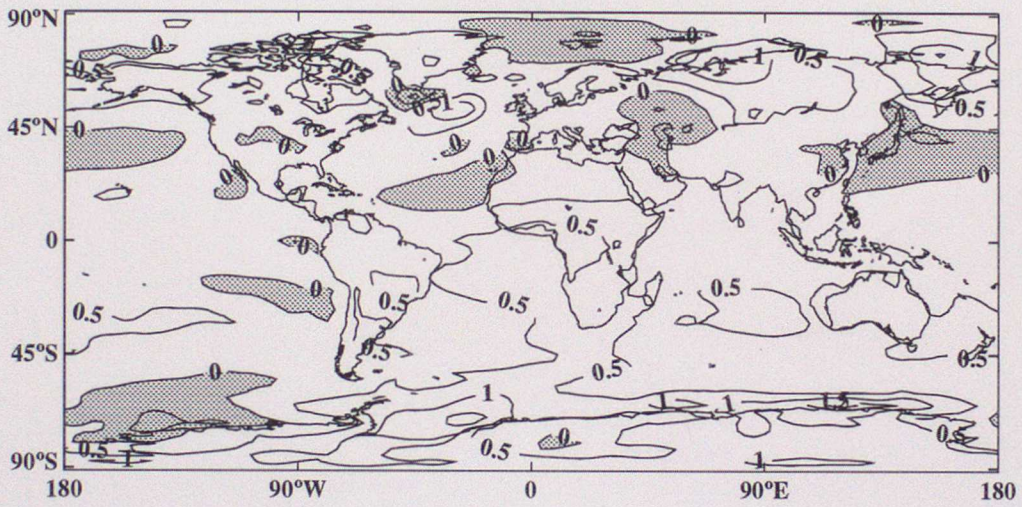

(c) OBSERVED: Surface Air Temperature Change

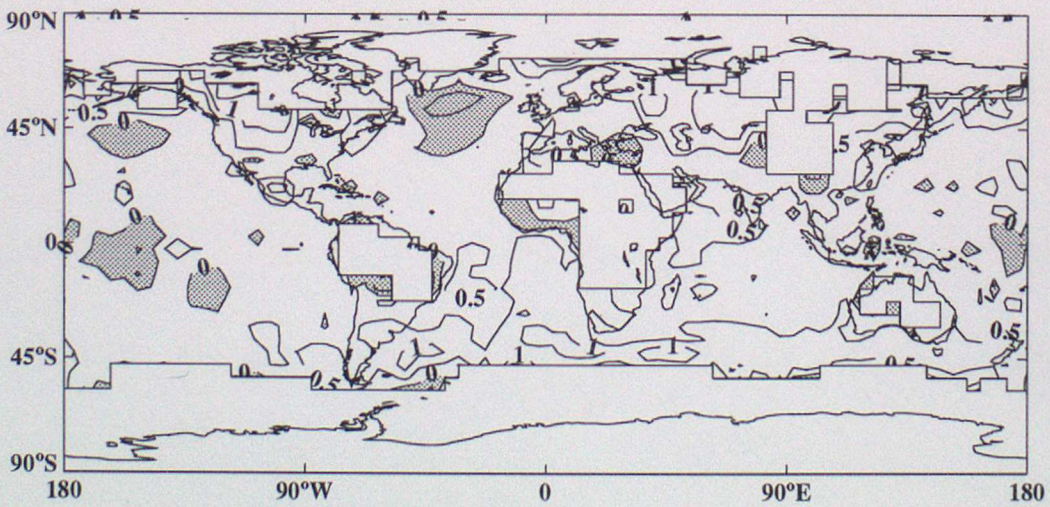

Figure 32

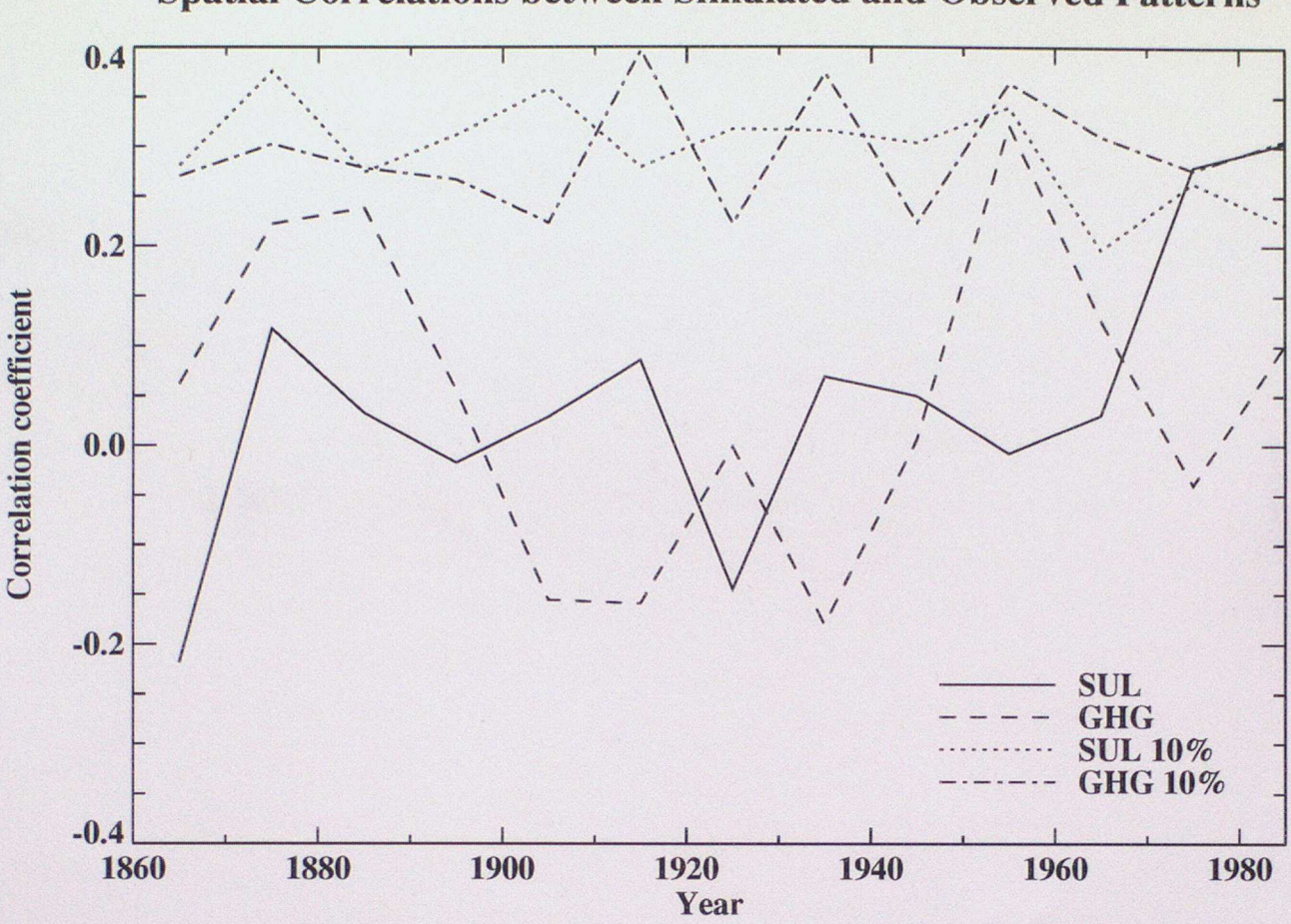
Spatial Correlations between Simulated and Observed Patterns
Correlation coefficient
0.4
0.2
0.0
-0.2
-0.4
1860
1880
1900
1920
1940
1960
1980
Year
SUL
GHG
SUL 10%
GHG 10%

Figure 33

(a) GHG: Decadal Zonal Anomalies of Average Surface Air Temperature

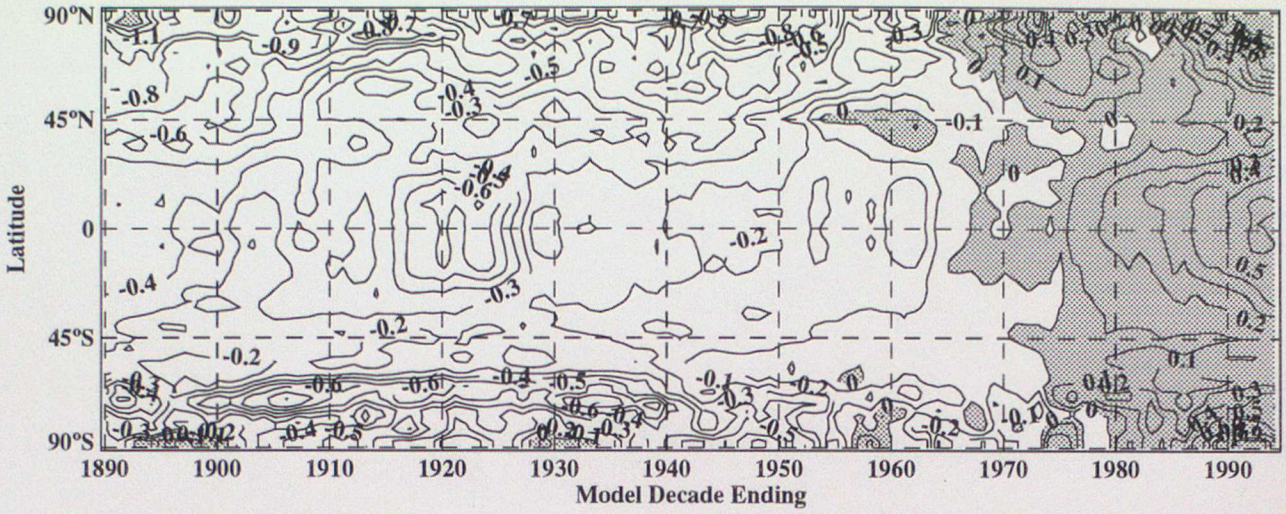

(b) SUL: Decadal Zonal Anomalies of Average Surface Air Temperature

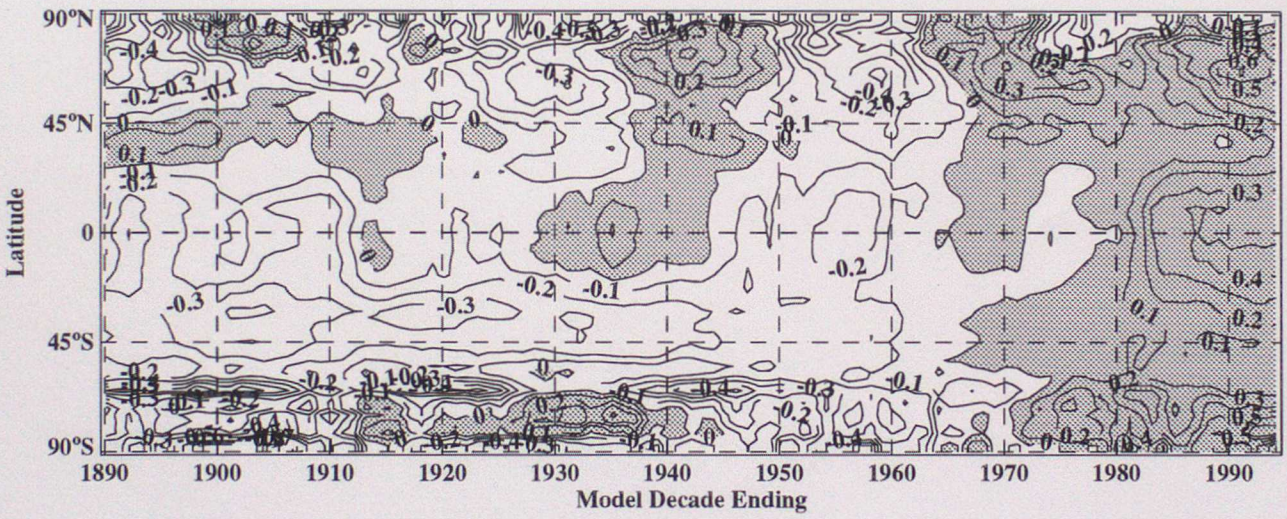

(c) OBSERVED: Decadal Zonal Anomalies of Average Surface Temperature

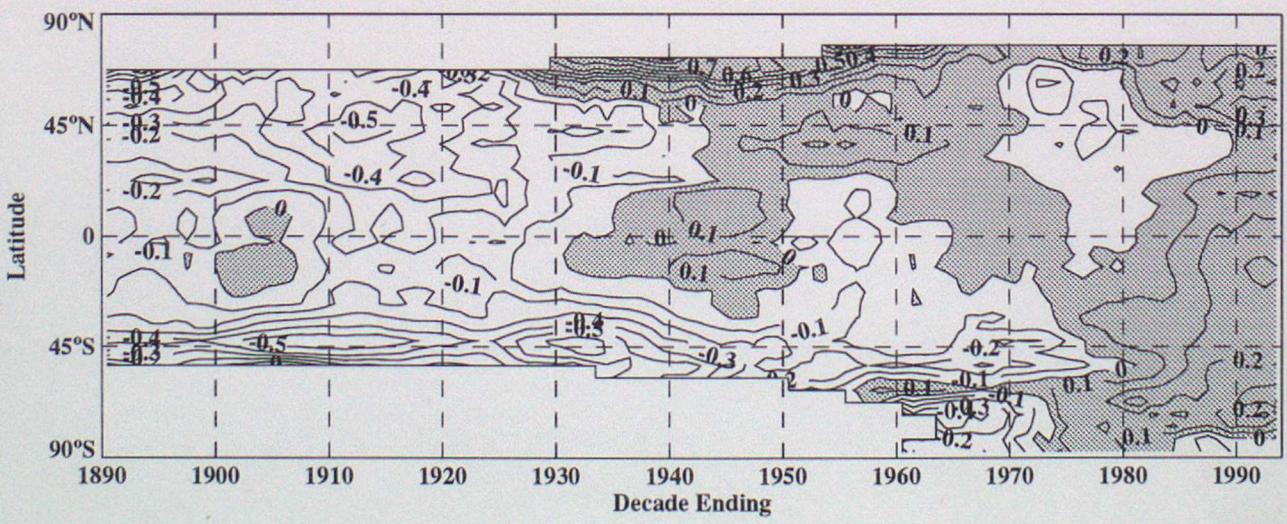

Figure 34

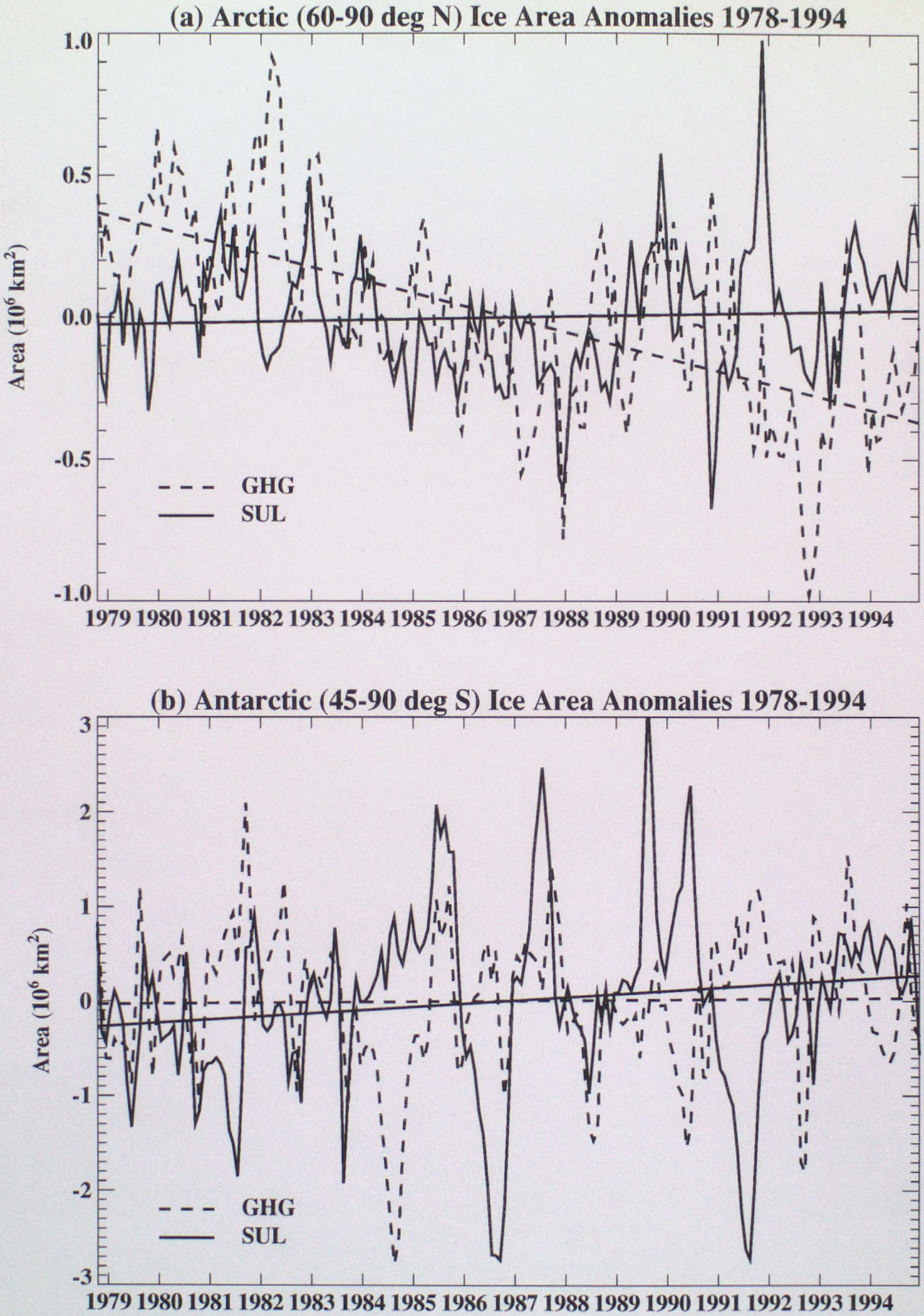
(a) Arctic (60-90 deg N) Ice Area Anomalies 1978-1994
Area (10^6 km^2)
1.0
0.5
0.0
-0.5
-1.0
GHG
SUL
1979 1980 1981 1982 1983 1984 1985 1986 1987 1988 1989 1990 1991 1992 1993 1994
(b) Antarctic (45-90 deg S) Ice Area Anomalies 1978-1994
Area (10^6 km^2)
3
2
1
0
-1
-2
-3
GHG
SUL
1979 1980 1981 1982 1983 1984 1985 1986 1987 1988 1989 1990 1991 1992 1993 1994

Figure 35

(a) GHG: 1963-1988 Atmospheric Temperature Trends (K/yr)

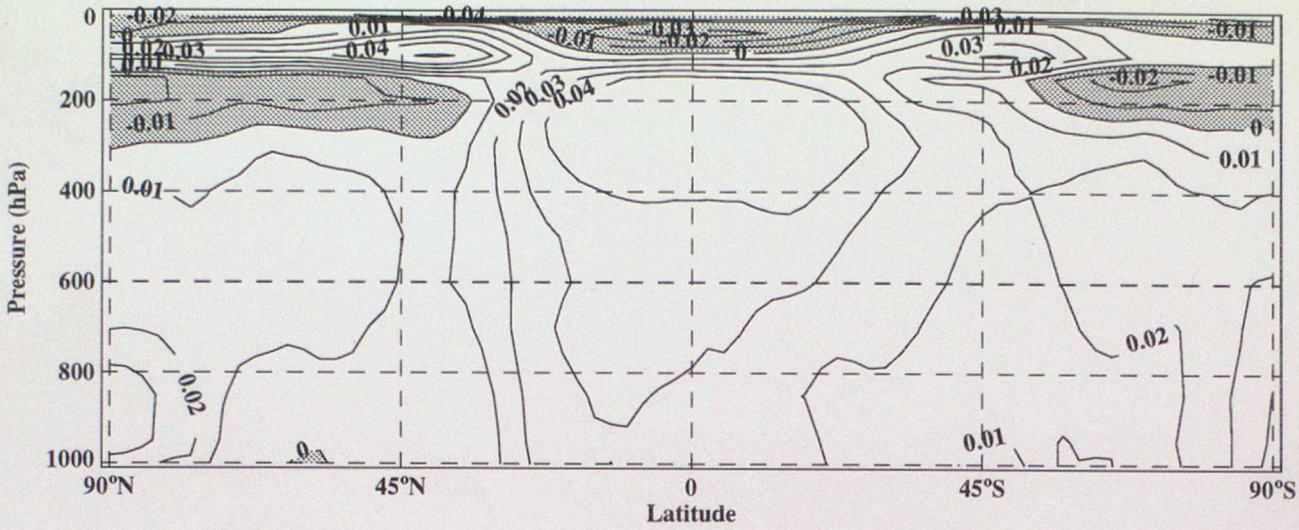

(b) SUL: 1963-1988 Atmospheric Temperature Trends (K/yr)

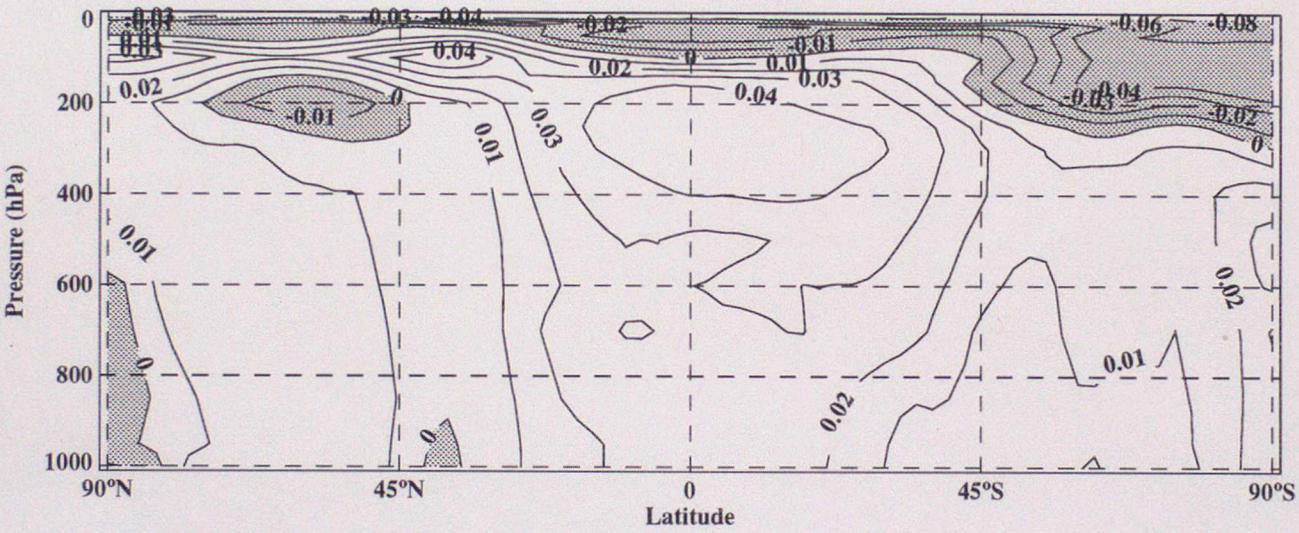

(c) OBSERVED: 1963-1988 Atmospheric Temperature Trends (K/yr)

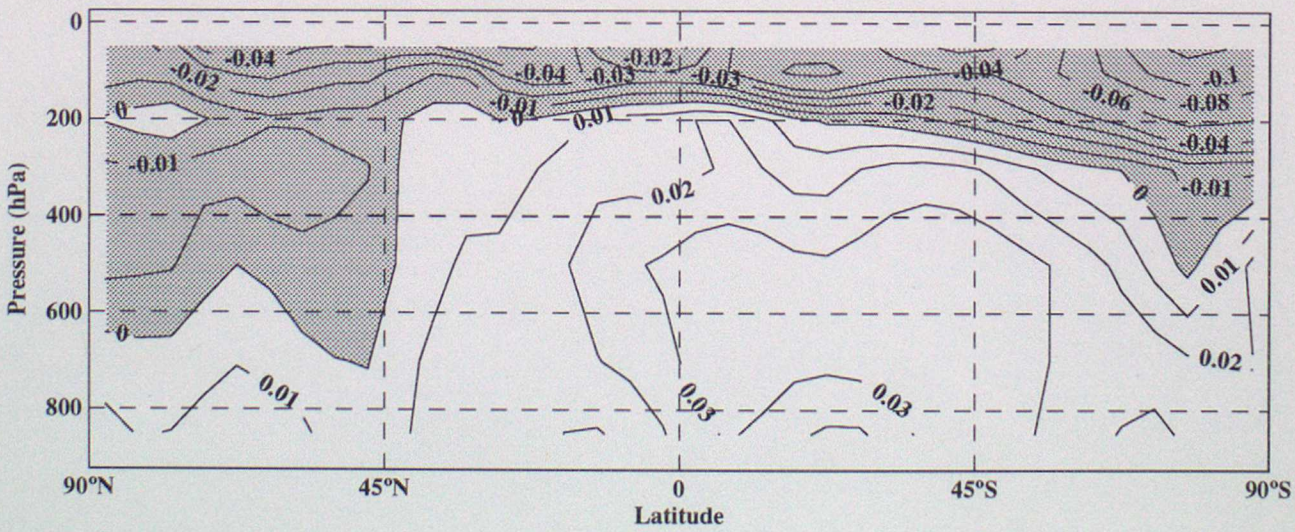

Figure 36

CLIMATE RESEARCH TECHNICAL NOTES

CRTN 1	Oct 1990	Estimates of the sensitivity of climate to vegetation changes using the Penman-Monteith equation. P R Rowntree
CRTN 2	Oct 1990	An ocean general circulation model of the Indian Ocean for hindcasting studies. D J Carrington
CRTN 3	Oct 1990	Simulation of the tropical diurnal cycle in a climate model. D P Rowell
CRTN 4	Oct 1990	Low frequency variability of the oceans. C K Folland, A Colman, D E Parker and A Bevan
CRTN 5	Dec 1990	A comparison of 11-level General Circulation Model Simulations with observations in the East Sahel. K Maskell
CRTN 6	Dec 1990	Climate Change Prediction. J F B Mitchell and Qing-cun Zeng
CRTN 7	Jan 1991	Deforestation of Amazonia - modelling the effects of albedo change. M F Mylne and P R Rowntree
CRTN 8	Jan 1991	The role of observations in climate prediction and research. D J Carson
CRTN 9	Mar 1991	The greenhouse effect and its likely consequences for climate change. D J Carson
CRTN 10	Apr 1991	Use of wind stresses from operational N.W.P. models to force an O.G.C.M. of the Indian Ocean. D J Carrington
CRTN 11	Jun 1991	A new daily Central England Temperature series, 1772-1991. D E Parker, T P Legg and C K Folland
CRTN 12	Jul 1991	Causes and predictability of Sahel rainfall variability. D P Rowell, C K Folland, K Maskell, J A Owen, M N Ward

CLIMATE RESEARCH TECHNICAL NOTES

CRTN 13	Jul 1991	Modelling changes in climate due to enhanced CO2, the role of atmospheric dynamics, cloud and moisture. C A Senior, J F B Mitchell, H Le Treut and Z-X Li
CRTN 14	Sep 1991	Sea temperature bucket models used to correct historical SST data in the Meteorological Office. C K Folland
CRTN 15	Aug 1991	Modelling climate change, and some potential effects on agriculture in the U.K. P R Rowntree, B A Callander and J Cochrane
CRTN 16	Aug 1991	The Boreal Forests and Climate G Thomas and P R Rowntree
CRTN 17	Aug 1991	Development of a Stratosphere-Troposphere Data Assimilation System. R Swinbank.
CRTN 18	Sep 1991	A study of asynchronous coupling using a simple climate model. M K Davey.
CRTN 19	Sep 1991	The Oceanic Carbon Cycle. N K Taylor
CRTN 20	Nov 1991	Worldwide ocean-atmosphere surface fields in Sahel wet and dry years using provisionally corrected surface wind data. M N Ward
CRTN 21	Dec 1991	Coupled tropical ocean global atmosphere models at the UKMO. M K Davey, C Gordon, S Ineson and S Lawrence
CRTN 22	Dec 1991	Empirical parameterisation of tropical ocean-atmosphere coupling. M Allen, M K Davey, D L T Anderson and P D Killworth
CRTN 23	Feb 1992	The temporal evolution of Equatorial Currents in the Indian Ocean D L T Anderson, D J Carrington, R A Corry and C Gordon
CRTN 24	Feb 1992	Stratospheric analyses provided by the U.K. Meteorological Office M J Bailey, A O'Neill and V D Pope

CLIMATE RESEARCH TECHNICAL NOTES

CRTN 25	Feb 1992	Modelling interannual variability in the Indian Ocean using momentum fluxes from the UKMO and ECMWF operational weather analyses. D L T Anderson and D J Carrington
CRTN 26	Mar 1992	A GCM simulation of the impact of Amazonian deforestation on climate using an improved canopy representation J Lean and P R Rowntree
CRTN 27	Mar 1992	The parameterization of rainfall interception in GCMs A J Dolman and D Gregory
CRTN 28	Jun 1992	Development of worldwide marine data eigenvectors since 1985 A W Colman
CRTN 29	Jun 1992	A tropical ocean model with reduced physics M K Davey
CRTN 30	Jun 1992	International Temperature Workshop, Boulder, Colorado, USA, 16 January 1992 Edited by D E Parker
CRTN 31	Jul 1992	Simulation of clear-sky outgoing longwave radiation over the oceans using operational analyses A Slingo and M J Webb
CRTN 32	Sep 1992	A prediction of the transient response of climate J M Murphy
CRTN 33	Nov 1992	LEPS scores for assessing climate model simulations and long-range forecasts. C K Folland
CRTN 34	Jan 1993	Stratospheric Data Assimilation System Guide Editer: R Swinbank
CRTN 35	Mar 1993	A Stratosphere-Troposphere Data Assimilation System R Swinbank and A O'Neill
CRTN 36	Mar 1993	Validation of hydrological schemes for climate models against catchment data. P R Rowntree and J Lean

CLIMATE RESEARCH TECHNICAL NOTES

CRTN 37	Apr 1993	Modelling of palaeoclimates: Examples from the recent past J F B Mitchell
CRTN 38	May 1993	A simulation of seasonality in ENSO forecast skill M K Davey, D L T Anderson and S Lawrence
CRTN 39	Jul 1993	ENSO Prediction experiments using a simple ocean-atmosphere model D-H Wu, D L T Anderson and M K Davey
CRTN 40	Sep 1993	Diagnosis of dynamic sea-surface and sea-level changes from the Cox ocean model J M Gregory
CRTN 41	Sep 1993	Seasonal variations of the clear-sky greenhouse effect: the role of changes in atmospheric temperatures and humidities M J Webb, A Slingo and G L Stephens
CRTN 42	Nov 1993	Sea-level changes under increasing atmospheric CO_2 in a transient coupled ocean-atmosphere GCM experiment. J M Gregory
CRTN 43	Dec 1993	Global and regional patterns of climate change: recent predictions for the Arctic P R Rowntree
CRTN 44	Feb 1994	The effect of changing horizontal diffusion in the atmospheric version of the unified climate model C D Hall and R A Stratton
CRTN 45	Mar 1994	Simulation of El-Niño/Southern Oscillation like variability in a global AOGCM and its response to CO_2 increase. S F B Tett
CRTN 46	Apr 1994	Global data required for monitoring climate change. D E Parker and C K Folland
CRTN 47	May 1994	Seasonal uptake of anthropogenic CO_2 in an ocean general circulation model. N K Taylor

CLIMATE RESEARCH TECHNICAL NOTES

CRTN 48	Jun 1994	A tropic-wide oscillation of boreal summer rainfall and patterns of sea-surface temperature. M N Ward, K Maskell, C K Folland, D P Rowell and R Washington
CRTN 49	Jun 1994	Simulation of the tropical Pacific using a simplified ocean model M A Balmaseda, D L T Anderson and M K Davey
CRTN 50	Sep 1994	Simulation of global mean temperature using a box-diffusion climate model P R Rowntree
CRTN 51	Sep 1994	Seasonal dependence of ENSO prediction skill M A Balmaseda, M K Davey and D L T Anderson
CRTN 52	Nov 1994	Simulation of the Indian Monsoon and Tropical Intraseasonal Variability by a General Circulation Model P M Inness and D Gregory
CRTN 53	Mar 1995	A comparison of modelled surface fluxes with climatological estimates. C Gordon and D K Wright
CRTN 54	Mar 1995	The representation of moist convection in atmospheric models. D Gregory
CRTN 55	Mar 1995	A consistent treatment of the evaporation of rain and snow for use in large-scale models D Gregory
CRTN 56	Apr 1995	Workshop on simulations of the Climate of the Twentieth Century using GISST, 28-30 November 1994, Hadley Centre, Bracknell, UK Edited by C K Folland and D P Rowell
CRTN 57	May 1995	Enhanced shortwave cloud radiative forcing due to anthropogenic aerosols. S E Swartz and A Slingo
CRTN 58	May 1995	The simulation of the tropical oceans in models of different horizontal resolution. C Gordon, D K Wright and C M Roberts
CRTN 59	Sep 1995	The water budget of middle latitude continental regions - a modelling and observational study P R Rowntree
CRTN 60	Sep 1995	Intraseasonal variability of the Indian summer monsoon simulated by the Hadley Centre climate model K Ashok, D Gregory and P M Inness

CLIMATE RESEARCH TECHNICAL NOTES

CRTN 61	Sep 1995	Climate simulations with the Unified Model: AMIP runs C D Hall, R A Stratton and M L Gallani
CRTN 62	Nov 1995	Validation of surface parameters over the oceans in climate simulations with the unified model. C D Hall
CRTN 63	Dec 1995	The GISST2.2 sea surface temperature and sea-ice climatology D E Parker, M Jackson and E B Horton
CRTN 64	Dec 1995	Parametrization of momentum transport by convection. II: Tests in single column and general circulation models. D Gregory, R Kershaw and P M Inness
CRTN 65	Jan 1996	Understanding the sensitivity of a GCM simulation of Amazonian deforestation to the specification of vegetation and soil characteristics. J Lean and P R Rowntree
CRTN 66	Jan 1996	On the efficient calculation of infra-red fluxes and cooling rates using the two-stream equations. J M Edwards
CRTN 67	Jan 1996	The second Hadley Centre coupled ocean-atmosphere GCM: Model description, spinup and validation. TC Johns,RE Carnell,JF Crossley,JM Gregory, JFB Mitchell,CA Senior,SFB Tett and RA Wood